12-2015

Electrospray deposition of chalcogenide glass films for gradient refractive index and quantum dot incorporation

Spencer Novak
Clemson University, spencen@g.clemson.edu

ELECTROSPRAY DEPOSITION OF CHALCOGENIDE GLASS FILMS FOR GRADIENT REFRACTIVE INDEX AND QUANTUM DOT INCORPORATION

A Dissertation
Presented to
the Graduate School of
Clemson University

In Partial Fulfillment
of the Requirements for the Degree
Doctor of Philosophy
Materials Science and Engineering

---

by
Spencer Novak
December 2015

Accepted by:
Dr. Igor Luzinov, Committee Chair
Dr. Kathleen Richardson
Dr. Konstantin Kornev
Dr. John Ballato
Dr. Luiz G. Jacobsohn

ABSTRACT

Chalcogenide glasses (ChGs) are well-known for their optical properties, making them ideal candidates for emerging applications of mid-infrared microphotonic devices, such as lab-on-a-chip chemical sensing devices, which currently demand additional flexibility in processing and materials available to realize new device designs.

Solution-derived processing of ChG films, initially developed in the 1980s by Chern and Lauks, has consisted mainly of spin-coating and offers unique advantages over the more traditional physical vapor deposition techniques. In the present effort, the nanoparticles of interest are luminescent quantum dots (QDs), which can be used as an on-chip source of light for a planar chemical sensing device. Prior efforts of QD incorporation have exposed limitations of spin-coating of ChG solutions, namely QD aggregation and material waste, along with incompatibility with larger scale manufacturing methods such roll-to-roll processing.

This dissertation has evaluated electrospray (ES) as an alternative method of solution-derived chalcogenide glass film deposition. While employed in other materials systems, deposition of optical quality ChG films via electrospray has not been previously attempted, nor have parameters until now, been defined. This study has defined pre-cursor solution chemistry, electrospray jet process parameters required for formation of stable films, annealing protocols and resulting film attributes, yielding important correlations needed to realize high optical quality films. Electrosprayed films attributes were compared to those seen for spin coating and trade-offs in processing route and resulting quality, were identified. Optical properties of importance to device applications were defined, including

surface roughness, refractive index, and infrared transmission. The use of a serpentine path of the spray over the substrate was demonstrated to obtain uniform thickness, blanket films, and demonstrates process compatibility with roll-to-roll processing whereby (theoretically) 100% of starting solution can be utilized in a continuous process.

The present effort has shown that electrospray offers the advantage of spatially defined, localized deposition, which enables direct 2-D and 3-D printing, though with limited (unoptimized) spatial resolution on the order of millimeters. Knowledge of processing protocols were exploited to fabricate multi-layer films from two different glass compositions to yield an effective refractive index gradient (GRIN). GRIN coatings were fabricated and refractive index variations were predicted.

The advantages of electrospray deposition were also explored for the enhancement of quantum dot doping in ChG films. A hypothesis whereby electrospray would enable deposition of films based on consolidation of many, single QD doped aerosol droplets was developed and evaluated. Experimental validation of this premise in CdSe and PbS doped ChG films was shown, indicating that electrospray offers a kinetic barrier to QD movement preventing aggregation from occurring, not seen in spin-coating. Two types of organic ligands were found to enhance dispersion of QDs in amine solvents, octadecylamine and mercaptopropionic acid. Utilizing TEM characterization, evidence that electrospray may be more suitable than spin-coating for the dispersion of QDs in solution-derived ChG films was confirmed. However, the ultimate effectiveness of this approach was limited due to the ability to quantify direct loading levels of the QD and surrounding glass matrix.

This work demonstrates that electrospray offers additional flexibility over spin-coating and other evaporation methods for the deposition of ChG coatings. Electrospray processing of doped and undoped ChG solutions for microphotonic applications has been shown as a viable alternative in the processing and material toolbox where spatially defined index and dopant control is required.

DEDICATION

First and foremost, to my wife, Jackie, for her love and support as I pursued my dream of earning a PhD.

To my parents and siblings for giving me the mindset that full potentials are often larger than you originally thought them to be, and for pushing me to pursue them.

To my grandparents and extended family, for sharing their wisdom and always caring about my path through life.

ACKNOWLEDGMENTS

I owe a huge thank you to my advisor, Dr. Kathleen Richardson. She has truly gone above and beyond the required duties. Thanks to her, I have had to opportunity to study at Université Bordeaux and work with many great collaborators. This PhD has also been shaped and furthered by my outstanding committee of Dr. Igor Luzinov, Dr. Luiz Jacobsohn, Dr. Konstantin Kornev, and Dr. John Ballato.

There are many others to thank for their major contributions to this dissertation. To Dr. Weiwei Deng, Dr. Danvers Johnston, and Dr. Cheng Li, I am deeply grateful for the use of their electrospray system and for lending their expertise to my experiments.

Dr. Manashi Nath and Wipula Liyanage from the Missouri University of Science and Technology have helped greatly by optimizing quantum dot surface chemistry for our chalcogenide glass solutions and providing samples.

For their aid in measuring photoluminescence and use of their instruments, I am very appreciative to Dr. Nathan McClenaghan, Dr. Sergey Denisov and Dr. Luca Scarpantonio from Université Bordeaux, as well as Dr. Mercedeh Khajavikhan and Hossein Hodaei from the University of Central Florida.

Matt Schneider from the Materials Characterization Facility at the University of Central Florida has done a tremendous job with transmission electron microscopy analysis and training.

Finally, I thank Dr. Pao-Tai Lin and Dr. Anuradha Agarwal from the Massachusetts Institute of Technology for excellent ideas on advancing and refining this research.

Funding for this research was provided by Defense Threat Reduction Agency contracts:

HDTRA1-10-1-0073: *Gradient Films from Shape Memory Nanofoams for Waveguide Coating*

HDTRA1-13-1-0001: *Evaluation of Radiation-induced Photonic Defects in Silicon, Germanium, Chalcogenides, and Polymers*

TABLE OF CONTENTS

LIST OF TABLES

LIST OF FIGURES

List of Figures (Continued)

List of Figures (Continued)

List of Figures (Continued)

List of Figures (Continued)

List of Figures (Continued)

I. INTRODUCTION

This chapter will discuss the motivation and goals of this dissertation, as well as background information of the subjects studied, including optics, photonics, chemical sensing devices, chalcogenide glasses, quantum dots, and film deposition techniques. This chapter will describe the state-of-the-art in each area, and how this dissertation builds on those previous studies in order to make contributions to the field of ChG planar optics and photonics, with the primary goal being the development mid-IR microphotonic chemical sensing devices.

1.1. Motivation and research objectives

Chip-based, integrated photonics is a promising technology with potential high-impact applications such as chemical and biological sensing [1]. For these applications, the mid-infrared (mid-IR) regime from 2.5 to 10 μm is especially important because this is the location of the optical fingerprint of most chemical species of interest. Therefore, materials which are transmissive to mid-IR light and amenable to fabrication in film form and subsequent lithography are required for the creation of the optical components in such a device.

Chalcogenide glasses (ChGs), which can be formed into films using solution-based and evaporation-based methods, are particularly interesting because of their large transmission window in the infrared, and widely tunable properties, which can be tailored by choosing compositions from the various families of ChGs. Each type of deposition

technique has advantages and disadvantages, but a key advantage of film formation from solution is that nanoparticles can be incorporated by simple mixing of solutions prior to deposition. Thus, a hybrid material can be formed with properties unattainable by any single material by utilizing the extraordinary optical properties of nanoparticles. Specifically, the motivation of this dissertation is to effect luminescent properties in ChG films through the incorporation of infrared-emitting semiconductor quantum dots (QDs). Such a material could serve as a light source in an integrated, microphotonic device.

The main subject of this author's Master's thesis was a study on the incorporation of PbS and CdSe QDs into spin-coated $Ge_{23}Sb_7S_{70}$ films. While photoluminescence from the films was observed, it was found that the QDs did not disperse homogeneously in the deposited film, but instead were grouped in large aggregates. In order to maximize the efficiency of the emission, and to minimize scattering losses in the material, it is necessary to disperse the QDs homogeneously. Based on the need for better dispersion of QDs in ChG films, and the potential applications in microphotonic devices, the goal of this dissertation has been to improve the dispersion of QDs in solution-derived ChG films. Previously, a common QD synthesis recipe was used, with QD surface chemistry that was not optimized for the ChG solution. The QDs were dispersed in a typical organic carrier solvent (chloroform), and mixed with the ChG/amine solution prior to deposition by spin-coating. This was done because the QDs did not disperse in amines, and the film was deposited as quickly as possible in order to minimize the amount of time during which the QDs could aggregate. For the work done in this dissertation, we have collaborated with Dr. Manashi Nath at Missouri S&T in order to design a QD that disperses well in amine

solvents, eliminating the need for a QD carrier solvent. More importantly, reducing the thermodynamic driving force for aggregation through an optimization of the surface chemistry is the much needed, first step toward homogeneous dispersion of QDs in a solution-derived film.

In addition to studying the effect of surface chemistry on QD dispersion in ChG solutions, electrospray, a new method of solution-based ChG film deposition, was explored. To our knowledge, electrospray has never been used with ChG solutions, though it has been studied for the deposition of other types of films. One of the main objectives of this dissertation was to develop ChG film deposition by electrospray, and investigate its potential for better dispersion of QDs.

This dissertation aims to:

- Explore the fabrication of gradient refractive index (GRIN) coatings through the flexibility of the electrospray process
- Understand how the degree of dispersion varies with film deposition method (spin-coating vs. electrospray) and with the processing parameters used in each method
- Characterize the resulting luminescent properties of QD-doped ChG solutions and films

1.2. Background

1.2.1. Optics and photonics

The idea of manipulating light to perform some function originated at least as long ago as ~3200 B.C., which is evidenced by an Egyptian knife handle containing microscopic carvings that could have only been done under significant magnification [2]. In 300 B.C., optics was born as a science when Euclid, a Greek mathematician, wrote a work containing postulates that explained the fundamentals of vision [3]. Meanwhile, the use of light as a means of communication, such as a signal fire, is also an idea that probably dates back several thousand years. The photophone, invented in 1880 by Alexander Graham Bell, is particularly noteworthy because it is the first electrical device to transmit information using light.

Today, light is used for many purposes, including imaging, information displays, information storage, minimally invasive medical procedures, laser cutting and welding in manufacturing processes, telecommunications, generation of energy with solar cells, chemical sensing, and many different laboratory instruments such as spectrometers [4]. Many of these applications would not be possible without the laser, invented in the 1950s, which has the primary advantages of good spatial coherence (light is minimally divergent) and temporal coherence (narrow range of emission wavelengths).

These applications are also enabled by electronics, which began in the early 1800s with Alessandro Volta's battery and then furthered by the invention of the vacuum tube in 1910. Modern electronics originated in 1948 with the creation of the semiconductor

transistor by John Bardeen and Walter Brattain at Bell Labs, and took another leap forward with the development of the electronic integrated circuit (EIC) by Jack Kilby in the late 1950s, allowing smaller, cheaper, and more complex electronic circuits. Today, EICs with components on the micron size scale (microelectronics) can be found nearly anywhere as essential components of computers, cellular phones, and vehicles, to name just a few.

Photonic integrated circuits (PICs) are analogous to EICs, with the primary difference being that PICs operate at visible, near-infrared, and mid-infrared wavelengths of light, as opposed to the conduction of electrons. Since optical signals travel much faster than electronic signals, PICs offer potentially quicker operation and higher bandwidth. This is evidenced by the replacement of copper telecommunication wires with optical fiber beginning the late 1970s, enabling a three order of magnitude jump in bandwidth from 10^5 bit/s to 10^8 bit/s [4]. However, there are challenges that impede the replacement of microelectronic systems with microphotonics. It is unknown whether or not PICs can be made with similar density of components as a microelectronic circuit. Additionally, while an EIC is made of silicon and silica, a PIC consists of crystalline semiconductors, polymers, oxides, plastics, and glasses, making integration in a PIC difficult due to the wide range of physics and technology involved [4]. Recently, a new initiative by the US government has been awarded to expand the manufacturability of photonic chip-based systems to realize high performance, low cost components and devices. The five year, $660+ million consortium will be housed at the State University of New York (SUNY), and called the Integrated Photonics Institute for Manufacturing Innovation (IP-IMI) [5].

As part of a longstanding collaboration of team members [1,6-10] supported by diverse funding organizations interested in deploying small footprint, low cost on-chip sensor components and devices which leverage know-how from semiconductor fabrication via lithographic techniques, our team has been focusing on developing small, integrated, "lab-on-a-chip" chemical sensing technology. The goal of the effort, for example, would result in devices which could be left unattended for treaty verification to ensure that there is no production of nuclear weapons. This can be done with sensors operating in the mid-IR (3-5 μm), as this is where most chemicals of interest have their optical signature. An overview of sensing devices is presented in the following section.

1.2.2. Sensing devices

Identifying and quantifying the presence of chemical species provides invaluable information for investigative or decision-making processes. Just a few examples include medical diagnosis and treatment, analysis of the environment for water quality, presence of chemical weapons, and monitoring the manufacturing of some product, such as food, or chemicals. Given the wide variety of analytes, there exists many chemical sensing devices based on different physical principles. There are four main categories of sensing principles, including thermal, mass, electrochemical, and optical [11].

- Thermal chemical sensors utilize the amount of heat generated by a steady-state chemical reaction
- Mass chemical sensors typically absorb the chemical of interest onto a surface and detect the change in mass
- Electro-chemical sensors are (broadly) based on the interaction of chemicals with electricity
- Optical chemical sensors are based on the interaction of chemicals with electromagnetic waves

In an optical sensor, the light, which can contain many wavelengths or selected wavelengths, must interact with the analyte before being detected in its new form and subjected to further processing. The following table shows the type of interaction and information that can be obtained by different wavelength ranges of light [11].

Table 1.1: Types of interactions between an analyte and different regions of the optical spectrum, taken from reference [11]

Table 9.1 Molecular spectroscopy by optical sensors

Region	Wavenumber (μm^{-1})	Wavelength (μm)	Transition	Information	Energy (kJ/mol)
Far IR	10^{11}–10^{12}	10–1,000	rotational	Interactions	0.5
IR–Raman	10^{12}–10^{14}	1–10	vibrational	functional groups	4
UV–Vis	10^{14}–10^{16}	0.1–1	electronic	ionization energy	40–400

Many different sensor designs are utilized to probe these various types of material information, and are classified in the following chart, taken from reference [12].

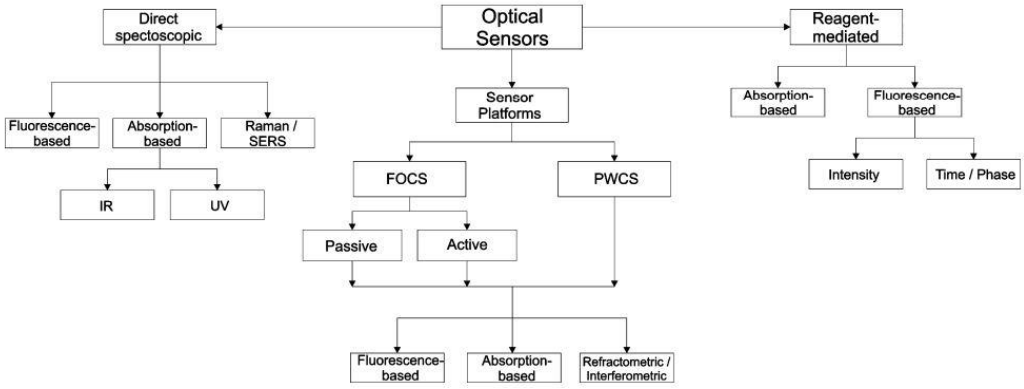

Figure 1.1: Classification of optical sensors, taken from reference [12].

Direct spectroscopic sensors measure an intrinsic optical property of the analyte, such as absorption, fluorescence or Raman scattering. Such a measurement, like an absorption spectra from an FTIR spectrometer, for example, can give very detailed information about the analyte. However, the large size and complex, sensitive optics required usually make such a device impractical and cost-prohibitive for transportation between locations or unattended sensing. Therefore, it is the aim of many researchers to develop small, inexpensive, highly-sensitive chemical sensors. There are two main sensor platforms utilized to achieve these goals, fiber optic chemical sensors (FOCS) and planar waveguide-based chemical sensors (PWCS). Planar sensors are compatible with existing

microfabrication technology and have a robust nature, allowing deployment in a wider variety of environments [12].

Fiber sensors and planar sensors both utilize three principle transduction mechanisms: fluorescence, absorption, and refractometry. As shown in Figure 1.1, fiber sensors can be passive, where the role of the fiber is simply to transport light to the analyte and then to the detector, or active, where the sensing is linked to an intrinsic change in the optical properties of the fiber. A reflection geometry is commonly used, in which one fiber (or bundle of fibers) guides light to the analyte, and another collects the reflected light to the detector.

Usually, the creation of an active fiber consists of cladding the fiber in an analyte-sensitive material. Here, the goal is to utilize the evanescent wave that "leaks" from the core of a fiber to interact with the active environment containing the analyte of interest, yielding a measurable emission of fluorescent light which can be captured as evidence of a species of interest. It is also possible to incorporate the fluorescent species into the fiber itself. The light passing through the fiber excites the fluorescent molecule, and de-excitation occurs through either radiative decay back to the ground state, or non-radiative pathways. The fluorescence will therefore have a characteristic efficiency and rate-of-decay, which can change as a function of the surrounding environment. One example is reference [13], where a fluorescent fiber sensor was demonstrated to quantify cellular dissolved oxygen by its ability to quench the fluorescence in the fiber coating. Active, absorption-based fiber sensors are analogous in design to fluorescent-based fiber sensors. Absorption-based sensors can be either colorimetric, where the detection arises from

changes in the absorption at specific wavelengths in the analyte-sensitive material, or spectroscopic, in which the intrinsic molecular absorptions of the analyte are probed.

PWCS are similar in design to FOCS, but all components must be integrated on a chip. The materials utilized in the design of a PWCS are a result of the three main components of such a device, which must allow the creation, propagation, and detection of photons [14]. The types of light sources that can potentially be used for a mid-IR PIC include various types of light emitting diodes (LEDs) [15], microring lasers [16], quantum cascade lasers (QCLs) [17], and quantum dot (QD) sources [18]. Figure 1.2 shows the envisioned design of such a sensing device:

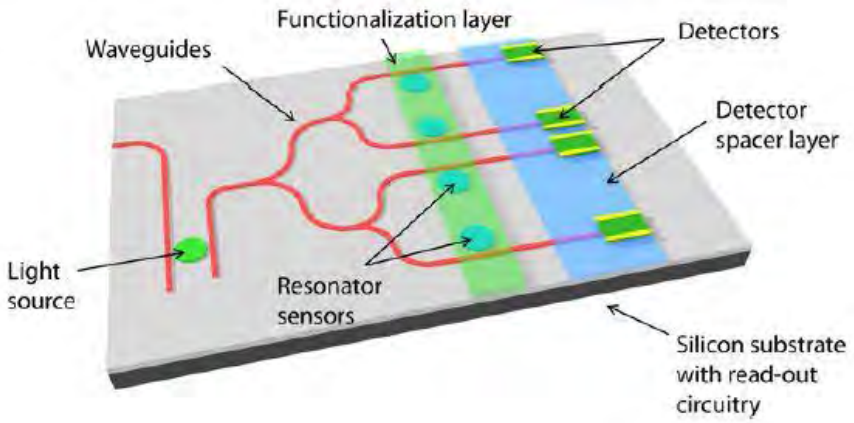

Fig. 1.2: Generic design of proposed chip-based microphotonic chemical sensing device

There are a few basic components of this device, including the light source, waveguides, resonators, detectors, and functionalization layer. The device senses chemicals by characteristic absorptions and/or shifts in the resonant wavelength of the resonator caused by a change in the effective refractive index due to adsorbed species on the resonator. In

the resonator, the light undergoes total internal reflection, and assuming that the loss is low, the light makes many trips around the resonator. This allows the device to be highly sensitive while maintaining a small footprint, and is analogous to a FOCS utilizing many coils of fiber to obtain a long interaction distance between the light and the analyte. Propagation of photons takes place inside of waveguides, and several materials systems have been investigated, including silicon-on-insulator (SOI), suspended silicon, silicon-on-sapphire (SOS), silicon-on-porous silicon (SiPSi), III-V semiconductors, silver halides, and chalcogenide glasses [1].

Several designs of silicon waveguides have been developed. SOI consists of crystalline Si waveguides on top of SiO_2. Si is transparent from 1.1 μm to 8 μm, but device operation is limited to ~4.5 μm due to absorption in the SiO_2 causing loss. Therefore, this platform is ideal for devices operating in the near-IR, because it utilizes mature complementary metal oxide semiconductor manufacturing technology [19,20]. Figure 1.3 shows a sample SOI waveguide structure. The cladding material can be air or SiO_2.

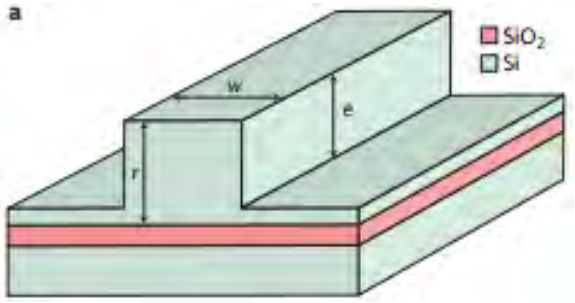

Fig. 1.3: Air-clad SOI waveguide structure, taken from reference [21]

To combat the issue of SiO_2 loss, suspended Si can be fabricated. A layer of Si is grown on an SOI type wafer, and the buried oxide (BOX) is removed below the Si structure,

typically by etching with hydrofluoric acid. The result is a structure made of Si that can transmit light without interaction with SiO_2. A schematic is shown in Figure 1.4:

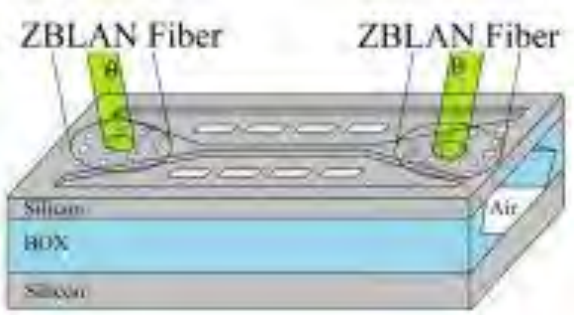

Fig. 1.4: Suspended Si device, taken from reference [22]

Another design that allows longer wavelength operation is SOS, which is similar in design to SOI, except that the SiO_2 substrate material is replaced with sapphire, which transmits to 6 μm. Like SOI, there is a high refractive index contrast between the waveguide and substrate, allowing good confinement of the signal [23,24]. Finally, SiPSi utilizes a silicon waveguide on a porous silicon substrate. This eliminates the lossy SiO_2 material, while maintaining good refractive index contrast due to the porosity of the substrate [25].

Waveguides can be made from other materials, such as III-V semiconductors. III-V semiconductors, such as GaAs, can be integrated simply on the same chip as existing QCL light sources using molecular beam epitaxy. Two such studies have demonstrated this [26,27]. Silver halides are another class of waveguiding materials, which have low Fresnel loss due to relatively low refractive indices (n~2), transparency between 3-30 μm, and are biocompatible [28]. The properties of silver halides can also be tuned, for example, by altering the amount of chlorine in the system $AgCl_xBr_{1-x}$.

Finally, non-oxide, amorphous materials, such as amorphous silicon (a-Si), Si_3N_4 and chalcogenide glasses offer compelling advantages to crystalline materials for waveguides. For example, a-Si has wider integration capability into devices than crystalline Si, and Si_3N_4 is also fully CMOS-compatible and known for its chemical stability and mechanical robustness [6,29]. Chalcogenide glasses (ChGs) are not yet CMOS-compatible, but they have properties that are tunable over a very wide range due to the large glass forming regions of the various chalcogenide glass families. The transmission window of ChGs ranges from visible to far-IR, and varies by composition. The following section will focus on the properties and advantages of ChGs.

1.2.3. Chalcogenide glasses

A glass is defined as an amorphous compound that exhibits a glass transformation upon heating. Formation of a glass vs. crystal is shown in Figure 1.5.

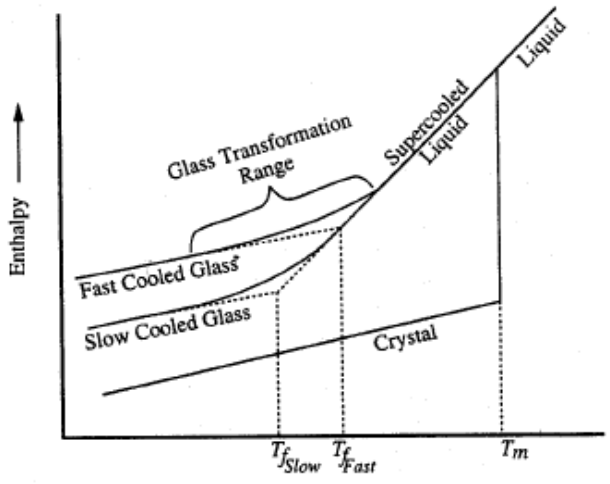

Fig. 1.5: Energy representation of glass transition and melting behaviors, taken from reference [30].

The glass form of a certain atomic composition has higher energy than the corresponding crystalline form. Formation of a glass is often done by rapid cooling of a liquid melt. In this case, a liquid is cooled below the melting temperature, at which point there is a thermodynamic driving force for the material to solidify through crystallization. However, kinetics also play a role in dictating the resultant form of the material, as there is an increase in viscosity as the material is cooled. If the viscosity is high enough, this poses a kinetic barrier that prevents crystallization from occurring, despite the thermodynamic driving force. As such, glasses are metastable materials, and their structures can change over time

through relaxation processes, or controllably crystallized by re-heating near the glass transformation range to form a glass-ceramic.

In Figure 1.5, the fictive temperature, T_f, is the intersection point when the enthalpy lines of the supercooled liquid and glass are extended. T_f is also the point when the structures of the supercooled liquid and glass are the same, and in general is used to describe the difference in thermal history of the fast-cooled and slow-cooled glasses. Glass transition temperature, T_g, is another important characteristic of a glass, which is generally considered to be the point at which the solid glass begins to behave like a viscoelastic material upon heating. T_g can be defined in different ways, such as by characteristic changes in thermal analysis curves measured using differential scanning calorimetry (DSC). Figure 1.6 below shows a fictional DSC curve with relevant features noted, and Figure 1.7 shows an actual DSC curve of $Ge_{23}Sb_7S_{70}$ glass.

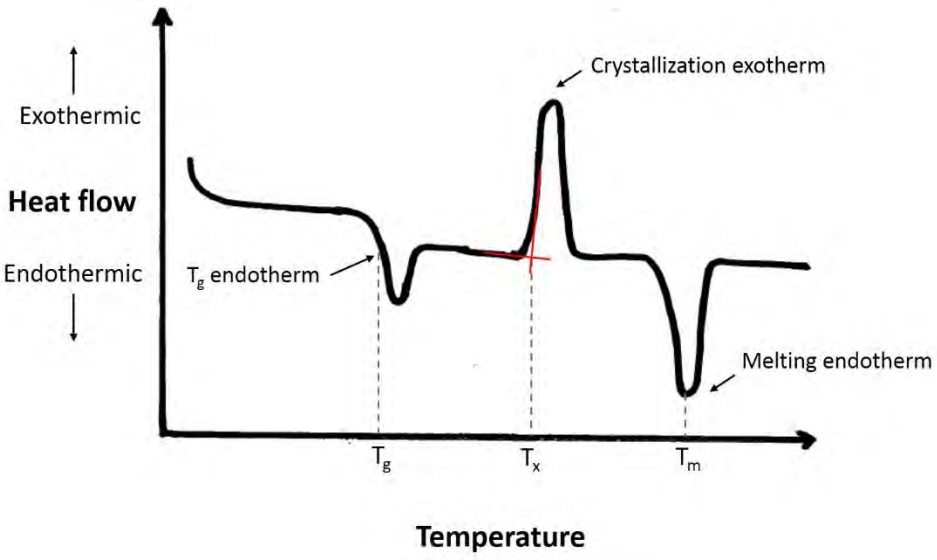

Fig. 1.6: Sample DSC curve showing glass transition, crystallization, and melting features

The glass transition temperature, T_g, is defined here as the inflection point of the glass transition endotherm. T_x is the crystallization temperature onset, which is determined by the intersection point of lines drawn along the baseline of the curve and along the first side of the peak. The melting temperature of the crystal, T_m, is reported as the minimum of this endotherm.

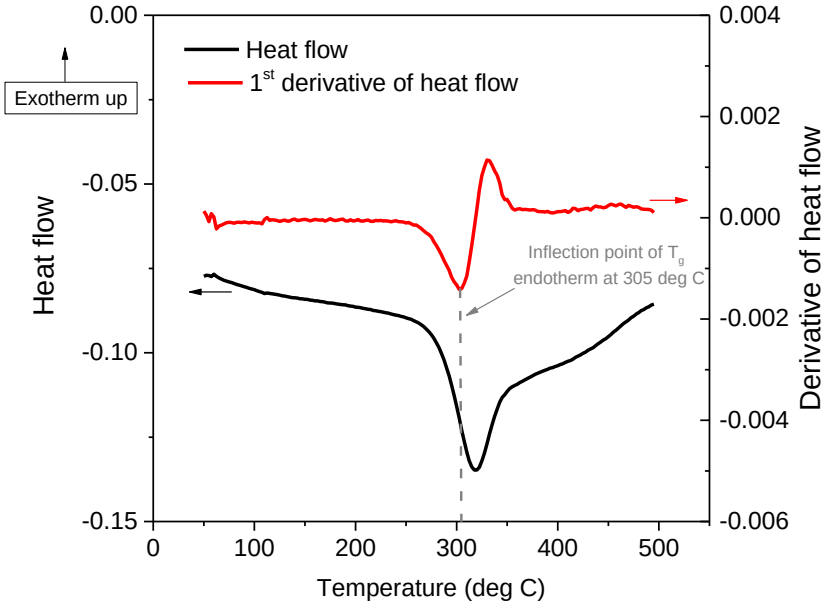

Fig. 1.7: DSC curve of $Ge_{23}Sb_7S_{70}$ glass

From the definition above, the T_g of $Ge_{23}Sb_7S_{70}$ is determined by plotting the first derivative of the heat flow curve, and finding the local minimum, which is at 305°C.

Oxide glasses, such as those based on SiO_2, have been known for thousands of years. This is evidenced by the use of glass beads to decorate Egyptian tombs dated as old

as 7000 B.C., as well as the fabrication of glass tools, containers, and the first optical lenses throughout history. Today, production of glasses still consists primarily of oxide glasses, including high-tech applications such as optical fiber. This comes as no surprise, given the good thermal and mechanical properties and chemical resistance of these materials, as well as the relative ease of fabrication under normal oxygen-containing atmospheres. However, these SiO_2-based materials have high phonon energies, and as a result generally cannot transmit light with wavelength longer than 4 μm. As there is much interest in developing optical systems that can operate in the mid- to far-IR (3-20 μm), there is much research on materials that can transmit light in these ranges, such as chalcogenide glasses.

Chalcogenide glasses are made up of elements from Group VI of the periodic table, including sulfur, selenium and tellurium, with the exception of oxygen. Oxygen, when present, forms M-O bonds which have fundamental absorption in the infrared, reducing material transparency in this spectral window. Elemental starting materials can be purified to remove trace levels of surface oxide, a common impurity that leads to long-wave infrared (LWIR) absorption, or hydrides, which have mid-IR absorption, in order to achieve the best transmission. To the chalcogen species, one or more network formers are added, such as gallium, germanium, arsenic, indium, tin, antimony, and lead. Thus, many chalcogenide glass systems exist due to the broad glass forming regions typically exhibited by such mixtures, and the properties can be finely tuned across these compositions, enabling physical and optical property tailoring. Interest in the optical properties of ChGs began to arise in the 1950s [31], and they are now widely known for their mid-IR transparency and high refractive index due to the heavy elements and high polarizability. As a result of the

need to preclude oxygen from ChG, batching, melting, and annealing must be done in environments that do not contain oxygen. Batching is typically done inside of a nitrogen-purged glovebox into a fused silica ampoule, which is sealed under vacuum for melting and annealing. In commercial applications, ChGs are mainly produced for optics such as lenses, and rewritable phase change memory devices. Current research trends show many promising applications of ChGs as passive components of photonic systems such as optical fiber [32-34], active components for amplification by Raman gain [35-37] or rare earth doping [38-40], and microphotonic waveguides and resonators [41,42].

In order to fabricate microphotonic structures from ChG in film form on a Si wafer or other substrate, the material must first be deposited in film form, and then patterned into the desired structure. There are a few ChG compositions that are particularly promising for microphotonic applications: $Ge_{23}Sb_7S_{70}$, As_2Se_3 and As_2S_3. All compositions have been formed into films using both solution-derived and PVD methods [8,43-45]. The film deposition techniques will be discussed in detail in section 1.2.5.

$Ge_{23}Sb_7S_{70}$ has relatively (for ChGs) strong mechanical properties (Vicker's hardness of 178), high glass transition temperature (T_g = 311°C), and a transmission window spanning 0.55 μm to 10 μm [46]. One of its chief advantages over other ChG compositions is its oxidation resistance, which allows use as an oxidation-resistant overcladding layer in planar photonic devices [10]. Hu et al first studied waveguides made from thermally evaporated $Ge_{23}Sb_7S_{70}$ films in 2007, using plasma etching and lift-off techniques. The high loss observed (3-5 dB/cm) was attributed to the sidewall roughness

of the waveguides [7]. More recently, Chiles et al developed Cl_2 plasma etching of $Ge_{23}Sb_7S_{70}$ from electron-beam deposition, leading to record loss of 0.42 dB/cm [47]. As-S and As-Se are very well-studied ChG systems, which offer generally higher refractive indices (2.80 vs. 2.15 for $As_{40}Se_{60}$ and $Ge_{23}Sb_7S_{70}$, respectively, at 1.55 μm), and high crystallization stability [8,48].

1.2.4. Nanomaterials and Quantum dots

Nanomaterials are usually defined as having dimension less than 100 nm and that exhibit a variation of optical and electronic properties with size [49], making them promising for optical and electronic applications. A notable milestone occurred in 1974, when Norio Taniguchi coined the term "nano-technology" to describe semiconductor fabrication techniques with control on the order of a nanometer.

However, synthetic nanoparticles have existed since the discovery of soluble gold around 1200 BC in Egypt and China [50]. For many centuries, these gold sols were prescribed for the treatment and diagnosis of various diseases. Additionally, the vibrant colors of gold and silver nanoparticles in glass were utilized to make stained glass art, primarily for cathedrals built between the years 500 and 1500. Various colors of glasses could be obtained by precipitating different sizes of gold and silver, which was likely done by subjecting the glasses to different heat treatments. However, despite the realization of these techniques, it was not until the mid-1800s that a scientific understanding of these nano-sized particles started to form, when the work of Jeremias Richters and later, Michael Faraday, showed that the color of aqueous suspensions of gold depends on the size of the

particles [51]. In 1908, Gustav Mie published a theory derived from Maxwell's theory of electromagnetic interaction to explain scattering by particles that have size comparable to the wavelength of the interacting light. Metallic nanoparticles also exhibit a size-dependent surface plasmon resonance absorption, which is the collective oscillation of conduction electrons. Other types of nanoparticles, such as semiconductors, exhibit different size-dependent properties than metallic nanoparticles, which will be discussed in more detail.

The phenomenon of size-dependent properties is often understood as the result of under-coordinated surface atoms, which play an increasing role in determining the properties of the material as it becomes smaller [52]. For example, in the case of spherical PbS nanoparticles, the number of surface atoms varies from about 70% to less than 10% for diameters ranging from 2-20 nm [53]. As a result, the nanomaterials offer the remarkable "bridge" between the properties of bulk materials and the properties of an individual atom. It is therefore possible to create a doped material with extraordinary properties through the incorporation of nanomaterials into a bulk matrix.

Quantum confinement is another size-dependent phenomenon exhibited by certain nanomaterials. Such a nanomaterial is named based on its dimensionality: 0-D quantum dots (QDs), 1-D quantum wires, and 2-D quantum wells. Quantum confinement is observed when the dimension of a material is similar in magnitude to the de Broglie wavelength of the electron wavefunction. As a result, an exciton, which is an electron-hole pair bound by electrostatic force, is confined. The energy spectrum becomes discrete, resembling the structure of a single atom, and the band-gap increases in size as the material becomes smaller. An exciton is formed when a material absorbs a photon or some other form of

energy, exciting an electron from the valence band to conduction band. The electron can then relax through a radiative process (the emission of a photon), which is the mechanism of luminescence. It can also relax through non-radiative processes, such as through phonons, which are atomic vibrations in the lattice of the material. In order to maximize the efficiency of luminescence, which is known as quantum yield and defined in Equation 1.1, it is crucial to minimize the probability of non-radiative de-excitation.

$$Quantum\ yield = \frac{photons\ emitted/second}{photons\ absorbed/second} \qquad \text{(Eq. 1.1)}$$

In the case of QDs, maximum efficiency is achieved primarily through passivation of the surface. For example, a bare QD has defect states due to dangling surface bonds that can lie inside the band-gap and provide a path of non-radiative de-excitation. Figure 1.8 shows schematic representations of different types of QD passivation.

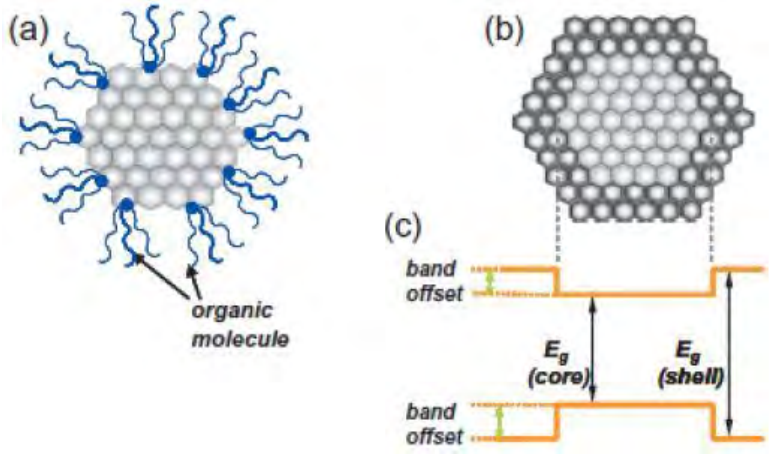

Fig. 1.8: QD passivation types (a) organic and (b) inorganic, with (c) the relative size of band-gaps for the core and shell materials. Taken from reference [49]

QDs can be passivated on the surface by either grafting organic molecules or growing a crystalline layer. In the case of organic passivation, the number of molecules

attached to the surface is limited by steric hindrance, and many dangling bonds remain unsatisfied. Forming a core/shell QD with inorganic passivation can therefore lead to higher quantum yields, because essentially zero QD surface atoms remain unpassivated. For the most efficient and photostable QDs, the band-gap of the shell must be larger than that of the core in order to confine charge-carriers to the core, and also have a lattice parameter within ~12% of the core material to minimize strain [49].

QDs were discovered by the precipitation of semiconductor nanocrystals in a glassy matrix by Alexey Ekimov in 1980 while working at Vavilov State Optical Institute [54,55]. Shortly after, colloidal solutions of QDs were synthesized by Louis Brus at Bell Labs in 1982 [56,57]. Today, QD-doped materials have promising applications in a variety of optical systems, and can be incorporated into glass by both precipitation methods in bulk and film forms of glass and the utilization of colloidal solutions in liquid-based deposition of glass films. Table 1.2 below shows some common Cd- and Pb-chalcogenide QD compositions and their approximate range of attainable emission wavelengths.

Table 1.2: Approximate emission ranges for various compositions of QDs

QD composition	Minimum emission wavelength demonstrated (μm)	Approximate maximum emission wavelength (μm)	Bulk band-gap (eV)	References
CdS	0.250	0.512	2.42	[58]
CdSe	0.320	0.713	1.74	[58]
CdTe	0.570	0.832	1.49	[58]
PbS	0.528	3.024	0.41	[59]
PbSe	1.100	4.593	0.27	[60]
PbTe	1.020	3.875	0.32	[61]

The minimum emission wavelength reported is that which has been demonstrated in previous literature studies. Therefore, it does not represent a physical limit, but rather the

smallest QDs of that composition which have been synthesized thus far. It is possible that any of the listed QD compositions can be synthesized to emit shorter wavelengths than listed in Table 1.2. The maximum emission wavelength in Table 1.2 is equal to the band-gap of the bulk material. Theoretically, this can be approached with large sized QDs, whose band-gap approaches that of the bulk material. For example, in reference [62], 16.9 nm PbSe QDs were synthesized, which had an emission wavelength of 3.54 μm. However, in the same study, the quantum yield also decreased consistently with increasing size of the QDs, from 25% for 7.5 nm QDs emitting at 2.06 μm, to 0.5% for the 16.9 nm QDs.

Most of the work thus far on QD-doped glasses has been in silicate-based compositions. For example, to form Pb-chalcogenide QDs, small amounts of PbO_2 and elemental S, Se or Te are added to a common glass forming melt consisting of SiO_2, and common modifiers such as Na_2CO_3, Al_2O_3 and B_2O_3. The glass is formed by traditional melt-quench techniques, and then heat treated at temperatures where diffusion-controlled precipitation and growth of QDs takes place. Figure 1.9 shows absorption spectra of PbS grown in a silicate glass.

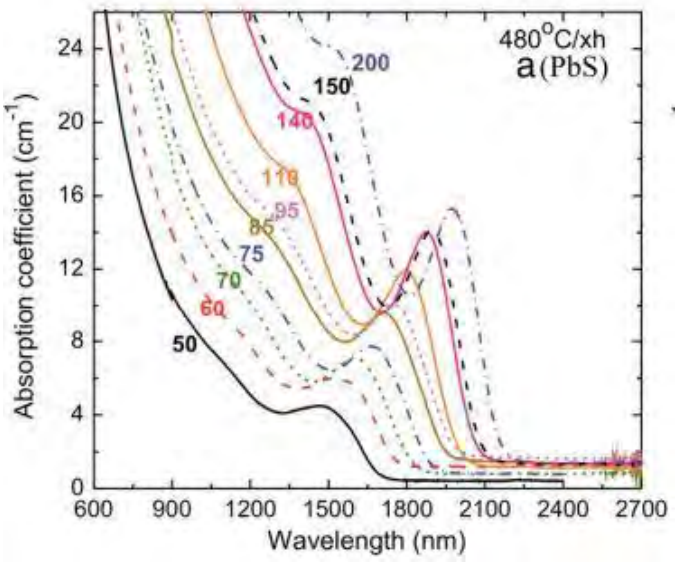

Fig. 1.9: Absorption spectra of PbS-doped glass heat treated for varying lengths of time (in hours), taken from reference [63]

This demonstrates the quantum confinement effect, as the smaller crystals have larger (in energy) band-gaps. Several other studies have demonstrated similar QD growth in bulk silicate glasses [64], as well as bulk germanate glass [65,66], and characterized the luminescent properties of the QDs. Such materials are attractive for utilization as fiber amplifiers [67,68], saturable absorbers for lasers [69], and ultra-short pulse generation [70].

In film form, applications of QD-doped glasses include photovoltaics and sensing devices. There are a few different methods that can be used to fabricate QD-doped glass films, briefly summarized below.

- QDs can be precipitated in glass films in a similar manner as utilized in bulk glass [71]. For example, Pb and S precursors, such as lead acetate trihydrate and ammonium thiocyanate, respectively, can be added to sol-gel derived amorphous

zirconia films [72]. After deposition, the films are heat treated to precipitate nanocrystalline PbS.

- A previously-prepared QD solution can also be mixed with a sol-gel solution [73]. In this case, there is greater control over QD size, shape, passivation, and concentration, because more flexibility is allowed by colloidal QD synthesis methods in solution than QD precipitation from a glass matrix.
- Additionally, reaction of a precursor-containing film with a precursor gas can allow the precipitation of semiconductor nanocrystals. For example, this was done by reaction of H_2S gas with silica xerogels containing Pb^{2+} ions to produce PbS QDs [74].

As is often the case, principles and process techniques are first learned in silicate-based glasses before application to ChGs. The approach whereby previously synthesized QDs are mixed with a glass solution is the only method explored in this dissertation. This is because crystallization in bulk ChGs is a young field, without much information on the precipitation of nanocrystals. Theoretically, this could be done in a thermally evaporated ChG film doped with Pb, and then subjected to further heat treatment to precipitate nanocrystals. Additionally, in reference [74], it was found that temperatures of 250°C were required for reaction of Pb^{2+} and H_2S, which would deteriorate the properties of most ChGs, including $Ge_{23}Sb_7S_{70}$.

Thus far, there are only a few publications that report the incorporation of nanoparticles into ChG films. Kovalenko et al utilized inorganically functionalized core-shell PbS/CdS QDs to observe strong near-IR luminescence, but did not comment on the

dispersion of the QDs in the film matrix [75]. Novak et al studied the incorporation of organically capped PbS and core-shell CdSe/ZnS QDs in spin-coated $Ge_{23}Sb_7S_{70}$ films, observing visible and near-IR luminescence, as well as aggregation of the QDs in the deposited film [76]. Finally, Lu et al developed a method of laser ablation of a silver target inside of an As_2S_3/propylamine solution to achieve uniform dispersion of Ag-nanoparticles in spin-coated As_2S_3 films [77].

1.2.5. Film deposition techniques

Several methods of ChG film deposition have been demonstrated, including thermal evaporation (TE) [8,78], pulsed laser deposition (PLD) [8], and radio frequency magnetron sputtering from bulk glass targets [79], as well as solution-based approaches like spin-coating (SC) [80] and sol-gel [81]. Film deposition techniques are grouped into two categories: physical vapor deposition (PVD), and solution-derived approaches. The most common PVD methods are thermal evaporation (TE) [8,78] and pulsed laser deposition (PLD) [8]. TE consists of heating a boat containing pieces of bulk ChG under low pressure (~10^{-6} torr) until a suitable vapor pressure of the ChG is reached. A cold substrate is then exposed, upon which a film condenses from the ChG vapor. PLD is similar to TE, except that the vapor is formed by ablating the material with short, high power pulses. The advantage of PVD methods is that the films are dense, non-porous, and have a refractive index very close to that of bulk glass, but they suffer from inhomogeneity due to varying volatilization rates of the components [8,43]

In solution-derived methods, an appropriate solvent is used to dissolve bulk glass (usually powdered), and a thin layer of this solution is formed on the substrate by spin-coating [80] or dip-coating before heat treating to drive off the solvent. The solvents usually used for ChG dissolution are various types of amines. Solution-derived approaches generally require less expensive equipment than needed for PVD methods, can coat large areas quickly, and do not suffer from inhomogeneity issues [43,82]. The main disadvantage of solution-based ChG film processing is that the residual solvent cannot be removed

totally, and as a result, the infrared transmission and refractive index are both reduced due to the organic material bonded into the film matrix. In fact, the structure of a spin-coated $Ge_{23}Sb_7S_{70}$ film is more similar to the propylamine-based solution than that of the bulk glass. This was demonstrated by Waldmann et al, where it was found that the building blocks of the bulk glass, GeS_4 tetrahedra, rearrange to form $Ge_4S_{10}^{4-}$ clusters during dissolution in propylamine, with the negative charge of these clusters compensated by n-propylammonium ions, $C_3H_7NH_3^+$ [83]. Raman spectra from this study of the bulk glass, film, and solution are shown in Figure 1.10.

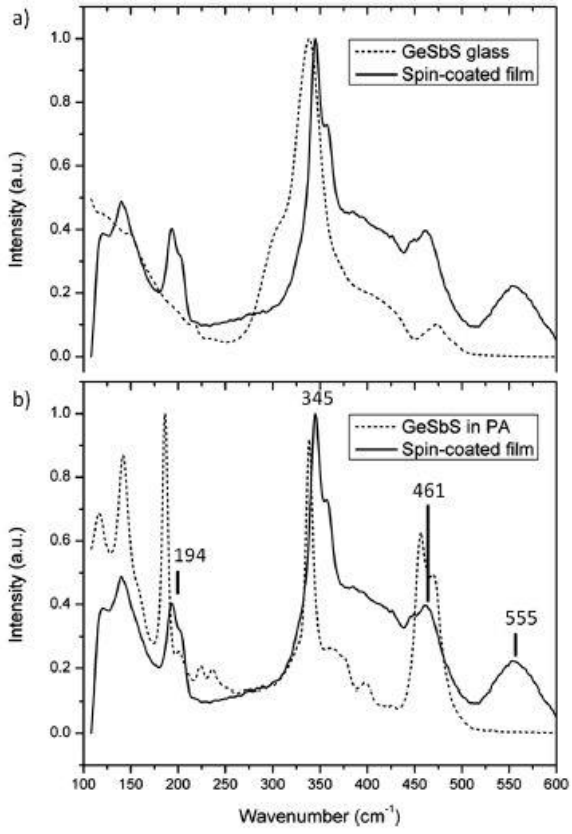

Fig. 1.10: Raman spectra of $Ge_{23}Sb_7S_{70}$ in the form of bulk, spin-coated film, and propylamine-based solution, taken from reference [83]

In another study, it was shown that annealing solution-derived $Ge_{23}Sb_7S_{70}$ enables the structure of the film to move closer the structure of the bulk, but is still different despite annealing at 270°C, which is just 40°C below T_g of the bulk glass, shown in Figure 1.11.

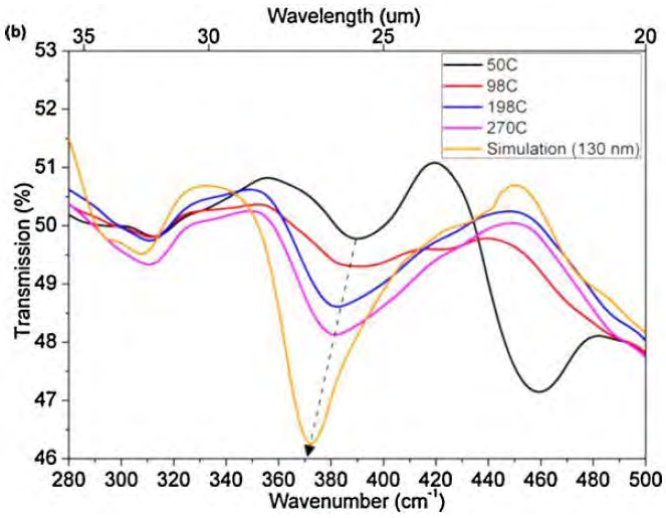

Fig. 1.11: Far-IR transmission spectra of $Ge_{23}Sb_7S_{70}$ films made by spin-coating, taken from reference [43]

This simulation is done using the properties of the bulk glass, and the peak at 370 cm^{-1} is due to GeS_4 tetrahedra with four bridging sulfurs. As the spin-coated film is annealed, the 370 cm^{-1} peak increases, and the structure gets closer to that of the bulk glass, but it is still not fully consolidated. Furthermore, in reference [84], it was found that the refractive index of $Ge_{23}Sb_7S_{70}$ films heat treated at temperatures up to 210°C reached 2.02 at long wavelength, whereas the refractive index of bulk glass is 2.21.

Despite some of the inherent disadvantages of solution-derived ChG film deposition, a unique advantage of solution-based ChG film deposition is simple incorporation of nanoparticles, which can enhance properties or create new functionalities

in a material. A ChG film can be doped with nanoparticles by mixing the two solutions together prior to deposition. This has been demonstrated in two publications, both studying the incorporation of quantum dots for their luminescent properties [75,76]. In comparison, there are no publications on nanoparticle doped ChG films made by thermal evaporation or similar methods utilizing a bulk glass target.

Electrohydrodynamic spraying, which is more commonly called electrospray, is a method of droplet generation and charging by means of an electric field. This method was first discovered by Zeleny in 1915 [85]. In general, the process consists of applying a potential difference, on the order of several thousand volts, between a liquid-filled capillary and a target. Due to the electric field, a shear stress is applied to the liquid, which elongates into a jet. The jet disintegrates into droplets due to Rayleigh instability. The droplets are highly charged, and as a result are self-dispersing in space due to Coulombic repulsion. Different modes are possible, such as dripping, microdripping, cone-jet and multi-jet, amongst others. Figure 1.12 shows schematics of the most common electrospray modes.

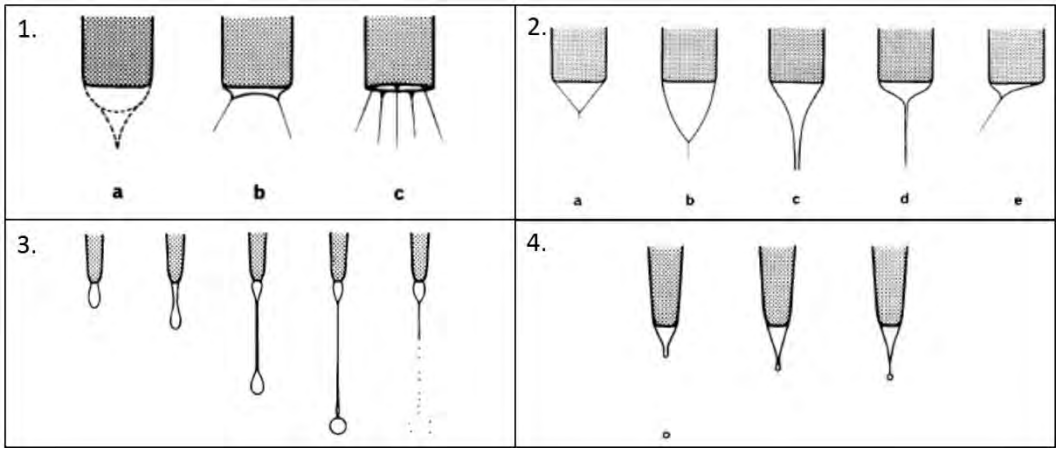

Fig: 1.12: Variations of cone-jet mode: a) pulsed cone-jet b) and c) multi-jet. 2. Variations in meniscus forms for cone-jet mode a) through e). 3. Sequence of

stages during dripping mode. 4. Sequence of stages during microdripping mode. Taken from reference [86]

In general, the cone-jet mode with single jet (Fig 1.12_2) tends to be the most useful and widely studied. This is because it allows a narrow size distribution of droplets, which can be tuned over a wide range, including submicron diameters. It is often called the "Taylor cone" due to the first demonstration of electrostatic pressure and capillary pressure balanced at any point on the surface of a liquid cone [87]. Several applications of this electrospray technique have been studied, such as film deposition and nanoparticle synthesis [88,89], but currently the only widespread application is electrospray ionization mass spectrometry [90], for which John B. Fenn was awarded the Nobel Prize in Chemistry in 2002. Electrospray has been used to deposit films of various materials, such as nuclear materials [91], organic [92], inorganic [93], but never ChGs. Electrospray can add additional flexibility in the deposition of films compared to spin-coating and PVD methods, which poses some interesting advantages for ChG microphotonics. These potential advantages include localized deposition, similar to a printing method, the ability to fabricate non-uniform thickness films, and possibly better nanoparticle dispersion.

Directly fabricating complex geometries of ChG is not easily possible with spin-coating or PVD methods of film deposition, as they are blanket film techniques. Current methods of integrating ChG structures into planar devices all begin with deposition of a blanket film, and then various lithography techniques are utilized to form the ChG structure, such as a waveguide or resonator. During deposition of the blanket film by PVD, some material is wasted by "missing" the substrate, and in the case of spin-coating, as much

as 95% of the solution is wasted by spin-off [92]. Furthermore, the blanket film is also used inefficiently, as the vast majority of the film is etched away to fabricate the structures. Therefore, the ability to deposit ChG selectively, at the location where the structures will be fabricated on the substrate, provides large raw material cost savings. As a result, the advantage of localized deposition using electrospray allows the possibility of much more efficient use of material. In the case of blanket film deposition by electrospray, nearly 100% of the solution can be used because there is no run-off. Furthermore, if only part of the substrate needs to be coated, electrospray can be used to target this specific location, whereas other techniques would coat the entire area. Electrospray is also more suitable than spin-coating for scaled up, roll-to-roll manufacturing because it is a continuous process.

II. EXPERIMENTAL

While Chapter I highlighted the prior art and background specific to this dissertation, Chapter II will describe the experimental techniques utilized to fabricate and characterize the properties of these samples. Based on the desired characteristics of a ChG film proposed for use in a planar microphotonic chemical sensing device, the experimental methods can be classified into several categories.

- How are the starting materials prepared?
    - Preparation of bulk glass
    - Preparation of a solution from the bulk glass and organic solvent suitable for film deposition by spin-coating and electrospray
- Do the films have the required properties for use in a sensing device, and how can they be achieved in an electrosprayed film?
    - Low-loss: mid-IR transmission and surface roughness
    - Composition and refractive index
    - Target thickness and uniformity
- What are the unique and novel functionalities that can be created with multi-layer electrosprayed films and QD-doped films?
    - Multi-layer GRIN
        - Refractive index across the film
        - Interface between the two layers
        - Surface quality of a multi-layer film
    - QD-doped

- Luminescence emission range
- Luminescence efficiency
- Arrangement of the QDs on the nanoscale

2.1. Fabrication of bulk glass and dissolution

Fabrication of ChGs consists of a traditional batch, melt, quench, and anneal process. These steps must all be done in an inert atmosphere in order to avoid contamination by oxygen, which would degrade the optical properties, especially reduction of the infrared transparency. Therefore, elemental starting materials are batched into a fused silica ampoule inside of a nitrogen-purged glovebox, then vacuumed for four hours at 90°C to drive off any residual moisture. While under vacuum, the ampoule is sealed with a gas-oxygen torch, and the batch can then be melted in a rocking furnace, typically for 16 hours to allow complete homogenization. Three compositions were explored in this dissertation, $Ge_{23}Sb_7S_{70}$, which was melted at 850°C, As_2S_3, which was melted at 700°C, and As_2Se_3, which was melted at 700°C. Glasses were quenched by removing from the furnace and holding the ampoule upright in air until the sample pulled away from the sides of the ampoule. Glasses were annealed for 16 hours at 40°C below the glass transition temperature (T_g). T_g for $Ge_{23}Sb_7S_{70}$ is 311°C [46], 197°C for As_2S_3 [94], and 191°C for As_2Se_3 [95].

In order to make a solution of ChG, bulk material is crushed into a powder with a mortar and pestle. The powder is then mixed with an amine solvent, and dissolution can be

expedited with stirring and gentle heating on a hotplate with a surface temperature of about 40°C. These solutions were then used to deposit films by spin-coating and electrospray.

2.2. Deposition of films by spin-coating

The spin-coating process of film deposition used in this dissertation was identical to a prior optimization in our group [43]. Propylamine solvent was combined with 3 angstrom molecular sieve and let to sit overnight in order to remove residual water from the solvent. $Ge_{23}Sb_7S_{70}$ glass was dissolved in the propylamine at a concentration of 0.05 g/mL, with 3.4 μL of water added per mL of solution, which was found to improve solubility and film surface quality in the same study [43]. Inside of a nitrogen-purged glovebox, the solution was dripped on a borosilicate glass microscope slide or Si wafer substrate, and spun for 10 s at 3000 rpm with a 5 s acceleration time using a Model G3 spin-coater by Specialty Coating Systems. Films were soft-cured at ~50°C on a hotplate and then vacuum baked at a pressure of about 30 in Hg below atmospheric pressure according to the following table.

Table 2.1: Annealing protocol of spin-coated $Ge_{23}Sb_7S_{70}$ films

HT0	5 min on hotplate at 100°C
HT1	1 h at 100°C
HT2	1 h at 125°C
HT3	1 h at 150°C
HT4	1 h at 175°C
HT5	1 h at 200°C

2.3. Deposition of films by electrospray

Figure 2.1 shows a schematic and photograph of the electrospray system.

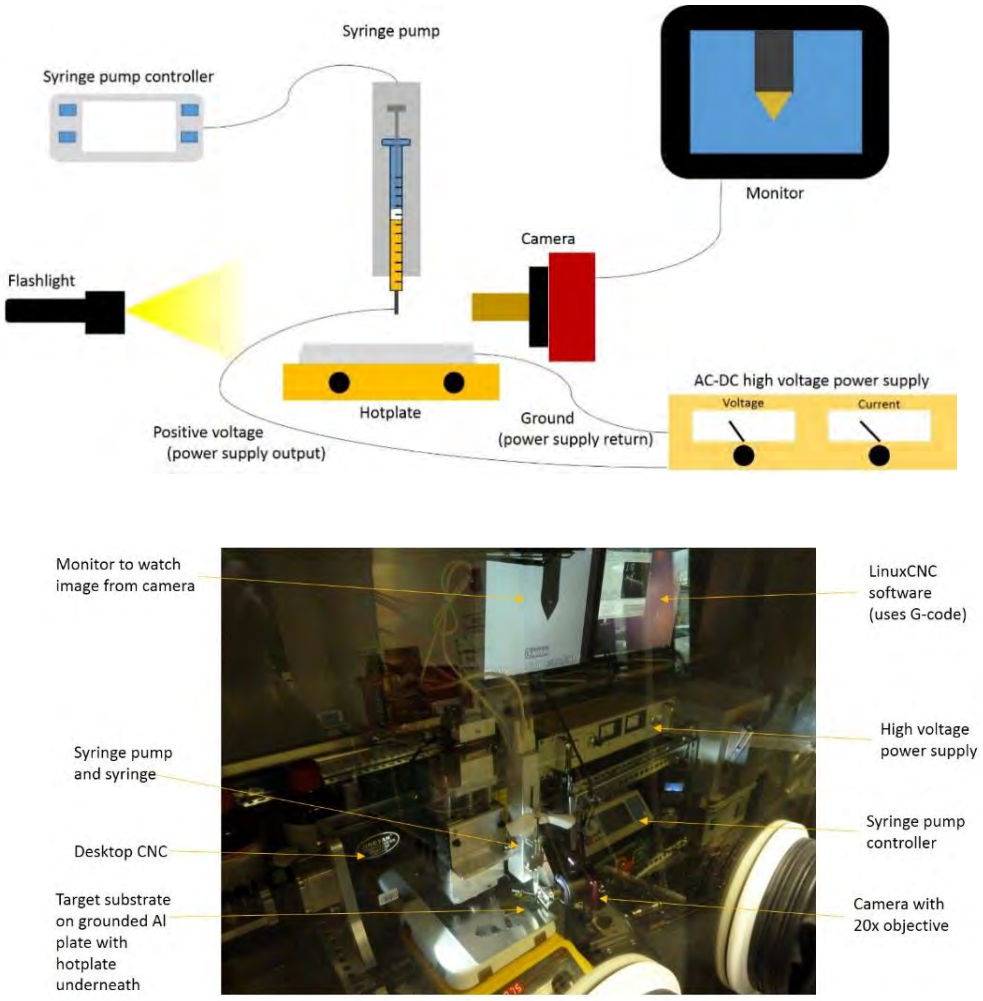

Fig. 2.1: Schematic (top) and photograph (bottom) of electrospray system

Electrosprayed films were fabricated using $Ge_{23}Sb_7S_{70}$ of As_2S_3 glass dissolved in ethanolamine at a concentration of 0.05 g/mL. The solution was loaded into a 50 µL syringe by using a syringe pump in extraction mode at 150 µL/hr. This low extraction rate was

used in order to prevent the formation of bubbles. The syringe is a removable needle style, with a 26s gauge cone-tip needle shown in Figure 2.2.

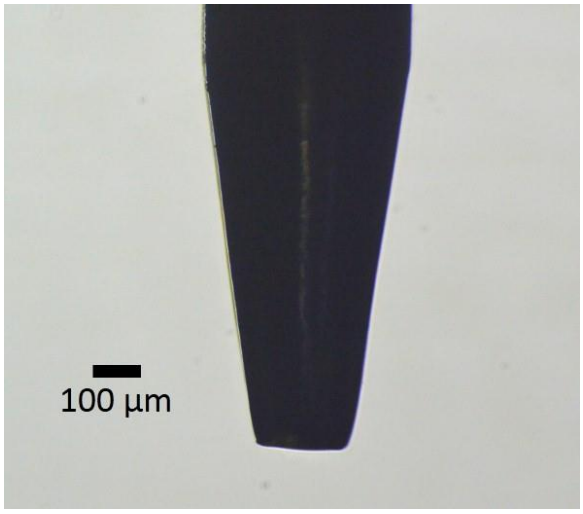

Fig. 2.2: Cone-tipped needle used for electrospray experiments

No special advantages were observed from using a cone-tip needle. Initial experiments were done with a 30 gauge (300 µm) outer diameter straight, blunt needle on a Luer type syringe. This setup tended to trap bubbles in the corners where the syringe meets the needle, which is worsened by the relatively large "dead space" volume between the plunger and the solution. A comparison between the removable needle type and Luer type syringes are shown in Figure 2.3.

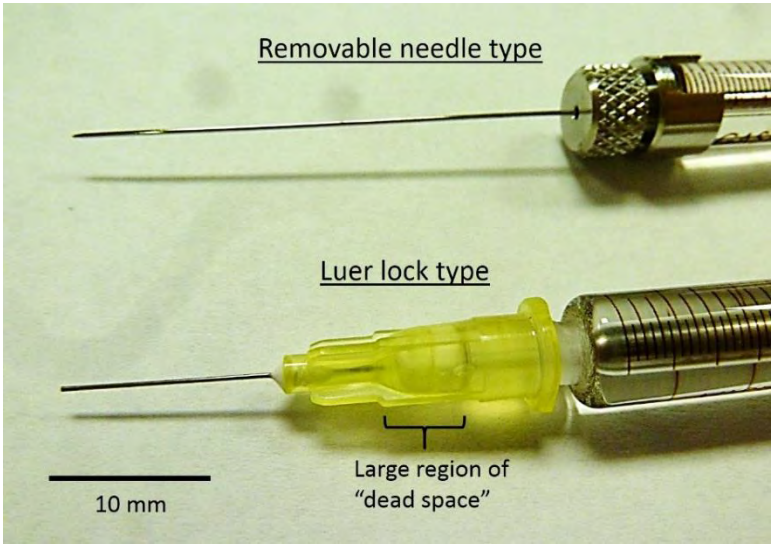

Fig. 2.3: Comparison between removable needle type syringe and Luer lock type syringe

In order to solve the bubble issue, a removable needle type syringe was used in order to reduce the places where bubbles can become trapped in the dead space when drawing solution into the syringe. The cone-tip needle was the only off-the-shelf option for a removable needle type syringe, with a similar outer diameter to the 30 gauge Luer needle used in the proof-of-concept electrospray experiments.

To evaluate the basic processing protocol of the method, electrospray deposition took place in a fume hood with ambient atmosphere, despite the possibility of introducing oxygen to the system. The electrospray deposition was set up vertically with a working distance of 4-15 mm between the needle and a Si wafer. Hotplate surface temperature was varied depending on the flow rate, glass composition and working distance, and was typically in the range of 50-80°C. Flow rate was set in the range of 10-25 μL/hr, and a DC high voltage power supply was tuned until a stable Taylor cone was formed [87]. The

needle and spray is viewed live using a 20x, 1 cm working distance microscope objective attached to a Nikon J3 camera.

Current flow of the electrospray was measured with a multimeter. One lead was attached directly to the target substrate, which was placed on a non-conducting surface, and the other lead was attached to the power supply return (ground). Assuming that all charge flows through the multimeter, the current flow during electrospray, I_{ES}, can be determined using Ohm's law, where v_{meas} is the measured voltage of the multimeter, and R_{int} is the internal resistance of the multimeter.

$$I_{ES} = \frac{V_{meas}}{R_{int}} \qquad \text{(Eq. 2.1)}$$

Conductivity of the solutions were also measured with a multimeter. A small piece of non-conducting material was constructed to hold the leads a constant distance apart, and placed into a vial of the solution to record resistance. The resistance of deionized water was also measured using a calibrated conductivity probe (which could not be used to test the ChG/amine solutions because they would damage the probe). The conductivity of the ChG solutions was estimated by the following relationship, where σ_s is the conductivity of the sample, R_s is the measured resistance of the sample, R_{ref} is the measured resistance of the reference, and ρ_{ref} is the absolute resistivity of the reference.

$$\sigma_s = \frac{R_{ref}}{R_s \rho_{ref}} \qquad \text{(Eq. 2.2)}$$

2.4. QD doping

The stock QD solution was 0.6 mg/mL CdTe QDs with mercaptopropionic acid capping agent, dispersed in ethanolamine solvent. This solution was prepared by Dr. Manashi Nath's group at Missouri S&T. In addition, commercial CdSe/ZnS core-shell QDs capped with octadecylamine were tested, which were purchased from Ocean NanoTech in powder form. These QDs were dispersed in ethanolamine at a maximum concentration of 0.3 mg/mL.

In order to make QD-doped films by spin-coating and electrospray, these QD suspensions were mixed with a 0.05 g/mL $Ge_{23}Sb_7S_{70}$/ethanolamine solution in a 1:10 volume ratio, or by dissolving the $Ge_{23}Sb_7S_{70}$ glass directly in the QD suspension. For the CdTe QDs, the solution used for film deposition by both electrospray and spin-coating containes 0.06 mg/mL QD concentration, and 0.045 g/mL $Ge_{23}Sb_7S_{70}$. For the CdSe/ZnS core-shell QDs, $Ge_{23}Sb_7S_{70}$ was dissolved at a concentration of 0.05 g/mL, in QD suspensions ranging from 0.01 to 0.3 mg/mL.

2.5. Characterization of properties

Several metrics were used to analyze the properties of the films in this dissertation.

Optical properties:

Refractive index was measured using both ellipsometry (Woollam and Associates ESM-300) and by taking reflectance spectra with a Filmetrics F20 instrument. Ellipsometry determines the optical constants of a material by analyzing the polarization change of light due to interaction with the sample. The Filmetrics instrument determines refractive index

by fitting the interference fringes of the reflection spectrum with thickness and refractive index. Both parameters can be fixed to a range or specific value to more accurately determine the other parameter.

Fourier transform infrared spectroscopy (FTIR), is a method of analyzing the response of a material to mid- and far-infrared light. This response can be tested in transmission, reflection, or attenuated total reflectance (ATR). In ATR mode, the light is traveling inside of a high refractive index crystal, often diamond, and thus undergoes total internal reflection (TIR) when in contact with a lower refractive index sample. When TIR occurs in the instruments ATR crystal, there is an evanescent component of the light that "leaks" into the sample, interacting with the sample to a depth on the order of microns.

FTIR spectroscopy uses a broadband light source, often a SiC filament that acts like the filament of an incandescent light bulb. This broadband spectrum is modified using a Michelson interferometer, shown in Figure 2.4.

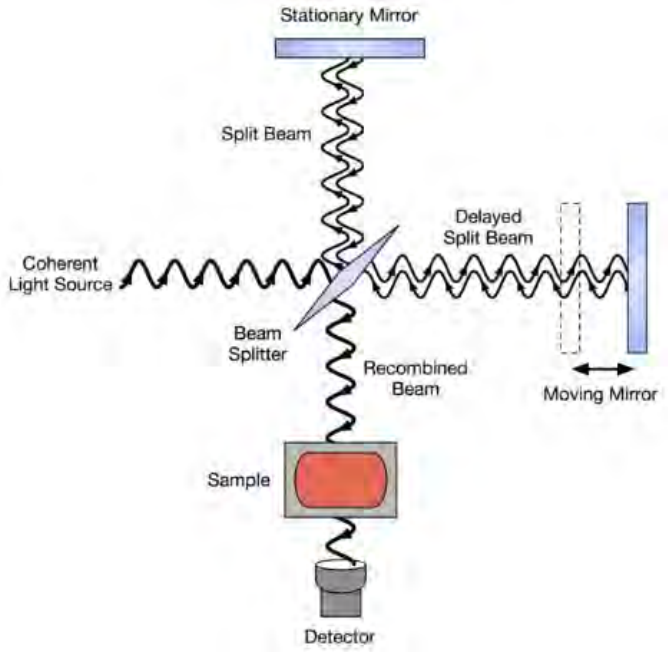

Fig. 2.4: FTIR spectrometer set-up with Michelson interferometer, taken from reference

A mirror is moved using a motor such that certain wavelengths from the broadband source are eliminated due to destructive interference depending on the position of the beam splitter. As a result, the spectrum of light that reaches the sample is modified differently at each moment. The detector records the intensity of light at each beam splitter position, and the full transmission spectrum of the sample is reconstructed using a Fourier transform.

In this dissertation, FTIR spectra were taken with a Thermo Scientific Nicolet IS5 spectrometer in both transmission mode and ATR mode. As films were deposited on undoped Si substrates, which have good transparency in the mid- and far-IR, they were analyzed in transmission mode. Liquid samples, such as amine solvents and ChG solutions were analyzed in ATR mode. The Nicolet IS5 has a usable range of approximately 7000

cm^{-1} to 500 cm^{-1} (1.43 μm to 20 μm). Typical instrument settings for the transmission measurements were 128 accumulations and resolution of 4 cm^{-1}.

Surface analysis:

Film surfaces were characterized using a few different metrics. Film thickness and surface profile was measured using a Dektak XT contact profilometer. This contact profilometer works by moving the sample stage beneath a tip in contact with the sample surface. The texture of the surface is determined by changes in the tip height, which are determined by a linear variable differential transformer. The tip size was 2 μm in diameter, stylus force was 3 mg, and scan rate was typically 100 μm/s. To measure thickness, the film was scratched down to the substrate, and step-height was determined. The contact profilometer was also used to determine film profiles. This was done by doing a scan with length 5-10 mm over a film, starting on uncoated substrate on one side of the film, scanning over the film, and ending on the uncoated substrate on the other side. In order to account for variations in the substrate thickness, averages of a few surface profiles (typically three) were used.

Surface roughness was measured with a Zygo NewView 8300 white-light interferometer. The following information is a general explanation on white-light interferometery, and is not a specific description of the Zygo 8300. A schematic of a white-light interferometer is shown in Figure 2.5.

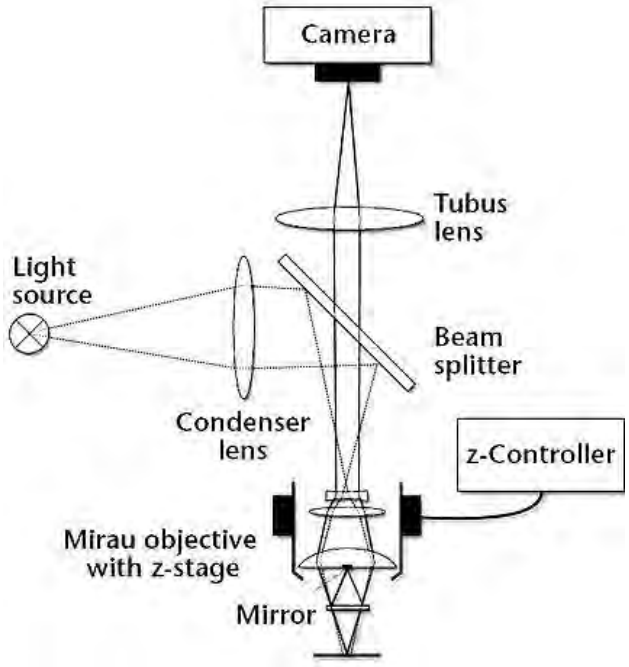

Fig. 2.5: Schematic of a white-light interferometer surface analysis system, taken from reference [96]

The light travels through a beam splitter, which directs some light toward the sample, and some light toward the camera as a reference beam. After reflecting off the sample, different points can have different phases due to the texture of the sample surface. As a result, the camera sees an interference pattern when the reference beam recombines with the light that has interacted with the sample. This interference pattern is then analyzed by the software to determine the topography of the sample.

Electron microscopy:

Scanning electron microscopy (SEM) and transmission electron microscopy (TEM) were utilized to image the samples. In the case of SEM, an electron beam is scanned over the surface of the sample, and secondary electrons emitted by atoms excited by the electron

beam are collected. Contrast is created by the topography of the sample, as well as by differences in density and atomic number. Two different SEMs were utilized, including a Zeiss Ultra-55 FEG and a JEOL JSM 6480. The Zeiss was used primarily for imaging, while all energy-dispersive x-ray spectroscopy (EDX) compositional analysis was done using the JEOL.

TEM was done with a FEI Tecnai F30. Samples were prepared by electrospraying for a short period of time, usually five seconds, on ultra-thin carbon TEM grids, or by using an FEI 200 focused ion beam instrument to lift-out a slice of a blanket film and attach it to the post of a half-grid for TEM analysis. The FEI 200 utilizes a 30 kV gallium ion beam to mill the sample.

Photoluminescence (PL):

Luminescence is cold-body radiation of light. In general, luminescence describes the process by which an electron is excited into a higher energy state, and then relaxes to a lower energy state through the emission of a photon. This is in contrast to thermal radiation, which is the electromagnetic radiation emitted by all objects with temperature greater than absolute zero. Thermal radiation is a result of interatomic collisions that cause the kinetic energy of the atoms to change, and is the method of light generation in an incandescent light bulb, for example. In the case of cold-body radiation, there are many ways by which excitation can be provided to a luminescent material, such as the absorption of a photon (photoluminescence), the passing of an electric current (electroluminescence), or a mechanical action (mechanoluminescence), to name a few.

In the experiments in this dissertation, photoluminescence was utilized to study the luminescent behavior of quantum dots. Figure 2.6 below shows a schematic of the system belonging to Dr. Mercedeh Khajavikhan's group.

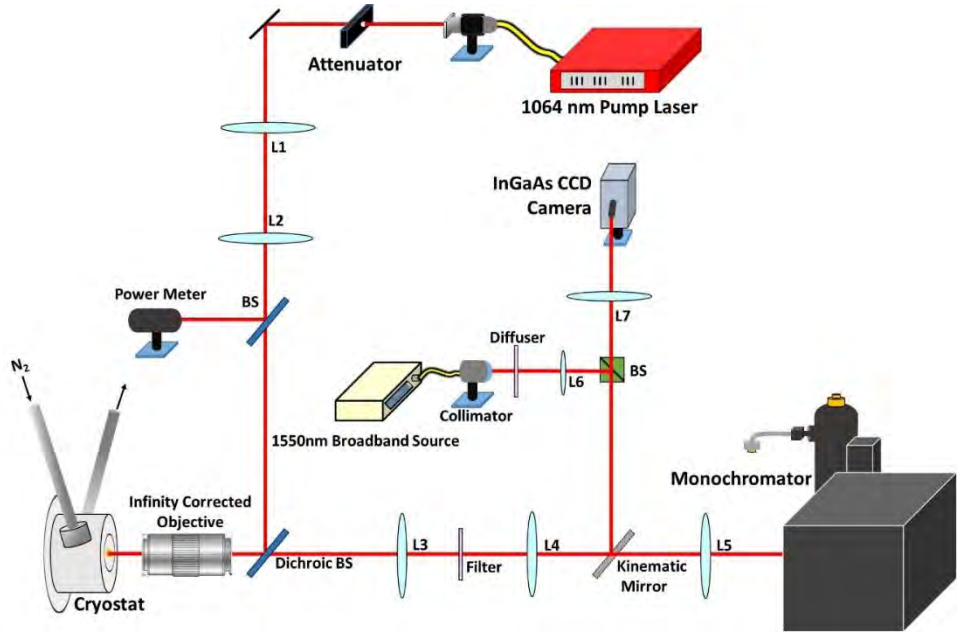

Fig. 2.6: Schematic of home-built photoluminescence system in Dr. Mercedeh Khajavikahn's group

The excitation source in this system can be changed between 1064, 633, or 532 nm. Photoluminescence was also tested using an Ocean Optics QE Pro FL for detection, in conjunction with a 532 nm laser pointer with power of approximately 1.5 mW as an excitation source. This system utilizes a fiber and collimating lens positioned near the sample to collect the signal, with no other optics used. In addition, a 27 lumen blue LED with emission centered at approximately 449 nm and having full width at half maximum of 20 nm, was also used as an excitation source for the QE Pro FL.

III. CHALCOGENIDE GLASS FILM DEPOSITION BY ELECTROSPRAY

Based on the experimental procedures described in Chapter II, this chapter will discuss optimization of undoped ChG film deposition by electrospray. This includes selection of an optimal solution from the several glass compositions and solvents that have been previously studied for spin-coated films, as well as investigations of ideal electrospray process parameters. In addition, a method of obtaining uniform thickness films by electrospray was developed, and a detailed investigation of the evolution of film properties during solvent removal by heating under vacuum was carried out. Two glass compositions were studied, $Ge_{23}Sb_7S_{70}$ and As_2S_3, and this allowed the fabrication and characterization of multi-layer GRIN films using a non-uniform thickness coating of each composition.

A general comparison overview between films deposition by electrospray and spin-coating is shown in Table 3.1 below.

Table 3.1: General advantages of each deposition process

Advantages of electrospray	Advantages of spin-coating
Localized deposition using CNC control	Can use non-conductive substrate
Simple method of GRIN fabrication with multilayer films or simultaneous deposition	Quick and simple to get uniform thickness films over large areas
Continuous, roll-to-roll processing with little wasted material	Minimal investment in equipment

Each process has key advantages and disadvantages. Spin-coating is generally preferred for the deposition of uniform thickness films up to 1 μm thick (for Ge-Sb-S) or a few μm thick (for As-S and As-Se). Electrospray is generally more complex for the deposition of uniform thickness films due to the need for computerized numerical control (CNC), but

theoretically there is no upper limit to film thickness. Electrospray also can allow localized deposition (2-D and 3-D printing), and a simple approach to the deposition of GRIN films, but does suffer from the requirement that the target substrate must be electrically conducting.

3.1. Selection of appropriate solution

To our knowledge, no previous work has been done on the electrospraying of ChGs. Initially, our aim was to explore electrospray as a method of "printing" select geometries of ChG films, for the advantages of localized depositions, efficient use of material, roll-to-roll processing and simple GRIN fabrication. ChG electrospray proof-of-concept was done in a fume hood under ambient atmosphere. Definitions of electrospray processing parameters are shown in the schematic and table below.

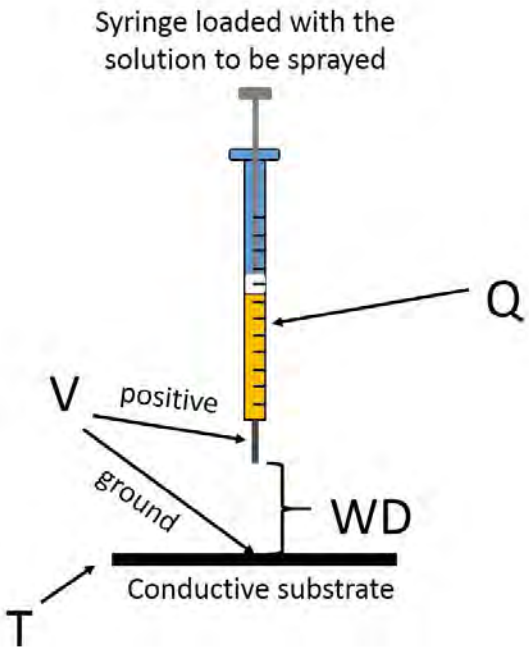

Fig. 3.1: Schematic representation of basic electrospray process parameters

Table 3.2: Definitions of basic electrospray process parameters

Process parameter	Definition
Q	The volumetric flow rate of the solution, which is controlled by a syringe pump.
V	The applied voltage, which is positive and DC in our system, between the nozzle and target substrate. V is set by an AC-DC power supply.
WD	The working distance between the end of the nozzle and the top of the substrate.
T	The substrate temperature during deposition, which is controlled with a hotplate.

First attempts to electrospray ChG were made using 0.05 g/mL $Ge_{23}Sb_7S_{70}$ dissolved in propylamine. It was found that the solution could be electrosprayed and films were formed. However, stability of the spray was poor, and tended to cycle through different spraying modes, shown in Figure 3.2.

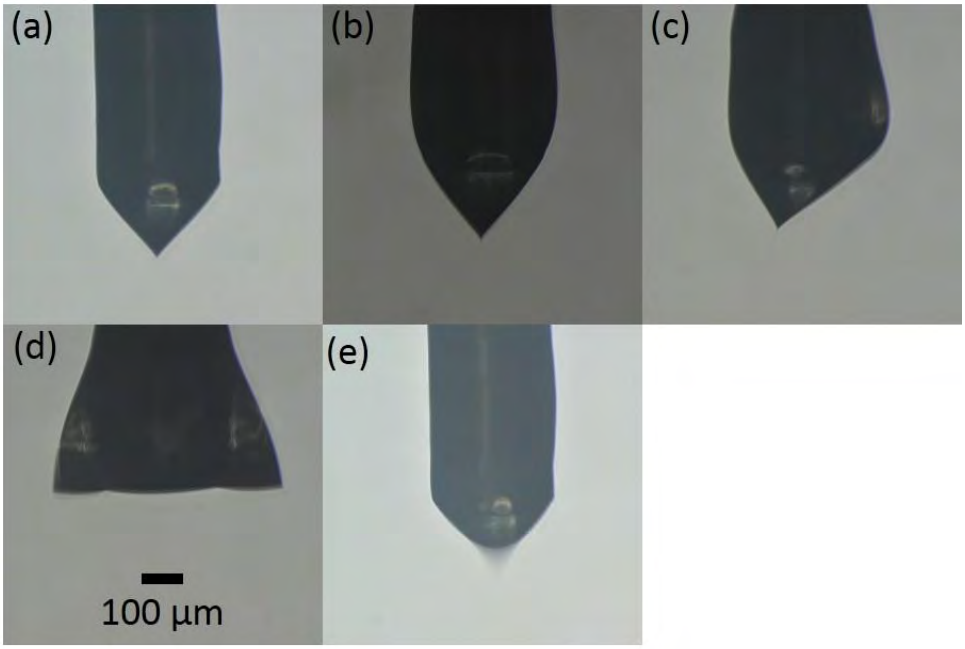

Fig. 3.2: Cycle of different spraying modes observed for $Ge_{23}Sb_7S_{70}$/propylamine solution

This was due to a strong tendency of the solution to wet up the nozzle. The depicted cycle begins with Fig 3.2(a), where a Taylor cone is observed. The solution will subsequently begin to wet the nozzle, shown in (b). When an appreciable volume of liquid is wetting the needle, the formation of two cone-jets occurs, shown in (c) and (d). This "double-cone" mode is not stable, and the solution drips after a few seconds, with very large droplets falling toward the substrate. These droplets are believed to be on the order of 100 μm in size, based on the resulting features on the film surface, shown in Figure 3.3. After the drop, there is minimal liquid at the bottom of the needle, and a pulsed cone is temporarily present before the new Taylor cone forms. The entire cycle can occur within as little as 20 s, but is often longer, and does not necessarily step through every mode in sequential order. For example, there might be oscillation between (b) and (c) for some time without the formation of (d). In these experiments, flow rates between 5 and 100 μL/hr were tested, with similar results obtained. Figure 3.3 shows a photograph and surface profile of an electrosprayed 0.05 g/mL $Ge_{23}Sb_7S_{70}$/propylamine measured with white-light interferometry.

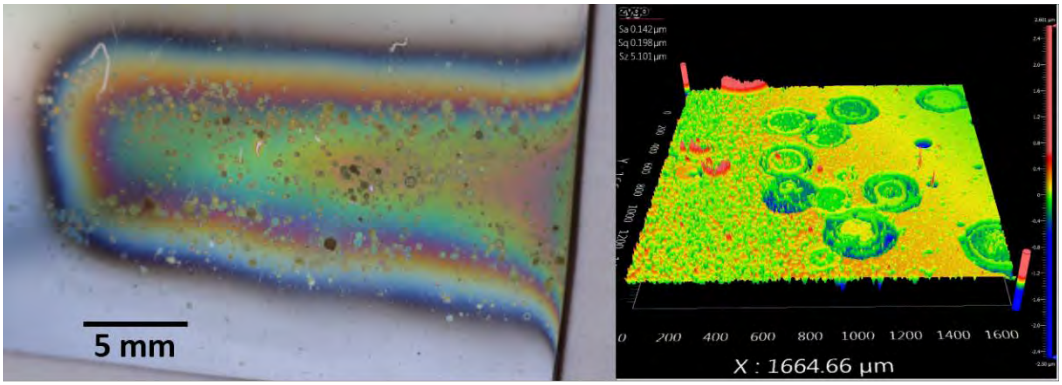

Fig. 3.3: Photograph (left) and white light interferometer image (right) of propylamine-derived $Ge_{23}Sb_7S_{70}$ film made by electrospray

The film is poor quality, with many large, round features on the film surface due to the large drops falling to the film from the nozzle during cone-jet instabilities. RMS surface roughness of the region characterized with white light interferometry is 198 nm.

Other solvents were explored as an alternative to propylamine, such as 0.2 g/mL As_2Se_3 dissolved in ethylenediamine, which was studied previously for the deposition of spin-coated films in [44]. In this case, stability of the cone-jet was better than with propylamine, but still not good enough to obtain smooth films. Generally, the As_2Se_3 cone-jet was somewhat stable, but periodically, a large amount of solution would discharge rapidly, instead of a spray of small droplets, shown in Figure 3.4.

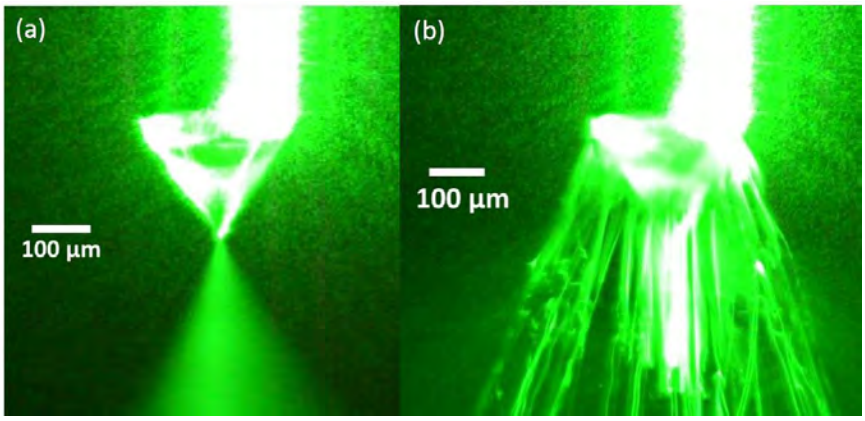

Fig. 3.4: Electrospray of As_2Se_3/EDA solution illuminated with a green laser sheet. (a) is a Taylor cone and spray, and (b) is a forceful drip of the solution.

The phenomenon in Fig. 3.4(b) is an expulsion of large droplets which disturb the surface of an otherwise smooth film that was formed by the spray in Fig. 3.4(a). This expulsion takes place over a short period of time, and occurred with a frequency of once every two seconds. Using normal backlighting, such as with a flashlight or ambient light, the cone-jet appears to simply "flicker," similar to the flickering of a candle flame. It was only upon

imaging the spray with a green laser sheet, and recording video of the spray that the expulsion could be observed. The photographs in Figure 3.4 are both single frames from a video taken at 30 frames per second. The expulsion was generally visible for one frame, or on the order of 30 ms.

While electrospray of As_2Se_3/EDA solutions were not stable in Taylor cone mode, they could be sprayed using a pulsed cone-jet mode. This mode is inherently unstable, as it is an oscillation between dripping and Taylor cone modes. The liquid still drips, but in this case these large droplets remained within a small area below the needle, instead of spreading throughout the area of the film like the unstable Taylor cones of $Ge_{23}Sb_7S_{70}$/propylamine and As_2Se_3/ethylenediamine. As a result, the small droplets formed from the Taylor cone were the only material to spread outwards, leading to smooth films in this region. This is shown in Figure 3.5.

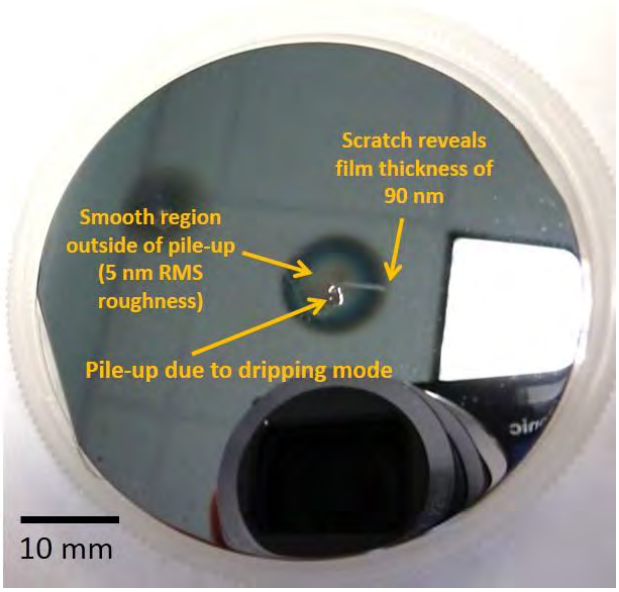

Fig. 3.5: Photograph of As_2Se_3 film made with pulsed cone-jet mode

These experiments demonstrated the possibility of making a ChG film from electrospray that has the potential to be useful in an optical application, due to the smooth surface with ~5 nm RMS roughness. However, the large "pile-up" of glass due to the dripping portion of the pulsed cone-jet mode poses issues, namely the problem of ensuring that the pile of glass does not affect the performance of the device, and also that a large portion of the material would be wasted in this unusable pile of glass. Therefore, achieving a stable Taylor cone is essential to the fabrication of optical ChG films using electrospray.

Through observing the electrospray of propylamine and ethylenediamine based solutions, it was determined that Taylor cone instabilities were a result of wetting of the solution on the nozzle. This causes oscillations in the size of the cone-jet, and variations in the effective flow rate. For example, when the solution is wetting up the needle, the effective flow rate of solution toward the substrate is low. Instead of reaching a steady-state amount of solution wet on the nozzle, the solution was observed to flow back down to the nozzle, causing an effective high flow rate of solution toward the substrate. The solution oscillates between wetting up and flowing down the needle, causing oscillations in the flow rate of the solution. There is an optimal range of applied voltage to obtain a stable cone-jet for a given solution, working distance, and flow rate, and the oscillations in flow rate are too great to be remain optimized for any given single value of applied voltage, leading to cone-jet instabilities. Wetting-induced cone-jet instability seems to be further complicated by the deposition of glass on the outer surface of the needle. This film could be re-dissolved, making the flow rate even less predictable as well as leading to variations in the glass concentration of the solution. In addition to the $Ge_{23}Sb_7S_{70}$/propylamine and

As_2Se_3/ethylenediamine solutions described above, other solutions tested included $Ge_{23}Sb_7S_{70}$ dissolved in butylamine, pentylamine, hexylamine, and ethanolamine. The most stable cone-jets were observed for $Ge_{23}Sb_7S_{70}$/ethanolamine solutions. It is believed that this is because of the relatively high viscosity of the solution, making it less prone to wetting up the nozzle. It is proposed that applying a hydrophobic coating, such as polytetrafluoroethylene (PTFE), a non-polar material with strong chemical resistance, would prevent the tendency of the polar amine-based solutions to wet the outer nozzle surface. In fact, better stability of ethanolamine-based solutions was observed by deliberately allowing the deposition of a glass film on the nozzle, which does not redissolve during electrospray. This film was deposited by pumping about 0.5 μL of the solution out of the syringe, allowing it to wet the nozzle in a thin layer, and then waiting for 1-2 hrs with the nozzle over the hotplate at 50-80°C while the solvent evaporated. While this worked well for the ethanolamine-based solutions, it could not be repeated for the propylamine- or ethylenediamine-based solutions, which quickly redissolved the coating. Therefore, it is suggested to explore the possibility of some insoluble, hydrophobic layer as an ideal remedy to prevent wetting of the nozzle.

In addition to a stable cone-jet, a critical degree of droplet drying is necessary to achieve high quality, smooth films. It is essential for the droplets to be wet upon arrival at the substrate, allowing the droplets to flow and become part of a film without optical interfaces, compared to dry deposition if the droplets dry too much on the way to the substrate. Solvent evaporates from the droplets as they travel toward the substrate, increasing the glass concentration and viscosity of the droplets. The degree of drying is

determined by the time of flight, initial droplet size, and the solvent properties, such as vapor pressure. Droplet drying times are estimated by Equation 3.1:

$$t_e = \frac{d_0^{\,2}}{K}, \qquad \text{(Eq. 3.1)}$$

where t_e is the evaporation time, d_0 is the initial droplet diameter, and K is the solvent evaporation rate, a solution property approximately proportional to the vapor pressure. Figure 3.6 below shows RMS roughness of films made with varying working distance. Substrate temperature was maintained at 55°C, flow rate at 10 µL/hr, and the duration of deposition was four minutes. This data is a demonstration of how the in-flight droplet drying affects surface roughness of the film, and shows a small dependence of surface roughness on working distance. The increase in roughness at longer working distances is explained by the longer flight duration of the droplets, allowing more time to dry. These samples were prepared by using a serpentine path of the spray over the substrate to achieve thickness uniformity, which is discussed in detail in Section 3.3. The thickness of a film deposited using this method is independent of the working distance.

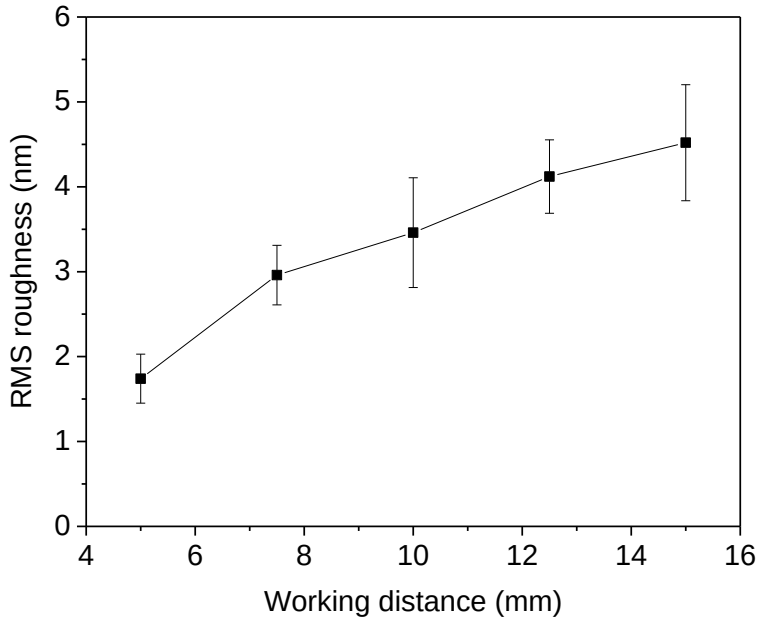

Fig. 3.6: RMS roughness of $Ge_{23}Sb_7S_{70}$ films made with varying working distance. Measurements taken in uniform thickness region of serpentine path. Films are all approximately 425 nm thick.

It was also observed that substrate temperature plays an important role in surface quality. Visual examples of the importance of optimal droplet drying are shown in the Figure 3.7, and RMS roughness is shown in Figure 3.8. The effect of substrate temperature will be discussed in more detail in Chapter IV.

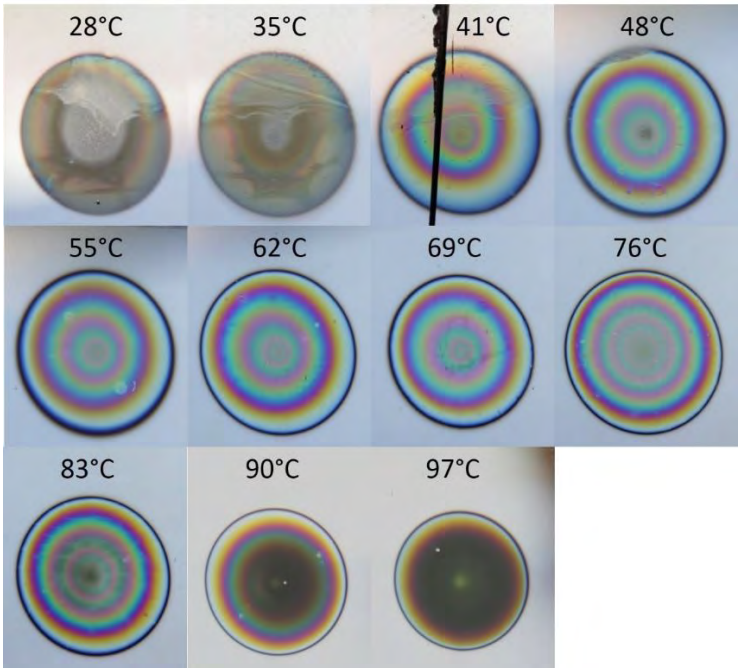

Fig. 3.7: 2 minute stationary depositions of $Ge_{23}Sb_7S_{70}$ films using 10 µL/hr flow rate, 5 mm working distance, and varying hotplate set-point temperatures. The dark line for the 41°C deposition is from a break in the substrate.

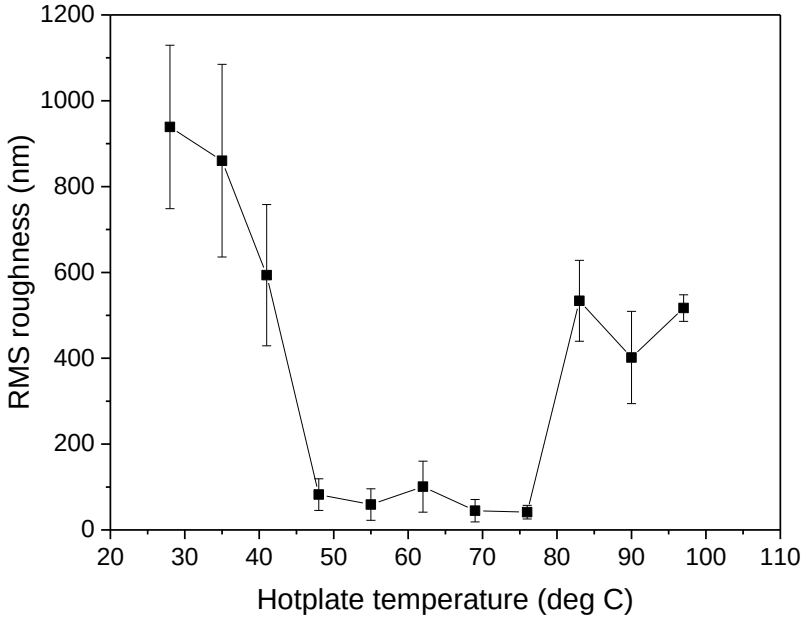

Fig. 3.8: RMS roughness of 2 min stationary depositions made with varying hotplate surface temperatures

By increasing the hotplate temperature, the rate at which solvent is driven off the film during deposition is increased. At temperatures below ~50°C, poor, non-uniform surface quality is observed, especially at the center of the films. This is evidenced by the low apparent reflectivity, which improves as temperature is increased. Substrate temperatures in the range of about 55-76°C are seen to result in generally smooth films, and temperatures above 83°C result in films with an increasingly matte surface appearance.

In summary, there are three key components to achieving optical quality films with electrospray:

- *Stability of spray*: the best stability observed was ChG/ethanolamine solutions, likely due to the higher viscosity
- *Degree of droplet drying during flight*: for smooth films with no optical interfaces, droplets must not be too dry upon arrival at the substrate, so that droplets flow and become part of the existing film.
- *Curing rate of the film*: good surface quality is observed for an optimal range of substrate temperatures, preventing the solution from puddling on the substrate as well as too-rapid removal of solvent.

3.2. Proof-of-concept: ethanolamine-based solutions

Based on these results, electrospray proof-of-concept was carried out in a fume hood (air atmosphere) using 0.05 g/mL $Ge_{23}Sb_7S_{70}$ dissolved in ethanolamine, recognizing that ChG materials are susceptible to oxidation, which can reduce infrared transparency. Because these materials are intended for use in planar photonic applications, there are

several important characteristics to meet: controlled, uniform thickness so that waveguides or other structures can be fabricated, and minimal optical loss, which is enabled by smooth surface and no absorptions in the operating range of the device. Typical thickness for most envisioned applications ranges from a few hundred nanometers to a few microns. Previously optimized $Ge_{23}Sb_7S_{70}$ films made by spin-coating were nominally 300 nm in thickness [43], so this was the target thickness of the electrosprayed films. It should first be noted that the tendency of electrosprayed ChG films to be circular in shape, and thicker at the center than the edges, as shown in the following photograph.

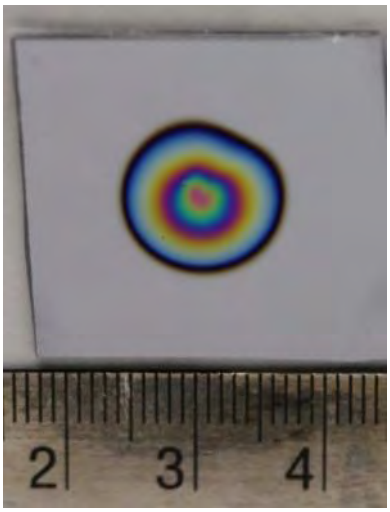

Fig. 3.9: Electrosprayed $Ge_{23}Sb_7S_{70}$/ethanolamine film made with a working distance of 15 mm on a Si substrate. Film is ~300 nm at the center. Scale is in cm.

Once it became possible to deposit films using electrospray, it was unknown how they compare to spin-coated films in terms of surface roughness, infrared transparency, and refractive index. These properties were measured and compared to spin-coated films made in parallel with the electrosprayed films. As described in the experimental section, electrosprayed films were deposited from a 0.05 g/mL $Ge_{23}Sb_7S_{70}$/ethanolamine solution

at a working distance of 15 mm, flow rate of 25 μL/hr, and duration of 8.5 min, while heating the substrate on a hotplate with surface temperature of 40°C. Spin-coated films were made from a 0.05 g/mL $Ge_{23}Sb_7S_{70}$/propylamine solution using a spin-speed of 3000 rpm for a duration of 10 s. Because ethanolamine has a lower vapor pressure than propylamine, it was unknown whether or not the solvent could be removed to a similar degree as propylamine. Films were subjected to the heat treatments described in Table 3.3, which were done under vacuum based on reference [43].

Table 3.3: Description of heat treatments used for electrosprayed and spin-coated $Ge_{23}Sb_7S_{70}$/ethanolamine films

Heat treatment number	Description
HT0	SC: 50°C for 5 min, ES: as-deposited
HT1	100°C for 1 hr
HT2	125°C for 1 hr
HT3	150°C for 1 hr
HT4	180°C for 1 hr
HT5	200°C for 1 hr

In Figure 3.10, film thickness is compared between electrosprayed films and spin-coated films throughout the heat treatments, with measurements taken at various distances from the electrosprayed film center point to illustrate the thickness profile that results from film deposition with no substrate translation. Theoretically, virtually any film thickness can be built up with electrospray by increasing the duration of deposition, like PVD methods. In contrast, the thickness of an individual spin-coated layer is ultimately limited by glass solubility, though multi-layer structures have been demonstrated to achieve greater than 10 μm thickness [97].

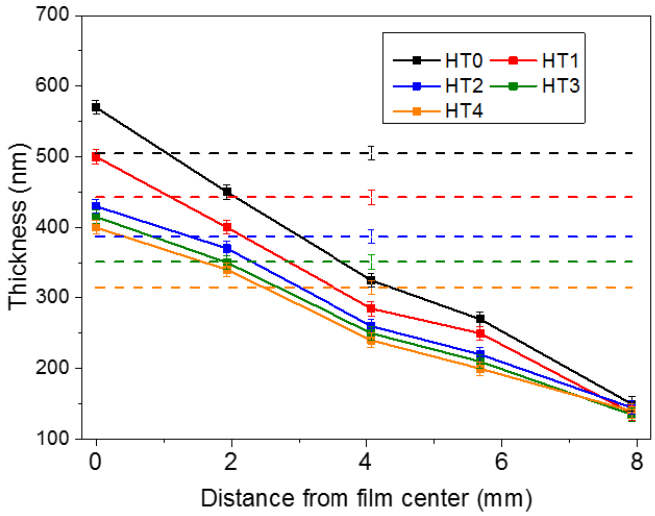

Fig. 3.10: Thickness comparison between spin-coated (dashed lines) and electrosprayed films (solid lines)

In addition to thickness, low optical loss is another important characteristic of optical thin films. Prior work by our team has shown a direct correlation between film roughness and scatter loss, whether in planar surfaces and on the side-walls of rib waveguides [7]. For the proposed QD-doped or GRIN film applications, good film surface quality is necessary to minimize scattering loss of the light, whether it is excitation and emission in the case of QD photoluminescence, or to maximize the sensitivity of a chemical sensing device by reducing the loss of a resonator. Removal of residual solvent from the film matrix is necessary to minimize absorption loss and quenching of luminescence [98]. RMS roughness and FTIR spectroscopy were used to demonstrate that electrospray is capable of producing films with comparable optical loss to spin-coating. RMS roughness values were taken after all heat treatments were completed. The average roughness of the electrosprayed films was found to be 6.8 nm with a standard deviation of 5.2 nm, and the spin-coated film was 7.8 nm with a standard deviation of 2.3 nm. While these RMS

roughness values are higher than TE films in other publications [99], they are similar to the initial studies on $Ge_{23}Sb_7S_{70}$ waveguides fabricated by TE and lift-off techniques [7]. FTIR spectra taken throughout the heat treatments were used to investigate solvent removal from the films, shown in Figure 3.11.

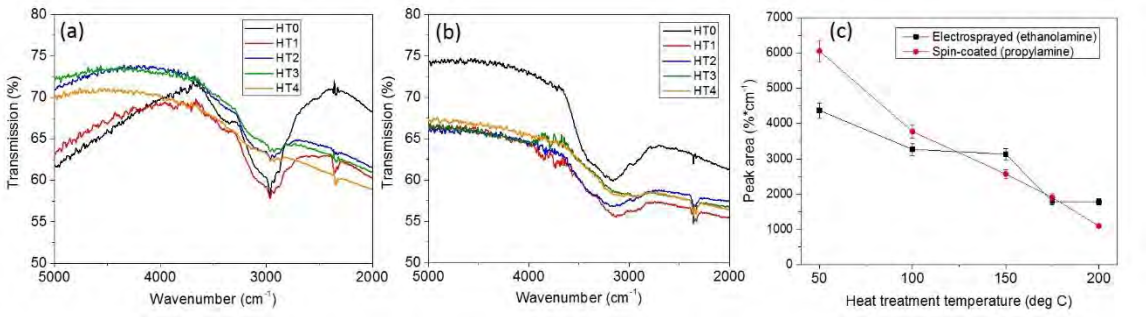

Fig. 3.11: FTIR spectra and solvent peak area evolution for spin-coated and electrosprayed films throughout annealing

From the FTIR spectra, both spin-coated and electrosprayed films demonstrate similar transparency in the mid-IR range, as the films were nominally the same thickness where the spectra were taken. The as-deposited (50˚C) electrosprayed film has a lower solvent absorption peak size at 3175 cm^{-1} than the as-deposited spin-coated film at 2960 cm^{-1}, implying that there is less solvent initially present in the film matrix, which is likely a result of the fast drying kinetics of electrospray droplets compared to the continuous liquid used for spin-coating. In both types of films, the solvent peak initially decreases rapidly at the lower heat treatment temperatures (50-150˚C). At this point, the remaining solvent is bonded more strongly into the film matrix, and it is driven off slower despite higher heat treatment temperatures. It should be noted that the shape of the FTIR transmission curve is partially determined by optical interference from the two layer, film plus substrate system. As the thickness decreases and refractive index increases when solvent is removed, an

increase in the period of the interference fringes is observed. As the heat treatments progress, propylamine is removed more quickly than ethanolamine, which is the result of the higher vapor pressure of PA. Despite the low vapor pressure of ethanolamine (0.054 kPa) relative to propylamine (33 kPa), the ethanolamine solvent can be removed to a similar degree as propylamine, as the spin-coated film had a slightly smaller absorption peak than the electrosprayed film after all heat treatments were completed, as shown in Figure 3.9. This residual solvent is the main disadvantage of solution-derived ChG film deposition, and it is possible that the intrinsic loss of microphotonic components made from solution-derived films is higher than with PVD methods.

Film refractive index is another important material property to the design of planar optical devices that employ doped or undoped films. A comparison of the refractive indices of spin-coated and electrosprayed films is shown in Figure 3.12, measured at 632.8 nm by taking reflection spectra with a Filmetrics F20 instrument.

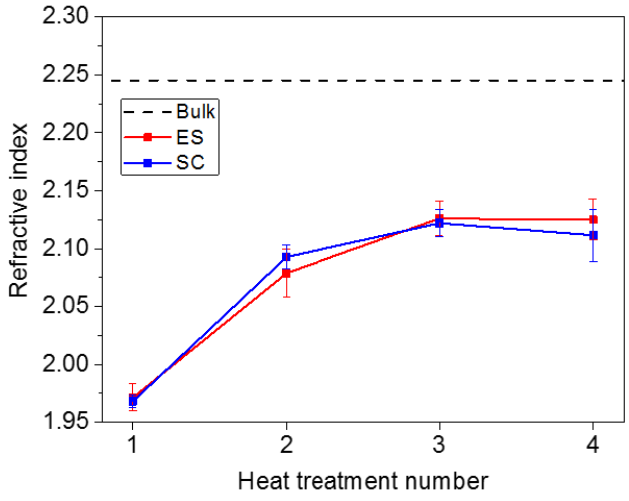

Fig. 3.12: Refractive index comparison between spin-coated and electrosprayed films throughout annealing

Throughout the heat treatments, refractive index was found to be in good agreement between the two types of films. Shown for reference is the refractive index of the bulk glass, which is the optimal, solvent-free target that we would like to realize. However, as is often the case with solution-derived films, the refractive index does not reach that of the corresponding bulk glass. This is consistent with the FTIR data, which shows the presence of residual solvent (n = 1.39 for propylamine and 1.45 for ethanolamine) that serves to lower the overall refractive index of the material. An estimation of the volume percent of residual solvent in the films after 4 h annealing is made by using the Lever Rule, where x is the volume percent of glass and the remaining volume is assumed to be solvent.

$$n_{measured} = (x)\left(n_{bulk\ glass}\right) + (1 - x)(n_{solvent}) \qquad \text{(Eq. 3.2)}$$

From Equation 3.2, the estimated volume of solvent remaining is approximately 15% for both the spin-coated and electrosprayed films. However, there are other factors which may contribute to the reduction in index of the films, such as the structure of the glass network, and porosity. It is proposed that the pure solvents and ChG solutions, having known pathlengths and amine solvent concentrations, could be tested with transmission measurements to estimate an attenuation coefficient of light at various wavelengths due to solvent. Transmission measurements of the films at the same wavelengths could then be utilized as an additional estimation of the amount of residual solvent. Although it is possible to fabricate thin ChG films with near complete removal of solvent, the remaining difference in refractive index between the solution-derived films and corresponding bulk glass is attributed to pores remaining in the film as solvent is removed and small amounts of residual solvent bonded into the film matrix [43]. The fact that the refractive index of

the electrosprayed film matches that of the spin-coated film implies that additional pores are not being formed between droplets during the electrosprayed film deposition. This further supports that the droplets have sufficiently low viscosity to flow upon arrival at the substrate.

Finally, it was also found that the films are adhered well to the substrate, and could not be removed with cellophane tape.

3.3. Optimization of thickness uniformity and solvent removal

As described in Section 3.2, initial explorations of film deposition by electrospray of $Ge_{23}Sb_7S_{70}$ were done using a flow rate of 25 μL/hr and 15 mm working distance. After these initial experiments, the typical flow rate was lowered to 10 μL/hr, as this allowed a more stable cone-jet, as well as leading to a smaller initial droplet size, which is an advantage for QD doping. Working distance was also decreased to 5 mm, as this allows thicker films to be deposited in a given amount of time compared to 15 mm working distance. With these process parameters, current of the $Ge_{23}Sb_7S_{70}$ electrospray was determined to be 0.3 μA. Table 3.4 below summarizes the conductivities of the solutions utilized for deposition in this chapter.

Table 3.4: Properties of electrosprayed liquids

Property	0.05 g/mL $Ge_{23}Sb_7S_{70}$ dissolved in ethanolamine	0.05 g/mL As_2S_3 dissolved in ethanolamine	Ethanolamine
Electrical conductivity (S/m)	2×10^{-2}	3×10^{-2}	5.5×10^{-5}

The results in Section 3.2 demonstrate that ChG films made with electrospray deposition have similar properties to spin-coated films. Therefore, it was deemed appropriate to continue studying this deposition method due to its potential advantages, namely near-100% material usage, the direct creation of geometries with 2-D or 3-D printing techniques, simple approach to graded refractive index films, and the potential for better nanoparticle dispersion. As As_2S_3 glass is also soluble in ethanolamine, this composition was studied for the initial demonstrations of GRIN coatings. The main reasons for this choice was because the refractive index of bulk As_2S_3 and $Ge_{23}Sb_7S_{70}$ are significantly different (2.40 and 2.25 at 633 nm, respectively), and compositional differences can be more easily mapped across the film due to unique elements in each glass.

The first step in these experiments was to obtain uniform thickness films using CNC control of the spray. Regions of uniform film thickness can be achieved by constant, relative velocity between the substrate and the spray. A demonstration of 1-D motion is shown in Figure 3.13.

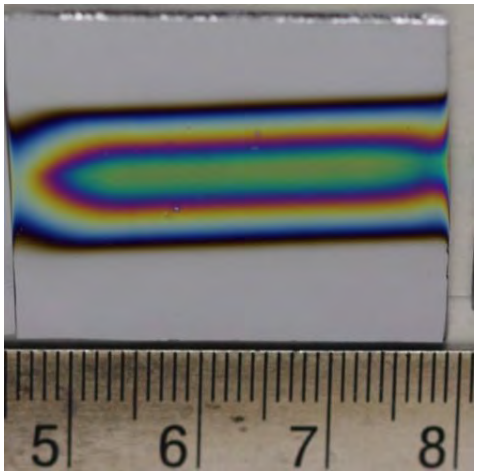

Fig. 3.13: Electrosprayed $Ge_{23}Sb_7S_{70}$ film deposited with one-dimensional movement of substrate. Scale is in cm.

The 1-D motion allows deposition of larger regions having similar thicknesses, which are generally indicated by similar color, due to optical interference, assuming that the refractive index is approximately constant over the film. The result of one-dimensional motion can be extended in two dimensions using a serpentine path with a small offset between passes. This method of obtaining uniform thickness films is shown in Figure 3.14.

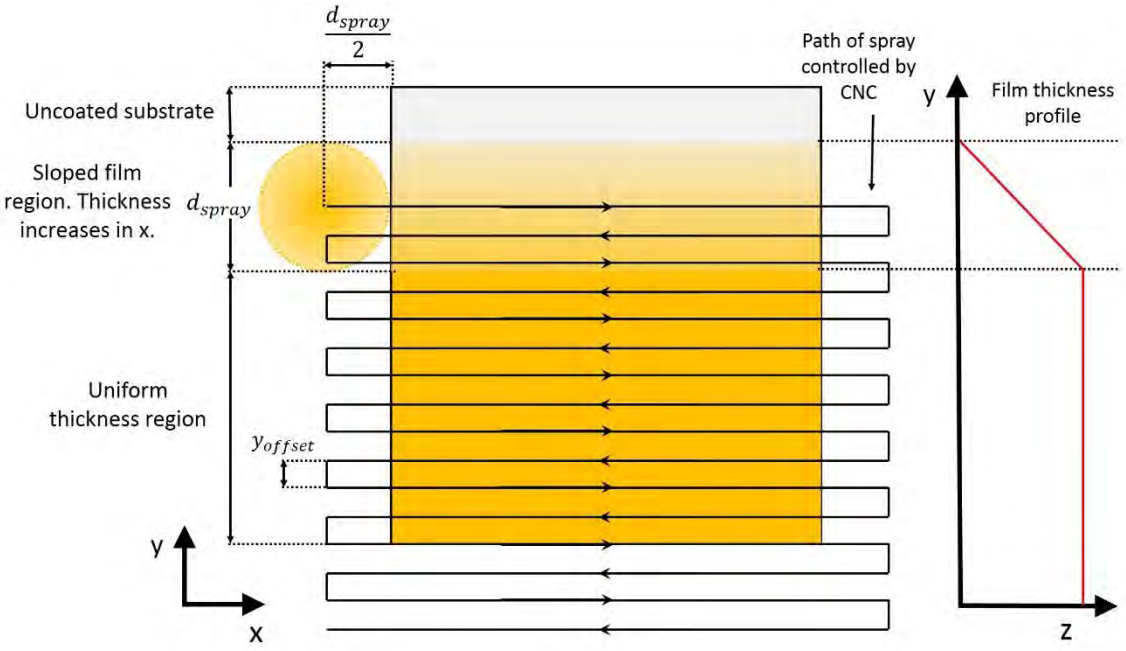

Fig. 3.14: Schematic of serpentine path motion of electrospray nozzle relative to substrate

By moving the spray over the substrate with small offsets (in the y-direction) between passes, the spray is moving approximately continuously in both directions. Initially, y_{offset} of 2 mm was tested, but this lead to films with a wavy surface profile, which is shown in the figure below.

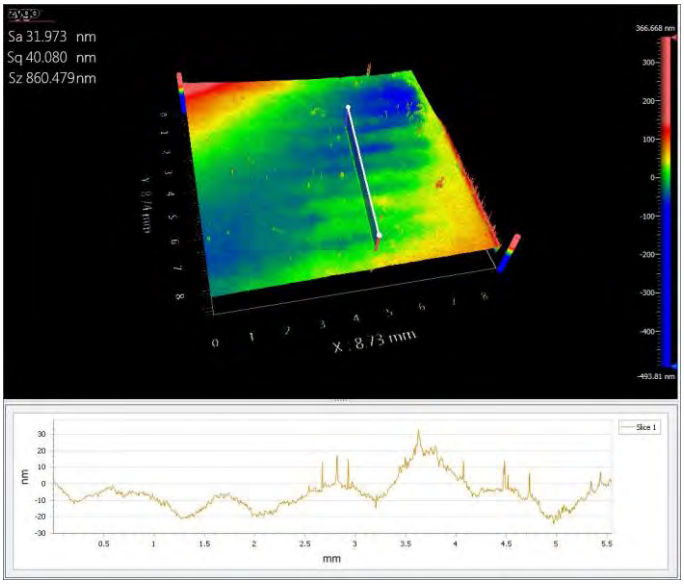

Fig. 3.15: White-light interferometer map of a film made with a serpentine path having y_{offset} = 2 mm, with a surface profile shown below taken from the location marked in the image

The period of the surface waves is approximately 1 mm. This discrepancy is unlikely to be a result of inaccuracy in the distance travelled by CNC, as it was calibrated and accuracy verified during set-up of the equipment. Rather, it is possible that there is an additional peak in the film thickness that forms between each pass. In order to reduce the waviness of the film surface and obtain better thickness uniformity, films were deposited using a y_{offset} of 0.5 mm. An annealing protocol was then established for solvent removal and densification of the film. The goals of these studies were to investigate the kinetics of solvent removal and the evolution of properties of both $Ge_{23}Sb_7S_{70}$ and As_2S_3 films made from ethanolamine-derived solutions in much more detail than the proof-of-concept studies in the previous section. Several considerations must be made when designing the steps of a heat treatment. Ideally, the properties and structure of the film would be identical to the

corresponding bulk glass, for easy prediction of the film properties. This means that no glass constituents are lost at high temperature, and that the film is fully densified, ensuring that the refractive index of the film is close to that of the bulk glass. Most importantly though, all residual organic solvent should be removed so that there are no infrared absorptions. For this heat treatment optimization, FTIR transmission spectra and thickness measurements were taken periodically throughout annealing at various temperatures. The area of the infrared absorption of ethanolamine was measured using the OMNIC FTIR software peak area function, and thickness measurements were compared to an estimation of theoretical film thickness, with the derivation based on conservation of mass.

It is assumed that the film is fully cured with the same density and composition as the corresponding bulk glass. In general, the thickness of the film is given by Equation 3.2, where T is the thickness, V/t is the rate of volume deposited per unit time, and A/t is the coverage area of the film deposited per unit time:

$$T = \frac{\left(\frac{V}{t}\right)}{\left(\frac{A}{t}\right)} \qquad \text{(Eq. 3.3)}$$

The volume of glass deposited per unit time is given by the following relationship, where C is the concentration of dissolved glass in the solution, Q is the flow rate of the solution, and ρ is the density of the bulk glass:

$$\frac{V}{t} = \frac{CQ}{\rho} \qquad \text{(Eq. 3.4)}$$

To determine deposition area per unit time, consider an area from the uniform thickness region, with the path of the spray depicted in Figure 3.15 below. An arbitrary number of

passes are made at velocity, V, to cover a distance Y_{cov} and X_{cov} in the y and x direction, respectively, and y_{offset} is the distance between passes.

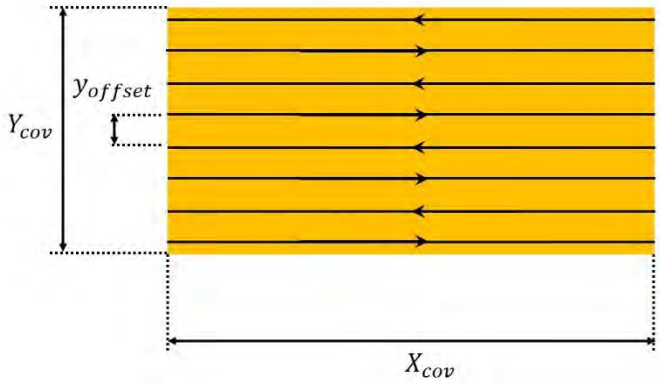

Fig. 3.16: Serpentine path schematic used in derivation of theoretical film thickness

The coverage area per unit time is then given by Equation 3.4, where t_{cov} is the length of time needed to coat a rectangular area with dimensions X_{cov} and Y_{cov}.

$$\frac{A}{t} = \frac{X_{cov}Y_{cov}}{t_{cov}} \qquad \text{(Eq. 3.5)}$$

The time, t_{cov}, is determined from the velocity of the pass and total distance covered, where N_p is the number of passes.

$$t_{cov} = \frac{X_{cov} * N_p}{V} = \frac{X_{cov}\frac{Y_{cov}}{y_{offset}}}{V} \qquad \text{(Eq. 3.6)}$$

The expression for t_{cov} can be substituted into Equation 3.4, giving an expression for the coverage area per unit time in terms of relevant deposition parameters.

$$\frac{A}{t} = y_{off}V \qquad \text{(Eq. 3.7)}$$

Finally, substituting Equations 3.4 and 3.7 into Equation 3.3 results in the theoretical film thickness:

$$T = \frac{QC}{\rho y_{off} V} \qquad \text{(Eq. 3.8)}$$

This estimation of film thickness was used in the following optimization of the annealing conditions and to obtain desired film thicknesses.

In order to optimize the annealing conditions, thickness and residual solvent were tracked throughout a set of heat treatments. The degree of solvent removal is characterized by the change in area of the absorption peaks seen in FTIR transmission measurements, which is demonstrated in Figure 3.17.

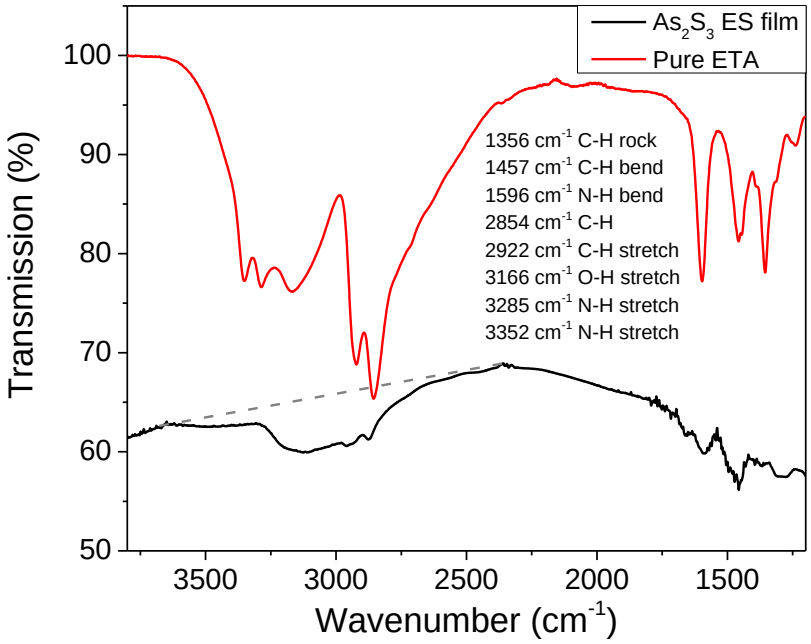

Fig. 3.17: Comparison of FTIR spectra of pure ethanolamine solvent and ethanolamine-derived As_2S_3 film made by electrospray (sample is Fig. 3.17 – 8 hrs – N_2 atmosphere), showing how residual solvent peak area is determined by drawing a baseline and measuring the area.

In the OMNIC FTIR software, a baseline was drawn by eye, and the peak area fitting function was used to compare the relative amounts of solvent remaining in the films. This

was plotted for a series of anneals, shown in Figures 3.18 and 3.19. By adjusting the baseline, the maximum variation for measured peak sizes was found to be about 10% for spectra taken throughout the heat treatments. Therefore, the error was taken to be +/- 5% on the peak size. In a similar way to [43], the goal was to use a stepwise annealing procedure, as this tends to result in films with better surface quality. At a given annealing temperature, it is observed that the solvent removal rate is initially high, then slows down. Once the removal rate slows, a higher temperature heat treatment is used, until no more solvent can be removed. The processing parameters of both films were 10 µL/hr flow rate, 10 mm working distance, and serpentine paths with 0.5 mm offset and 20 mm/min velocity of the nozzle over the substrate.

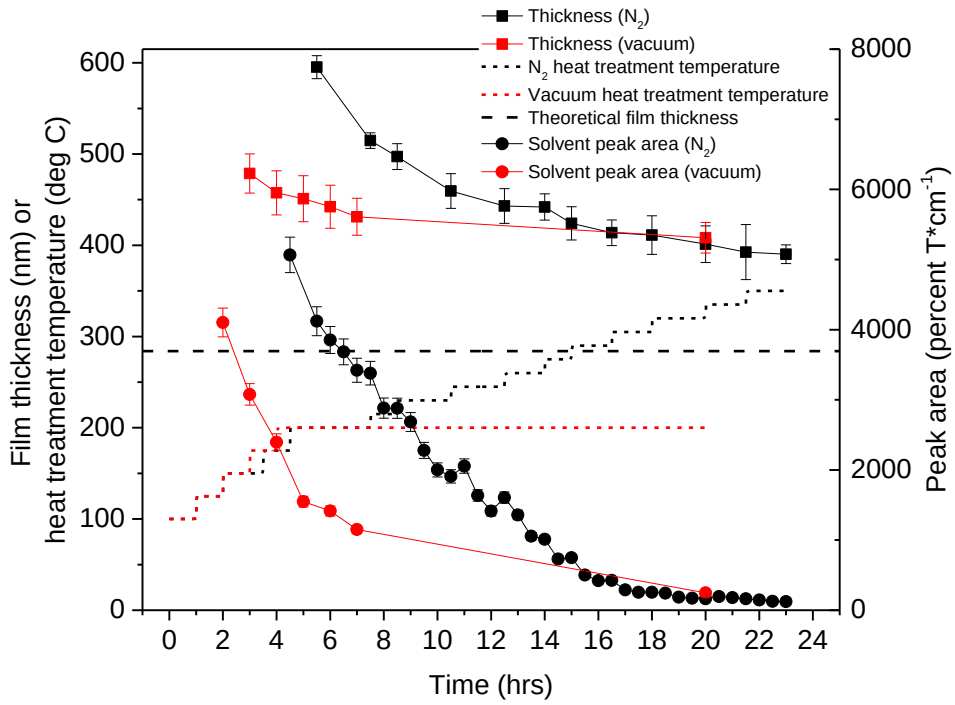

Fig. 3.18: Annealing optimization of electrosprayed $Ge_{23}Sb_7S_{70}$. The left vertical axis represents either the thickness of the film (red and black square data points), or the temperature profile of the heat treatments (red and black dashed lines). Theoretical thickness for this film is 284 nm.

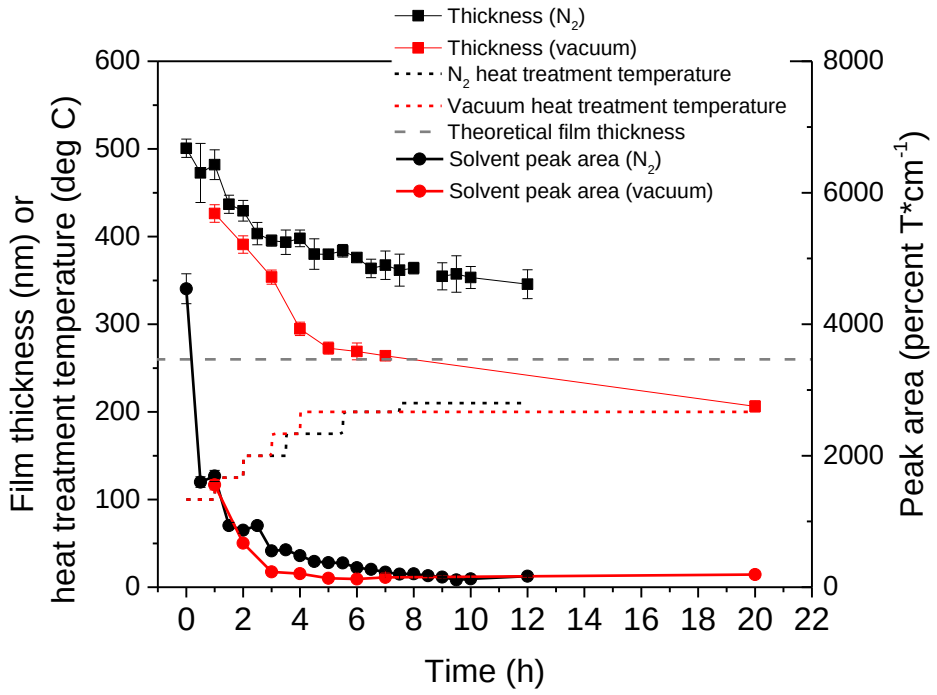

Fig. 3.19: Annealing optimization of electrosprayed As_2S_3. The left vertical axis represents either the thickness of the film (red and black square data points), or the temperature profile of the heat treatments (red and black dashed lines). Theoretical thickness for this film is 260 nm.

In Figures 3.18 and 3.19, film thickness is also tracked, as characterized by a contact profilometer. The temperature profiles of the anneals are indicated by the dotted lines. There are a few notable conclusions from this study. First, as indicated by the error bars on the thickness measurements, which were taken over an area of 1 cm^2, it is found that the serpentine method with y_{offset}=0.5 mm results in films with good thickness uniformity.

Next, solvent removal from the $Ge_{23}Sb_7S_{70}$ film is slower than from the As_2S_3 film, and requires higher temperatures in the case of annealing under nitrogen indicating that solvent is bound stronger to the $Ge_{23}Sb_7S_{70}$. This is consistent with literature on the

dissolution of ChG in amines, which has shown that $Ge_{23}Sb_7S_{70}$ forms molecular units in solution, compared to As_2S_3, which tends to form relatively large particles on the order of 1 nm [82]. It is also interesting to note that As_2S_3 tends to approach theoretical thickness under vacuum annealing, while $Ge_{23}Sb_7S_{70}$ is significantly thicker than theoretical. However, prolonged annealing of As_2S_3 results in a film which is thinner than theoretical. It is likely that there are issues with volatilization of the As_2S_3 film at 200°C annealing under vacuum, but as indicated in Table 3.5, the composition of the As_2S_3 film remains stoichiometric throughout all anneals, as characterized by EDX.

Table 3.5: Composition of vacuum annealed As_2S_3 film measured with EDX

Vacuum anneal	at% As (+/-2%)	at% S (+/-2%)
Bulk glass	40	60
1 hr @ 100°C	39	61
1 hr @ 125°C	38	62
1 hr @ 150°C	38	62
1 hr @ 175°C	40	60
1 hr @ 200°C	40	60
2 hrs @ 200°C	39	61
13 hrs @ 200°C	40	60

Table 3.6: Composition of vacuum annealed $Ge_{23}Sb_7S_{70}$ film measured with EDX

Vacuum anneal	at% Ge (+/-2%)	at %Sb (+/- 2%)	at% S (+/-2%)
Bulk glass	21	8	72
1 hr @ 150°C	32	11	57
2 hrs @ 200°C	28	9	63
13 hrs @ 200°C	28	9	63

There is some loss of sulfur when comparing the composition of an electrosprayed $Ge_{23}Sb_7S_{70}$ film to the corresponding bulk glass. The most likely explanation is that there

are some sulfur rich precipitates that form when dissolving the bulk glass in ethanolamine, which are either filtered out or do not make it into the film during the deposition. It seems that there is also some loss of germanium and antimony between the 1 hr @ 150°C anneal, and the 2 hrs @ 200°C anneal, which brings the composition closer to the original stoichiometry of the bulk glass.

Solvent removal, thickness, surface roughness and composition are also extremely important when designing a GRIN coating. Surface roughness was characterized throughout vacuum annealing of the films of each composition, shown in Figure 3.20. Predictable composition is important in order to obtain the desired optical properties, such as refractive index.

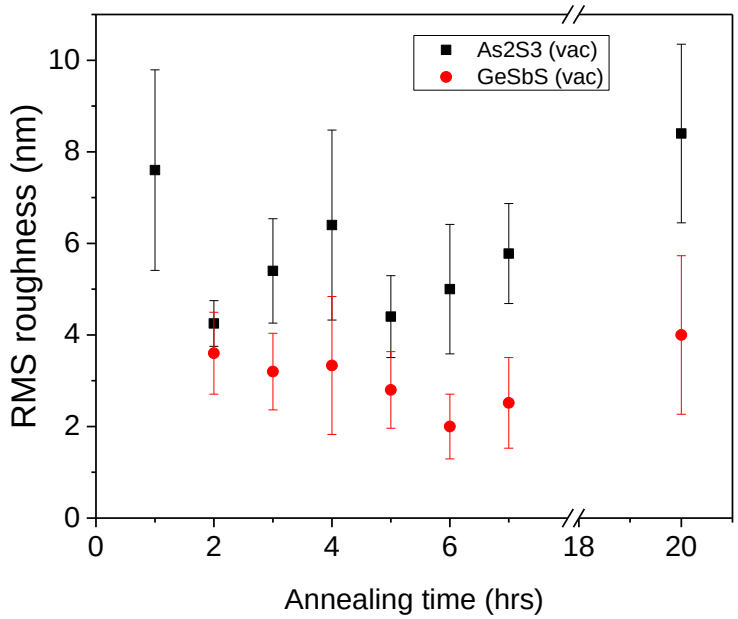

Fig. 3.20: Surface roughness of electrosprayed As_2S_3 and $Ge_{23}Sb_7S_{70}$ throughout series of vacuum anneals. The temperature profile of the anneals is the same as shown in the solvent removal and thickness graph

These roughness data points are taken from averages of five measurements taken randomly across an area of 1 cm^2. The size of the error bars are +/- one standard deviation. From this data, it is demonstrated that electrosprayed ChG films have low roughness across an area that is similar in size to proposed microphotonic devices. The surface roughness remains fairly constant throughout the annealing conditions, and is below 10 nm, which is acceptable for proof-of-concept films intended for devices. However, it should be noted that the overall purpose of these experiments was to optimize the annealing conditions of ethanolamine-derived, electrosprayed films, and roughness was not optimized for this study. It is interesting to note that $Ge_{23}Sb_7S_{70}$ has consistently lower roughness than As_2S_3. This is believed to be an effect of the quicker removal of solvent from As_2S_3 than $Ge_{23}Sb_7S_{70}$, leading to dryer deposition of As_2S_3 droplets. As demonstrated previously, there is an optimal amount of drying of the droplets before arriving at the substrate in order to achieve smooth films, which is dictated by the working distance and initial droplet size. It is likely that the deposition conditions used for As_2S_3 were further from optimal than $Ge_{23}Sb_7S_{70}$, due to the difference in solvent removal kinetics for the two solutions.

Refractive index was characterized throughout the vacuum anneals at 633 nm, shown in Figure 3.21.

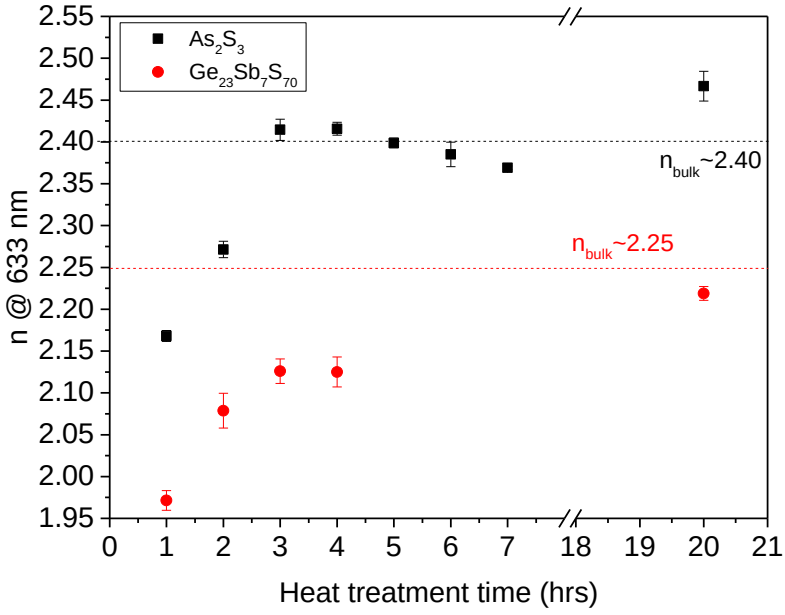

Fig. 3.21: Refractive index of electrosprayed films measured with Filmetrics F20 at 633 nm

In this figure, comparison is shown between both electrosprayed film compositions, as well as the corresponding bulk glasses. Electrosprayed As_2S_3 approaches the index of the bulk glass after 3 hours of annealing and a maximum temperature of 150°C, and $Ge_{23}Sb_7S_{70}$ is significantly below the index of the corresponding bulk glass, until prolonged annealing at 200°C. These results are consistent with previous literatures studies on spin-coated films of both compositions [43,84,100]. One possible reason for the reduced refractive index and higher than theoretical thickness of $Ge_{23}Sb_7S_{70}$ is the structure of the films. It has been shown in previous studies that the structure of solution-derived $Ge_{23}Sb_7S_{70}$ films is different from the bulk glass [83]. Porosity can also cause reduced refractive index and lower density/increased thickness, but no porosity was observed. The micrograph below is cross-sectional TEM of a three layer, QD-doped sample, where the intention was to

investigate the dispersion of three different concentrations of QDs in the film. However, this micrograph is presented here to illustrate a lack of porosity in the films, and the assumption is made that the presence of QDs does not affect the porosity.

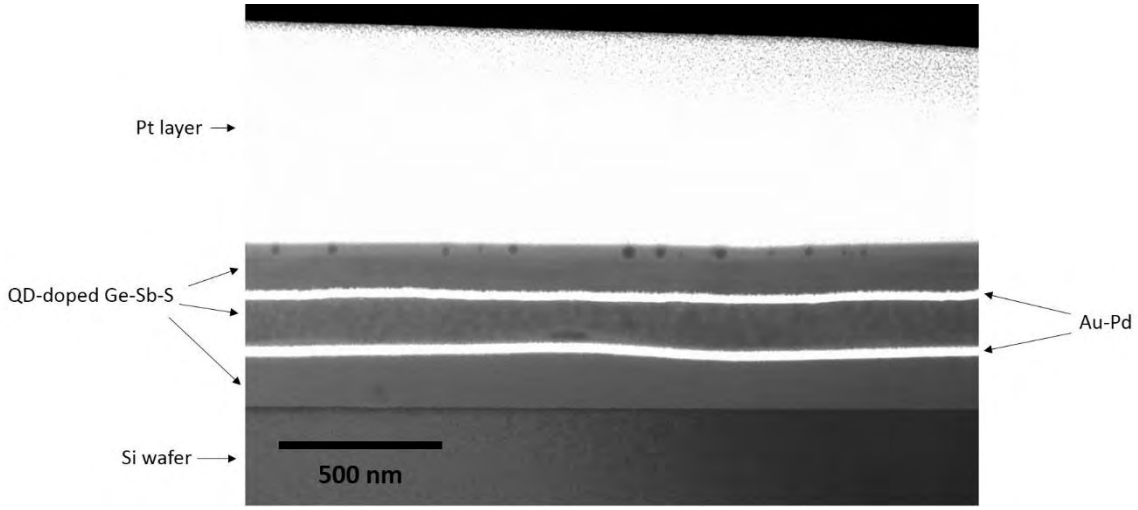

Fig. 3.22: Cross-section STEM of three layer, QD-doped $Ge_{23}Sb_7S_{70}$

This sample was fabricated by electrospraying three films of $Ge_{23}Sb_7S_{70}$ using a serpentine path to obtain uniform thickness. Between the layers of glass, Au-Pd layers were sputter-coated to prevent interaction during deposition of the next glass layer. A cross-section of this sample was then lifted out using a focused ion beam (FIB) instrument, during which a layer of Pt was deposited on the top surface of the sample. The top of the sample shows the presence of pores, which is believed to be caused by interaction of the Pt-layer with the top layer of ChG. Since this is the only location that shows any porosity, it is concluded that the electrosprayed $Ge_{23}Sb_7S_{70}$ films generally do not exhibit porosity, and that the reduced refractive index of the films is not from pores. However, if pores were present, a lever rule could be utilized to estimate the percentage of pores based on the following equation, where P is the volume fraction of pores, n_{total} is the refractive index of the total

film, n_{glass} is the refractive index of the glass phase, and n_{air} is the refractive index of the pores (assumed to be air-filled).

$$P = \frac{n_{total} - n_{glass}}{n_{air} - n_{glass}} \qquad \text{(Eq. 3.9)}$$

3.4. Gradient refractive index films

Gradient refractive index (GRIN) coatings have potential applications in planar sensing devices. One purpose of such a coating would be to vary the effective refractive index of an array of resonators through the interaction of the evanescent portion of the wave with the e-GRIN layer. In varying the effective index, the resonant wavelength of each resonator would be slightly different. The current approach to attaining a range of resonators with varying resonant wavelengths is to vary their pathlength, according to Equation 3.9, where r is the radius, n_{eff} is the effective index of the waveguiding material, m is the mode number, and λ_m is the resonant wavelength

$$2\pi r n_{eff} = m\lambda_m \qquad \text{(Eq. 3.10)}$$

As described in Equation 3.9, λ_m can be varied by changing n_{eff}. Therefore, a GRIN coating shown in Figure 3.23 is a method that could allow a range of resonant wavelengths without the spatial constraints or processing complexity of many different sized resonators.

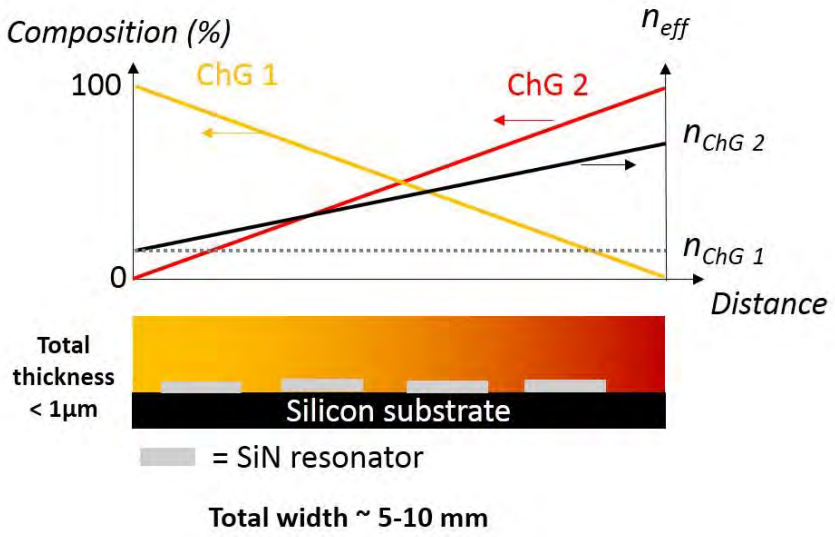

Fig. 3.23: Schematic representation composition of a true-GRIN resonator array coating (not to scale)

However, it is not necessary to have a true GRIN film for this application, as an effective GRIN (e-GRIN) coating can be fabricated by multiple layers of material with different compositions. Figure 3.24 shows a simple, two layer e-GRIN film design utilizing two linearly sloped films of different composition.

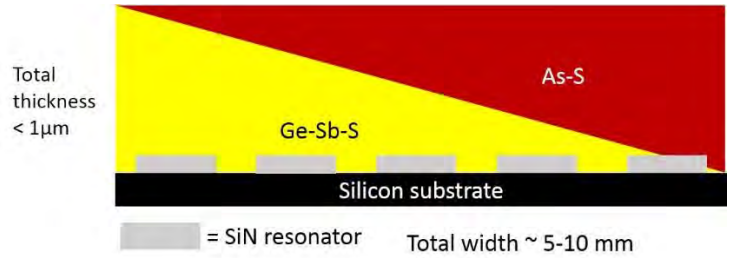

Fig. 3.24: Cross-section of two layer e-GRIN film (not to scale)

Such a film can be created using simple processing by electrospray and CNC patterning with three different methods, described in Figure 3.25.

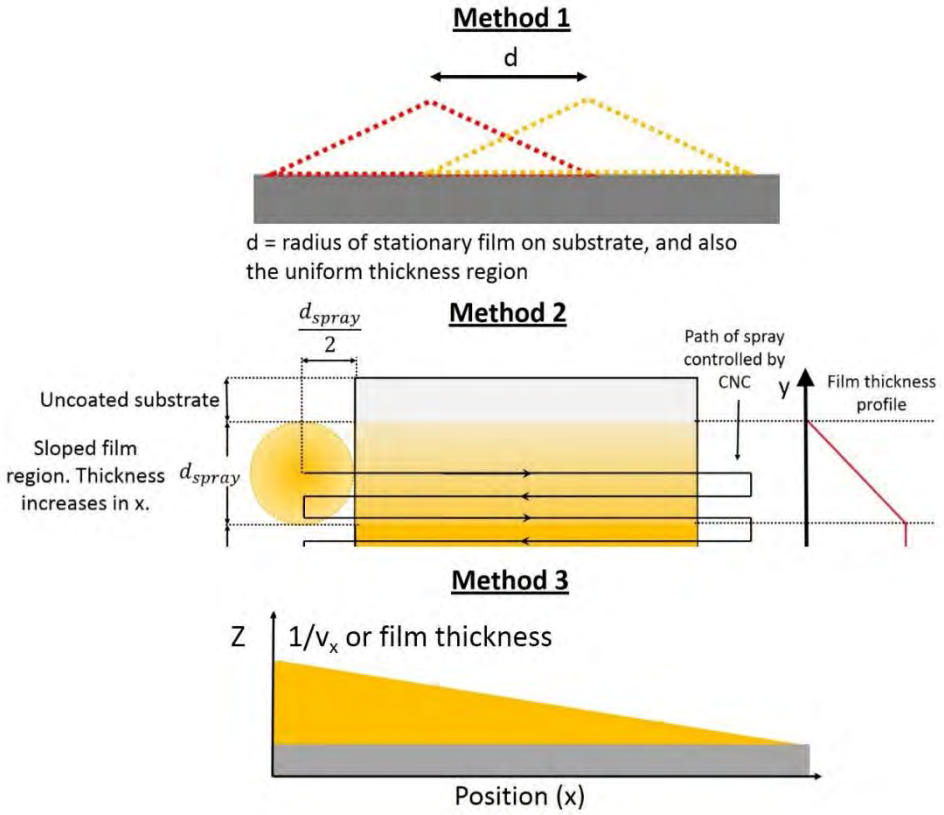

Fig. 3.25: Different methods of obtaining sloped films for the fabrication of effective-GRIN coatings

Method 1 consists of making 1-D passes of the spray over the substrate. Method 2 uses the first portion of the serpentine path described in section 1.3, where the film thickness is increasing. It should be noted that both Method 1 and 2 inherently have "overspray" material which is not used. Method 3 uses a constantly changing velocity of the spray over the substrate to obtain a variation in thickness. This is coupled with a serpentine path moving with offsets in the Y direction to allow coverage over the XY plane. Method 3 is regarded as the most flexible, as the coverage area or film slope using Method 1 and Method 2 is dictated by the working distance between the spray and substrate. With Methods 1 and 2, the working distance needed for a certain coverage area may not be

optimal for the other film properties, such as surface roughness. In contrast, Method 3 allows much more control over the thickness profile and coverage area of the film, with the use of an optimal working distance. However, it is not currently possible to use Method 3 with our system, as velocity cannot be changed continuously, so we have focused on Methods 1 and 2.

Method 1 was found to result in films which are very linear in thickness profile, whereas Method 2 films are nonlinear. A sample Method 2 film profile is shown in Figure 3.26.

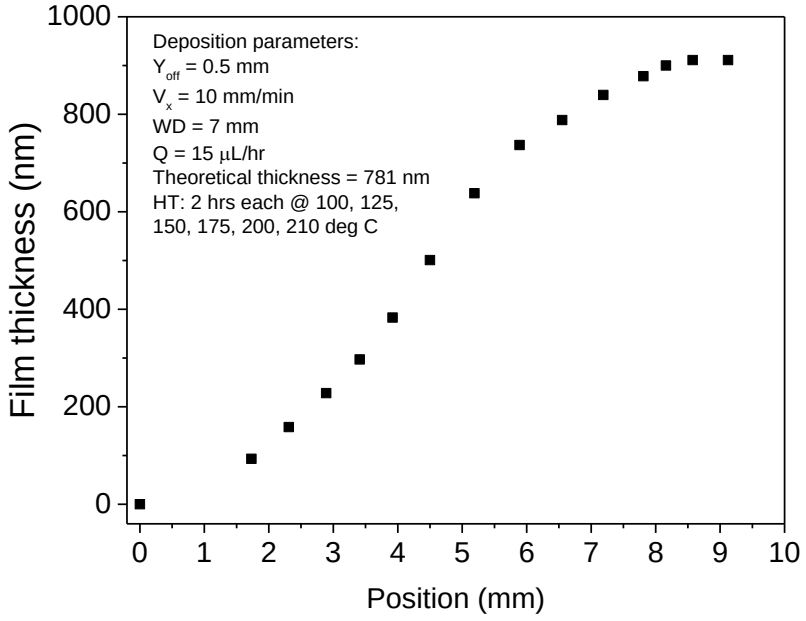

Fig. 3.26: Method 2 film profile of electrosprayed ChG solution determined by making scratches in the film and measuring with a contact profilometer

Therefore, initial e-GRIN demonstration consists of using Method 1 films. With this technique, coverage area can be tuned by varying the working distance between the nozzle

and substrate, and film thickness can be tuned by varying the velocity of the nozzle relative to the substrate. Data from this optimization is shown in Figures 3.27 and 3.28.

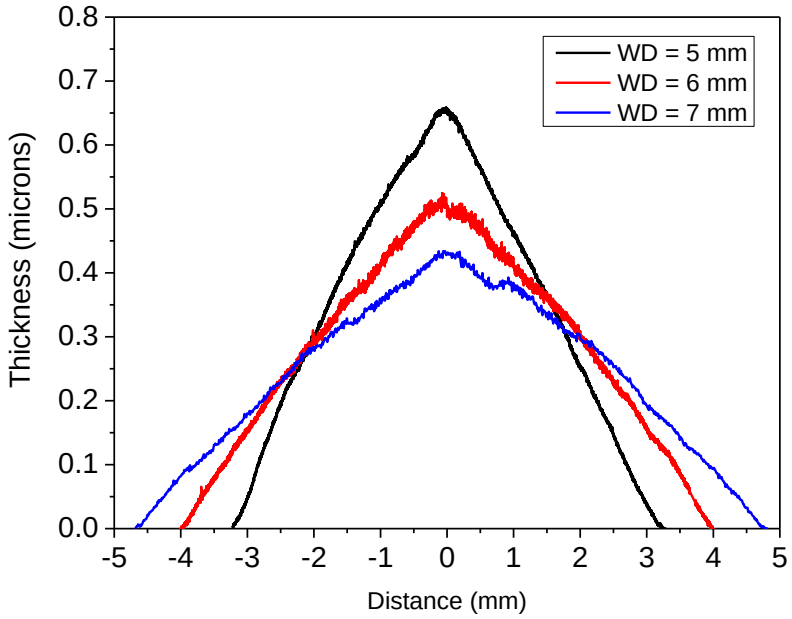

Fig. 3.27: 1-D passes of $Ge_{23}Sb_7S_{70}$ at a flow rate of 10 µL/hr and velocity of 2 mm/min

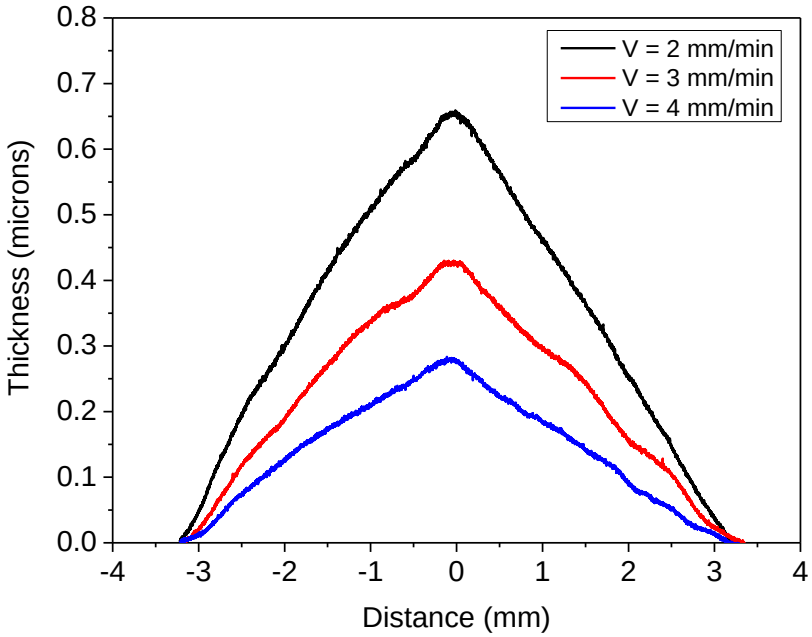

Fig. 3.28: 1-D passes of $Ge_{23}Sb_7S_{70}$ at a flow rate of 10 µL/hr and working distance of 5 mm

When using Method 1, only half of each film is usable as a component of the e-GRIN. The expected profile of such a film is depicted schematically in Figure 3.29, including the wasted "overspray" regions.

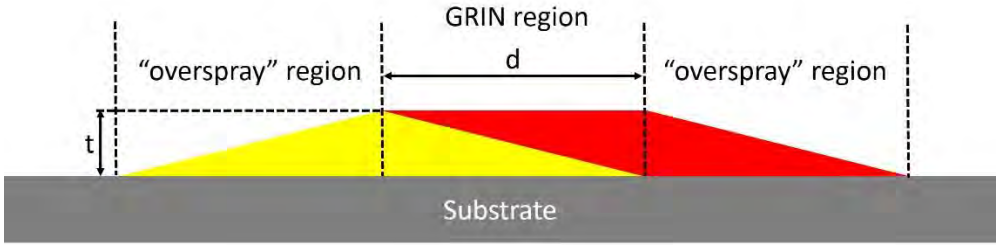

Fig. 3.29: Expected profile of e-GRIN from Method 1. Yellow and red represent different compositions of ChG

For the e-GRIN demonstration, the target "d" was 3 mm, and the target "t" was less than 500 nm. First, a single pass of As_2S_3 was deposited at a velocity of 5 mm/min and working distance of 4.5 mm. This resulted in poor film quality, evidenced by Figure 3.30.

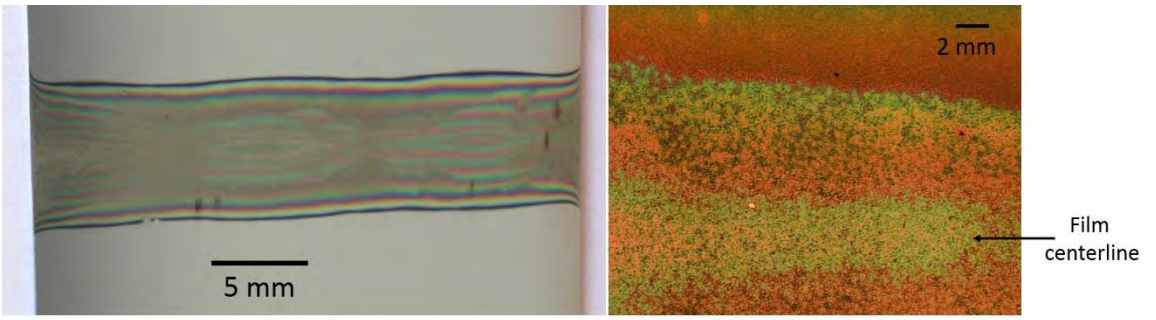

Fig. 3.30: Photograph (left) and optical micrograph (right) of single pass As_2S_3 film

This poor film quality is a result of too much material being deposited per unit time per unit area of the substrate. Film quality is vastly improved by making multiple passes at 20 mm/min to deposit a film of similar thickness, which in this case is 400 nm at the center. The improved surface quality of the multi-pass film is shown in Figure 3.31.

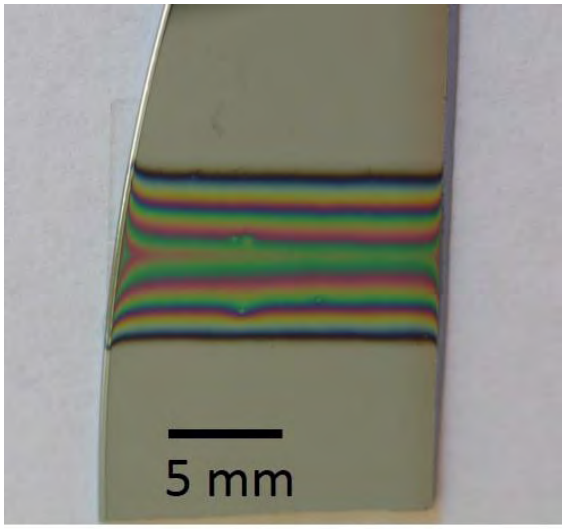

Fig. 3.31: Multi-pass As_2S_3 film made with 8 passes at 20 mm/min

During the depositions, the substrate is heated, which serves to begin curing the film as it is deposited. By using several passes to stack up thin layers, each layer has some time to cure before the next layer is deposited. This results in the as-deposited film having a lower concentration of residual solvent than a single-pass film of similar thickness, which in this case is ~400 nm for both the single pass and multi-pass films. Upon driving off the greater amounts of residual solvent in the single-pass film, greater dimensional changes occur, and more solvent escapes through the surface of the film, leading to the rough surface in Figure 3.26. There is a distinct difference in the surface morphology at the center of the single-pass film (center of image) compared to the edge of the film (top of image). As the edges

of the film are thinner, and formed from smaller, dryer droplets, the surface quality appears smoother than the center. Figure 3.32 below shows the surface profiles for As_2S_3 films made with multiple 1-D passes at a 5 mm working distance.

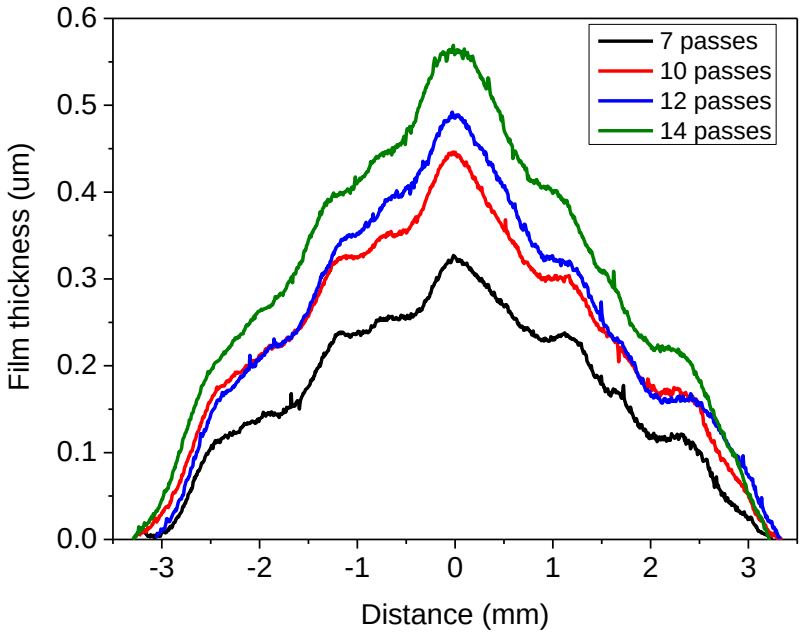

Fig. 3.32: Thickness profiles of As_2S_3 films made with varying numbers of 1-D passes

Very similar coverage area is observed for both As_2S_3 and $Ge_{23}Sb_7S_{70}$ films made with passes at a 5 mm working distance. It is interesting that the As_2S_3 film profiles in Figure are "wavy" and not linear like observed for $Ge_{23}Sb_7S_{70}$. It is possible that the wavy profile is more representative of the spatial flow rate of the spray, and that the linear film profiles form due to a post-deposition smoothing effect, although this was not investigated further. It is also possible that the surface of the substrate exhibits waviness on the surface, contributing to the thickness variations recorded by the profilometer. In data presented later

in this section, As_2S_3 films are shown with a smooth, linear change in thickness profile, so the waviness observed in Figure 3.32 is not always present.

White-light interferometry was utilized to analyze and optimize the surface quality of the films made with 1-D motion of the spray. A grid of surface analyses was made with 500 µm spacing between each measurement. Each measurement analyzed an area of 415 µm x 415 µm, and scans were made across the entire film (i.e. perpendicular to the direction of the spray motion) for a distance of about 5 mm along the film (i.e. parallel to the direction of the spray motion). A three-dimensional plot of the RMS surface roughness of an electrosprayed $Ge_{23}Sb_7S_{70}$ film is shown below.

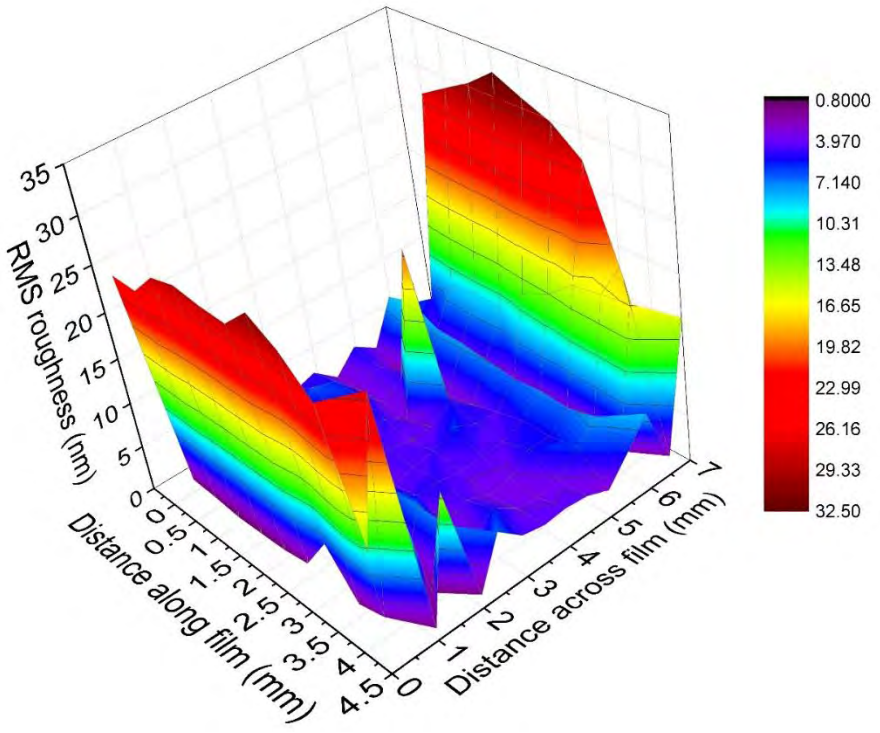

Fig. 3.33: RMS roughness mapping across surface of $Ge_{23}Sb_7S_{70}$ film made with 8 passes at 24 mm/min, 5 mm working distance, and 10 µL/hr flow rate.

There is a roughness spike in the center region of the film at the position: 1 mm along, 5 mm across. This center located roughness is generally uncharacteristic for such films made with 1-D motion, which is supported by the small error bars on roughness mapping of similar films in the center region that are shown in the following figures. It is believed that this localized roughness is due to random instabilities in the spray that cause large droplets to be expelled at the substrate. It is also possible that dust particles or other contamination that were present on the substrate before deposition, or were introduced to the film surface during or after processing. SEM was also utilized to investigate the surface of the $Ge_{23}Sb_7S_{70}$ films.

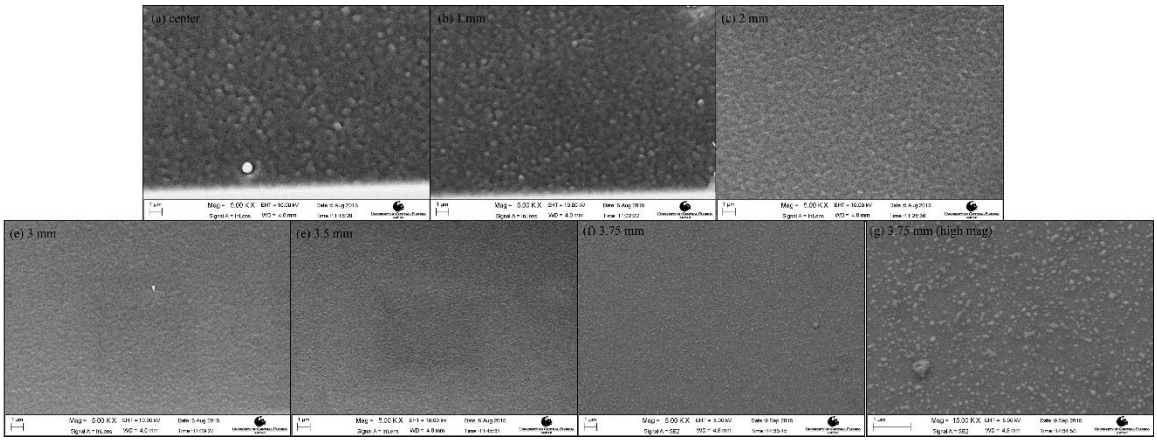

Fig. 3.34: SEM of $Ge_{23}Sb_7S_{70}$ film, at varying distances from the center, which was made with 8 passes at 24 mm/min, 5 mm working distance, and 10 µL/hr flow rate. These images were taken with the stage tilted at 30 degrees.

The purpose of these SEM images was to investigate the reason that the films tend to be rougher at the edges. In the SEM images, the surface morphology changes across the film. There are larger features at the center, which decrease in size toward the edge of the film. Finally, at approximately 3.75 mm from the center, there is incomplete coverage of the film on the substrate, as evidenced by micrographs (f) and (g). In addition to the incomplete

coverage that is observed, it is known that too-dry deposition and non-optimal substrate temperatures can both lead to increased surface roughness. For the case of too-dry deposition, this could be caused by a distribution in the droplet sizes. The smaller, lighter, and more mobile droplets likely travel further from the center of the spray than the larger and heavier droplets. From Equation 3.10, where t_e is the evaporation time, d_0 is the initial droplet size, and K is the solvent evaporation rate, smaller droplets have shorter evaporation times.

$$t_e = \frac{{d_0}^2}{K} \qquad \text{(Eq. 3.11)}$$

It is therefore possible that the edge roughness can come from dry deposition of small, mobile droplets present in the expanding spray. As a further investigation, imaging of a short deposition on a Si wafer was done using SEM, shown below.

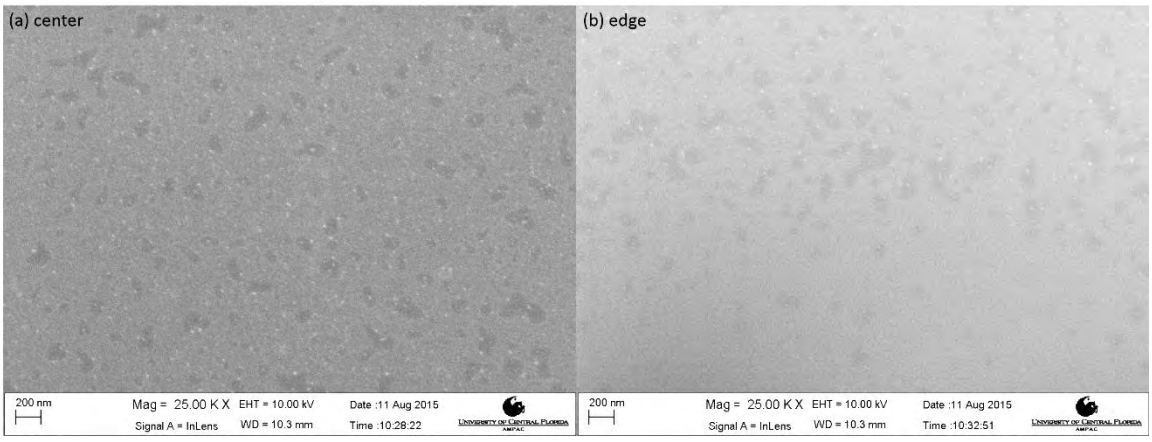

Fig. 3.35 (a) center and (b) edge of five second electrospray of $Ge_{23}Sb_7S_{70}$/ethanolamine on Si wafer

In Figure 3.35, similar feature sizes are present at both the edge and the center of the spray, indicating that there is minimal difference in the droplet sizes. At the edge, a fairly abrupt

cut-off is seen about halfway in the vertical direction of the micrograph. In addition, the appearance of necking between multiple droplets on the substrate indicates that wet deposition is occurring even at the far edge of the film. Therefore, it is concluded that incomplete coverage plays the largest role in the observed increase in roughness at the edges of the one-dimension multi-pass films of $Ge_{23}Sb_7S_{70}$.

As mentioned previously, substrate temperature also plays a significant role in determining the roughness of an electrosprayed film. It is possible that the substrate temperature is not optimized for the lower rate of material deposition at the film edges. This was investigated by depositing films with varying substrate temperature, shown in Figure 3.36 below.

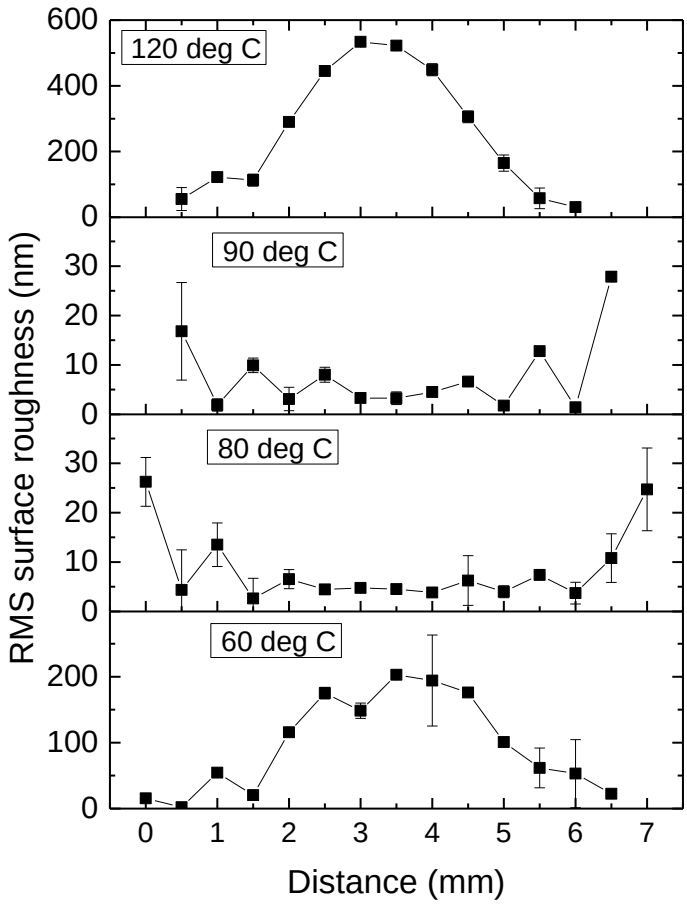

Fig. 3.36: RMS roughness across $Ge_{23}Sb_7S_{70}$ films made with eight passes at 24 mm/min, 5 mm working distance, and flow rate of 10 µL/hr, while varying substrate temperature

There is not a strong effect of substrate temperature on edge roughness, which is summarized in the following table.

Table 3.7: Edge roughness of the samples in Figure 3.33

Temperature (°C)	RMS roughness at edges of film (nm)	
60	15	23
80	26	25
90	17	27
120	51	36

This further supports that incomplete coverage plays the biggest role in the edge roughness of electrosprayed films. Edge roughness is seemingly unavoidable for thinner films, but this region is also likely to be quite small, depending on the amount of material which is deposited.

Effective GRIN (e-GRIN) films were then fabricated based on the previous results with sloped films. The $Ge_{23}Sb_7S_{70}$ films were made using 8 passes at 24 mm/min, and the As_2S_3 films were made using 8 passes at 20 mm/min, both at a working distance of 5 mm and flow rate of 10 μL/hr. The expected film center thickness was 400 nm, with a 3 mm offset between the films. In the first attempt, the $Ge_{23}Sb_7S_{70}$ film was deposited, then fully cured according to the annealing optimization study in Section 3.3, with annealing at 200°C under vacuum for 16 hours. The As_2S_3 film was then deposited, and fully cured under vacuum for 1 h each at 100°C and 125°C, and 3 h at 150°C. It was found that the As_2S_3 film lost material at the edges when annealing at 175°C under vacuum, so the annealing protocol was restricted to lower temperatures. The surface profile and optical microscopy of this sample are shown in the following figures.

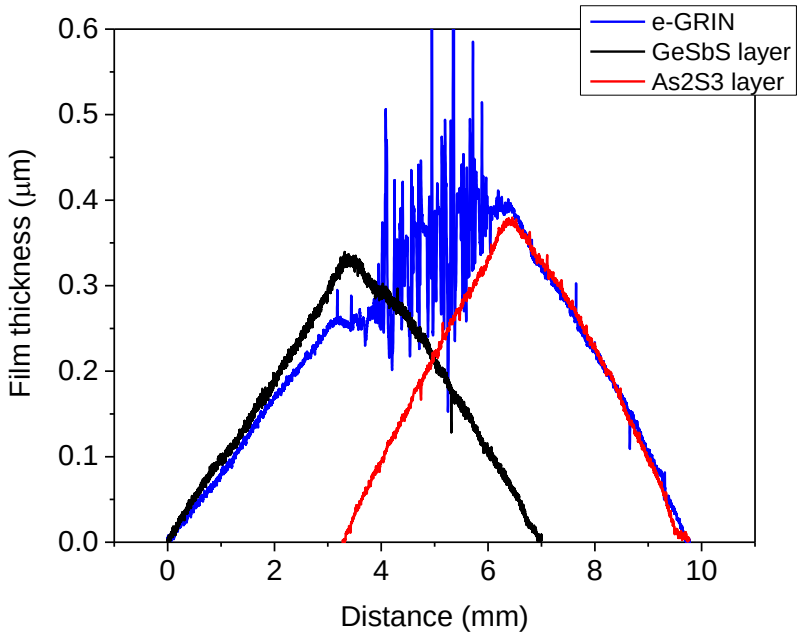

Fig. 3.37: Surface profiles of single layer films and e-GRIN film made with full cure of $Ge_{23}Sb_7S_{70}$ layer before deposition of As_2S_3 layer

From this film profile, it is seen that a lot of roughness was induced in the center region of the multi-layer e-GRIN film. Figure 3.38 below shows a photograph and optical micrograph of the e-GRIN film.

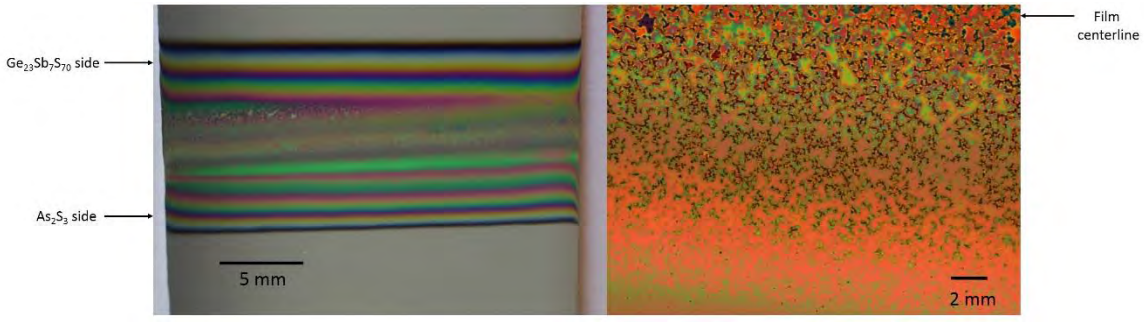

Fig. 3.38: Photograph (left) and optical micrograph (right) e-GRIN film made with full cure of $Ge_{23}Sb_7S_{70}$ layer before deposition of As_2S_3 layer

The roughness is induced by re-dissolution of the fully cured $Ge_{23}Sb_7S_{70}$ film by the As_2S_3 layer. In order to obtain better film quality, the As_2S_3 film was deposited on the un-cured $Ge_{23}Sb_7S_{70}$ film, and the entire multi-layer film was then heat treated with optimized annealing conditions for As_2S_3. These annealing conditions are not optimal for the $Ge_{23}Sb_7S_{70}$ film, which requires higher temperatures and longer annealing times to minimize the amount of residual solvent. The surface profile and photograph of this film are shown in the following figures.

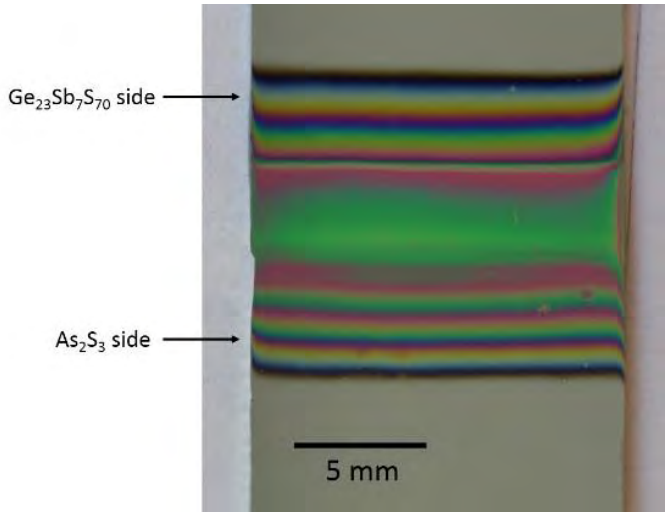

Fig. 3.39: Photograph of multi-layer GRIN film made with As_2S_3 layer deposited on un-cured $Ge_{23}Sb_7S_{70}$ film

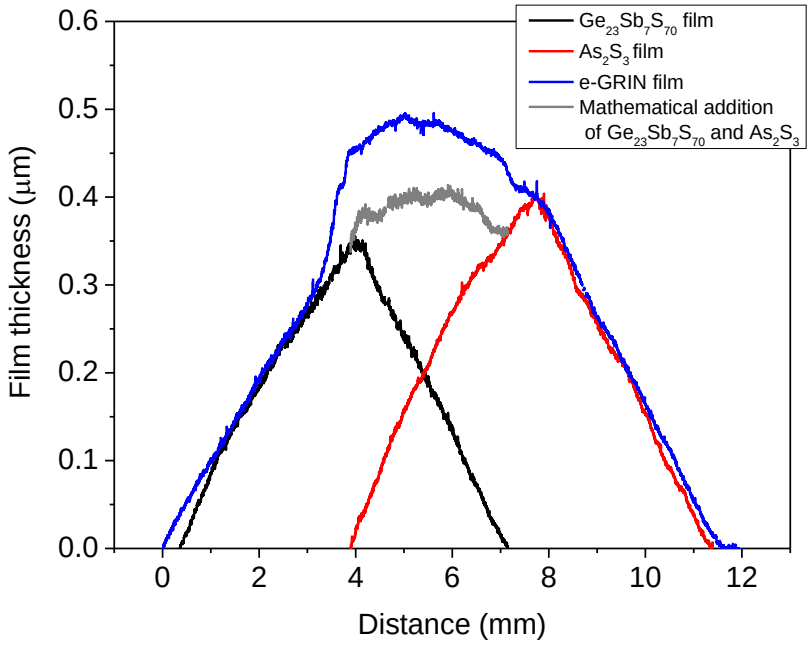

Fig. 3.40: Surface profile of single layer and multi-layer GRIN film made with As_2S_3 layer deposited on un-cured $Ge_{23}Sb_7S_{70}$ film

From the thickness profiles shown in Figure 3.38, a prediction of the refractive index across the film can be plotted, which is shown in Figure 3.40. This prediction is based on the volume percent of each glass composition, estimated by the thickness of the individual film profiles, and shown in Equation 3.11 below, where t_G and t_A are the thicknesses of the $Ge_{23}Sb_7S_{70}$ and As_2S_3 films, respectively, and n_G and n_A are the refractive indices of the $Ge_{23}Sb_7S_{70}$ and As_2S_3 films, respectively, which were measured in Section 3.3.

$$n_{eff} = \frac{(t_G)(n_G)+(t_A)(n_A)}{(t_G+t_A)} \quad \text{(Eq. 3.12)}$$

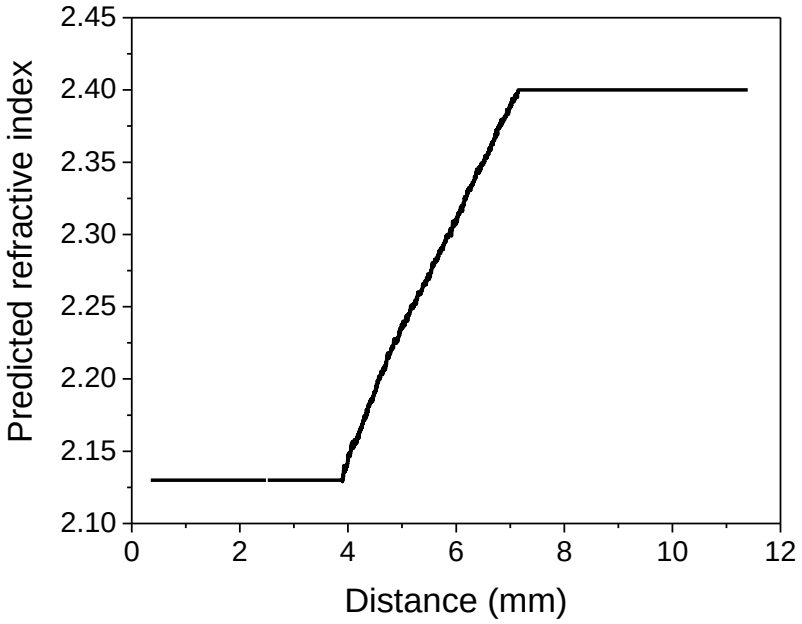

Fig. 3.41: Predicted refractive index of multilayer e-GRIN film

Based on the linear change in the thicknesses of the films, a linear change in the volume percent of each material is expected, leading to a potentially linear change in the refractive index of the film. However, this is not necessarily representative of the gradient that would be seen by the evanescent component of light traveling through a resonator, as there is also a change in film composition throughout the thickness of the film, and the intensity of the evanescent component would decrease as well in the same direction into the coating. Therefore, the predicted refractive index is more applicable to a true GRIN coating made with simultaneous spray of the two solutions. Efforts are currently underway to measure the refractive index across the multilayer e-GRIN film utilizing ellipsometry.

Just like most other components of a planar photonic device, low RMS roughness is desirable in a GRIN film to minimize optical loss. This was mapped over the e-GRIN film, which is shown in Figure 3.42.

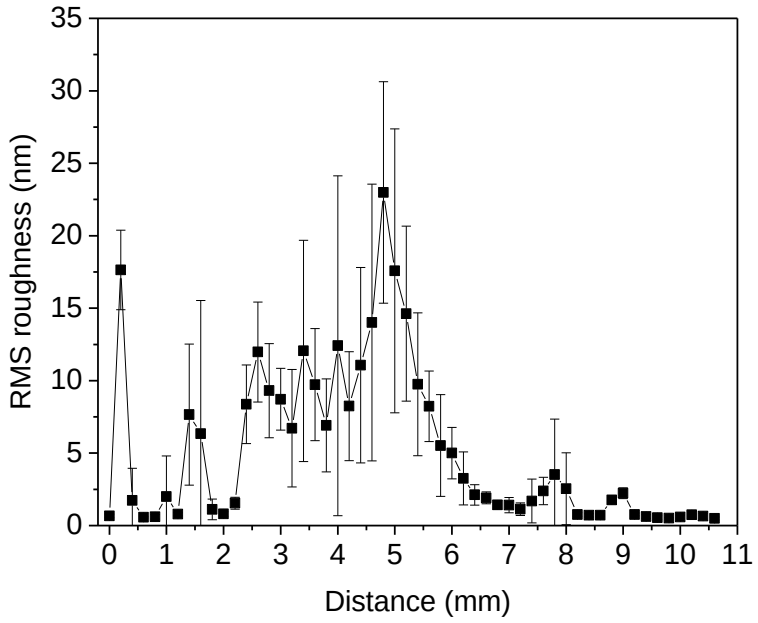

Fig. 3.42: RMS roughness mapping across e-GRIN film, with the left side being the $Ge_{23}Sb_7S_{70}$ side, and the right side being the As_2S_3 side

First attempts at GRIN films were seen to crack upon annealing. In these experiments, the deposition of $Ge_{23}Sb_7S_{70}$ was done at 80°C, and the As_2S_3 was deposited at 60°C. It was believed that the cracking was because the as-deposited $Ge_{23}Sb_7S_{70}$ films are known to contain more residual solvent than the As_2S_3 films, and shrink more during annealing as a result. In order to prevent cracking, the deposition temperature of $Ge_{23}Sb_7S_{70}$ was simply increased to 90°C to obtain a dryer as-deposited film. In Figure 3.38, the expected edge roughness is observed on the $Ge_{23}Sb_7S_{70}$ side of the film. In the center, overlapping region of the film, there is increased roughness compared to the individual $Ge_{23}Sb_7S_{70}$ and As_2S_3 films, which is probably a similar redissolution effect that was observed when coating a fully-cured $Ge_{23}Sb_7S_{70}$ with As_2S_3, but smaller in magnitude.

SIMS shows no distinct transition between the two layers. The film is milled from the top down using a Cs-ion beam, and the resulting secondary ejected particles are identified by a mass spectrometer. Therefore, the top of the film, is analyzed first, at t=0 seconds. At some point ranging from t=250 seconds to t=650 seconds, the counts/second for Si increase sharply, meaning that the surface of the substrate has been reached. The figures below show SIMS data for three different spots on the film, with the distances noted according to the previous figures showing the thickness profile of an e-GRIN film. Figure 3.42 is the $Ge_{23}Sb_7S_{70}$-rich side of the film (distance of ~4 mm), Figure 3.43 is the center of the film (distance of ~6 mm), and Figure 3.44 is the As_2S_3-rich side of the film (distance of ~8 mm). In these experiments, the presence of organics was ignored, and only the response from the glass elements (Ge, Sb, As, S) and the substrate (Si), were considered.

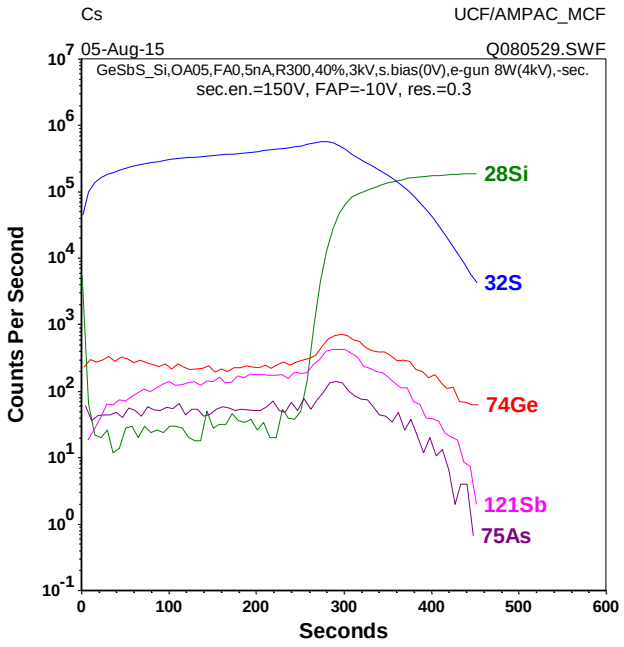

Fig. 3.43: SIMS at the $Ge_{23}Sb_7S_{70}$-rich region of an e-GRIN multilayer film

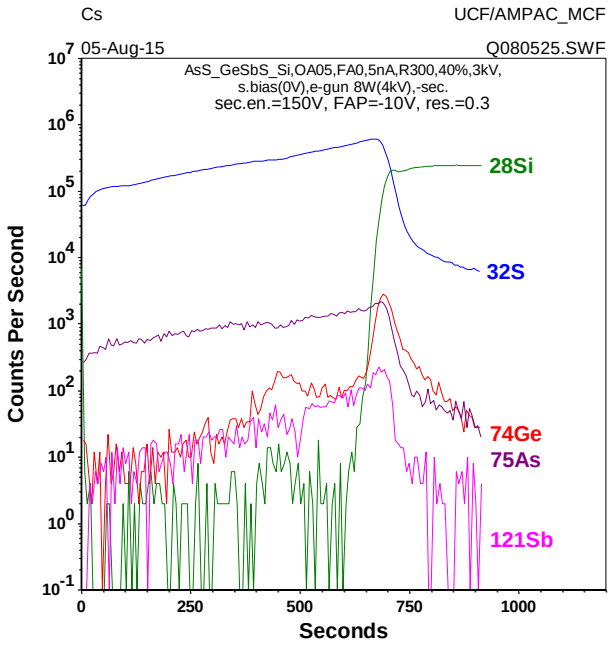

Fig. 3.44: SIMS at the center region of an e-GRIN multilayer film

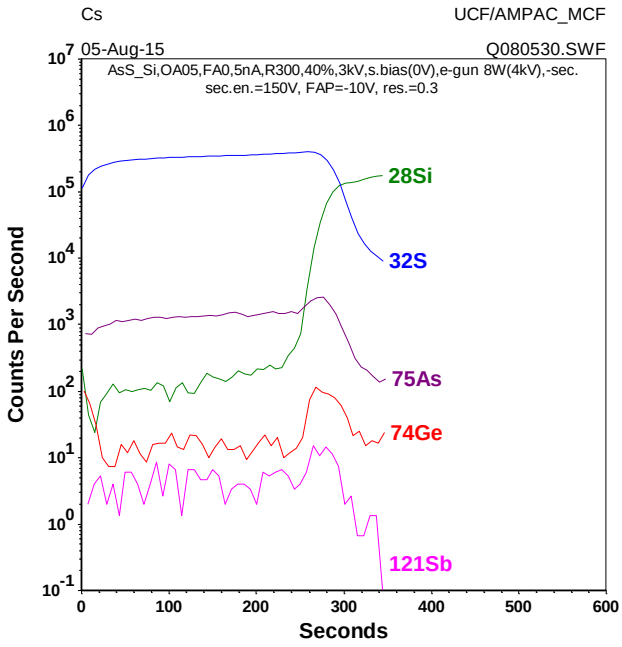

Fig. 3.45: SIMS of an As_2S_3-rich region of an e-GRIN multilayer film

First, it is noted that the center region of the film appears to be thicker than the other regions analyzed, based on the time to mill through the film to the Si substrate. In the $Ge_{23}Sb_7S_{70}$-rich region, Ge has more counts/second throughout the experiment, while As has more counts/second throughout the experiment in the As_2S_3-rich region. In the center region, As has more counts/second. One main source of error for this data is that As and Ge have very similar atomic masses (75 and 74, respectively). This makes it difficult to discern between the two elements. Furthermore, it is possible to detect As from Ge plus hydrogen, which possibly leads to the significantly higher counts recorded for As. The SIMS data confirms the gradient in chemistry across the film.

A slice from the center of the GRIN film was lifted out and the cross-section analyzed with TEM and EDS. Figure 3.46 shows a micrograph of the cross-section of this film. The Au-Pd sputtered layer was deposited before the Pt layer in order to minimize interaction between the ChG and Pt.

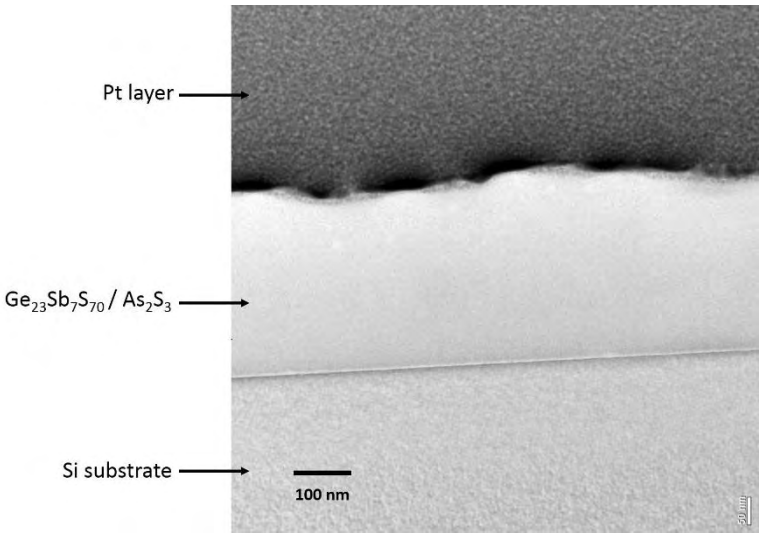

Fig. 3.46: Cross-sectional TEM at center of GRIN film

No distinct interface is seen between the $Ge_{23}Sb_7S_{70}$ and As_2S_3 layers. This was investigated further with EDS mapping, shown in Figure 3.46 below. With the ~100 nm thick slice in this case, there is a very small interaction area between the beam and the material, allowing high spatial resolution of the EDS, and in some cases atomic resolution can be achieved [101,102]. Thus, EDS line scan in TEM is suitable to investigate the composition of this film along the thickness of ~400 nm. Further supporting this is the very sharp interface identified between the ChG film and the Si wafer below.

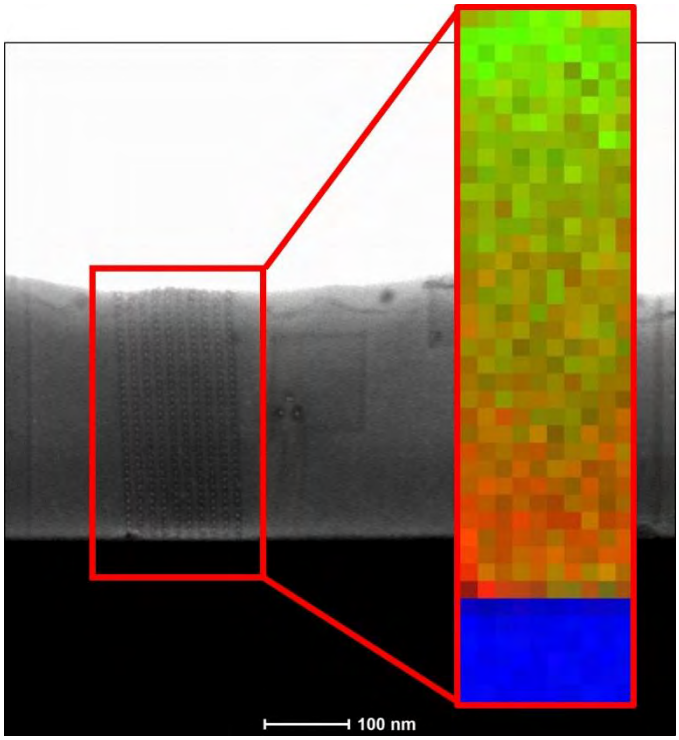

Fig. 3.47: EDS map of GRIN film, where red represents the presence of Ge, green is As, and blue is Si.

In Figure 3.47, the EDS map was made by taking an array of point scans, 10 columns and 40 rows (within the red box). Each point on the film cross-section appears as a damaged area in the micrograph, which was taken after the EDS map was complete. The colors in

this composition map were generated by the relative EDS peak heights between arsenic and germanium. As such, the data is purely qualitative, and indicates a gradual change in the composition of the film throughout the film thickness. Despite that the films were deposited in separate layers, they two compositions mix to some degree and there is no sharp interface between the films, which is likely a result of partial redissolution of the existing $Ge_{23}Sb_7S_{70}$ layer by the arrival of still-wet As_2S_3 droplets, as well as perhaps diffusion of the two layers during annealing. This is an important result because the lack of a sharp interface between the layers means that little to no Fresnel loss would occur to light transmitted through this film. Furthermore, it opens up the possibility to design a GRIN through the thickness of multi-layer electrosprayed films (z-direction), in addition to the GRIN across a substrate (x-y plane). Such a coating, made from multiple blanket films, could conceivably be used as an anti-reflective coating for a bulk optic, or may have interesting applications in planar photonics. This result illustrates how electrospray is an additional tool in ChG photonics, allowing a simple method of fabricating gradients in all three dimensions and giving optical designers additional degrees of flexibility when designing a device.

Finally, while multi-layer films provide great potential for a method of fabricating a GRIN coating, GRIN coatings by simultaneous spray is also proposed. This could be done by using positive voltage for both solutions, or one positive and one negative, as depicted in Figure 3.48 below.

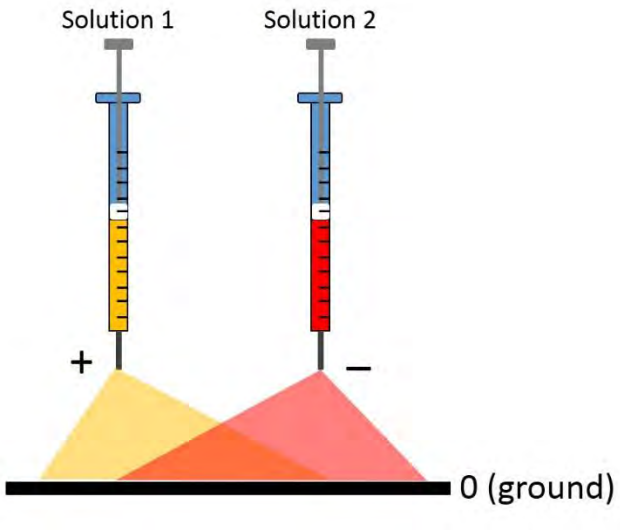

Fig. 3.48: Simultaneous spray of two solutions to generate true GRIN coating

Due to one solution being sprayed with a positive bias, and one with a negative bias, this would create droplets of solution 1 being charged oppositely than that of solution 2. This would promote mixing of the two solutions to some degree, as the oppositely charged droplets would be attracted to each other. Currently, electrospraying a ChG solution using a negative voltage has not been attempted. It is proposed to utilize glass solutions from the same family for a true GRIN, such as $As_{20}S_{80}$ ($n \sim 2.2$) and $As_{40}S_{60}$ ($n \sim 2.4$), which could allow a similar Δn as the $As_{40}S_{60}/Ge_{23}Sb_7S_{70}$ studied in this dissertation. These compositions would be more likely to have similar optimal annealing parameters, unlike $As_{40}S_{60}/Ge_{23}Sb_7S_{70}$, and may also be less likely to crack in a multilayer or true GRIN coating.

Data summary:

The data in Chapter III demonstrate that it is possible to create $Ge_{23}Sb_7S_{70}$ and As_2S_3 films from ethanolamine derived solutions using electrospray which are suitable for use in an optical device. This includes optimization of the annealing conditions for minimal residual solvent remaining, low roughness film surface, and the ability to fabricate blanket films with tunable thickness utilizing a serpentine path of the spray over the substrate. An initial demonstration of a multilayer e-GRIN coating was done by exploiting the nature of electrospray to result in non-uniform thickness films with 1-D passes of the spray. For the processing parameters used, the composition of the film is varied approximately linearly over ~3 mm, with a predicted linear change in refractive index from 2.13 to 2.40 over this distance. The composition of this film also changes gradually from top to bottom, with no sharp interface between the two layers, which is believed to be due primarily to re-dissolution of the first layer by the second layer. The roughness of the e-GRIN film was characterized, as well as the roughness of the individual films used. It was found that the films are generally smooth, with less than 10 nm RMS roughness, except for an increase in roughness at the film edges, which is due to incomplete coverage of the film on the substrate.

IV. QUANTUM DOT DOPING IN CHALCOGENIDE GLASS FILMS

While Chapter III discussed the optimization of deposition conditions for undoped blanket films of As_2S_3 and $Ge_{23}Sb_7S_{70}$, as well as demonstrated an approach to obtaining mid-IR GRIN coatings, Chapter IV will build on those results and explore nanoparticle doping, another potential advantage of electrospray. In this chapter, the incorporation of luminescent QDs into ChG films was done by both spin-coating and electrospray. Initial studies, done during the author's MS thesis and shortly after the completion, were on CdSe and PbS QDs in only spin-coated $Ge_{23}Sb_7S_{70}$. This consisted of proof-of-concept experiments in which steady-state photoluminescence was measured, along with luminescent lifetimes to compare the performance of the QDs in different environments, and TEM to characterize dispersion.

Electrospray of ChG was subsequently developed in an effort to reduce the aggregation of the QDs in the deposited film. In parallel, optimization of QD surface chemistry for the ChG solutions was carried out to enable integration onto photonic platforms where active structures are required. Ultimately, it is sought to improve dispersion by the quicker electrospray drying kinetics, and isolation of individual QDs in each aerosol droplet. Experimental determination of initial droplet size during electrospray was done to understand the optimal loading levels of the QDs in the film. Dispersion of QDs in spin-coated and electrosprayed films was then compared, as well as photoluminescence of the QDs in solution and in films deposited with different methods. The QDs in this study emit in the range of about 600 to 1400 nm. While this is not in the

desired operation range for proposed use in mid-IR chemical sensing devices, it is convenient to use these well-studied QDs with more easily measurable luminescence in the visible and near-infrared range. Once the principles of QD dispersion and luminescence in ChG films are understood, they can be applied to QDs which emit in the desired range, as described in Section 1.2.4.

4.1. Previous work and initial studies

The main subject of this author's MS thesis was the incorporation of PbS and CdSe QDs into spin-coated $Ge_{23}Sb_7S_{70}$ films. Since the conclusion of the MS thesis, experiments continued on these samples to better understand the properties of the films. In this section, data which originally appeared in the MS thesis is described as so.

In these initial doping experiments, QDs dispersed in chloroform solvent were mixed with the $Ge_{23}Sb_7S_{70}$/propylamine solution prior to spin-coating. Despite that the QD surface chemistry was not optimized for amine solvent, photoluminescence from the doped films was observed, which are shown in the Figures 4.1 and 4.2 below. Both PbS QDs capped with thioctic acid, and CdSe/ZnS core-shell QDs capped with tri-octyl phosphine oxide (TOPO) were incorporated into $Ge_{23}Sb_7S_{70}$ films made by spin-coating. In retrospect, the photoluminescence spectra of pure chloroform and the undoped $Ge_{23}Sb_7S_{70}$ film should have been included, but it is believed that they would not show any significant luminescence response in this range.

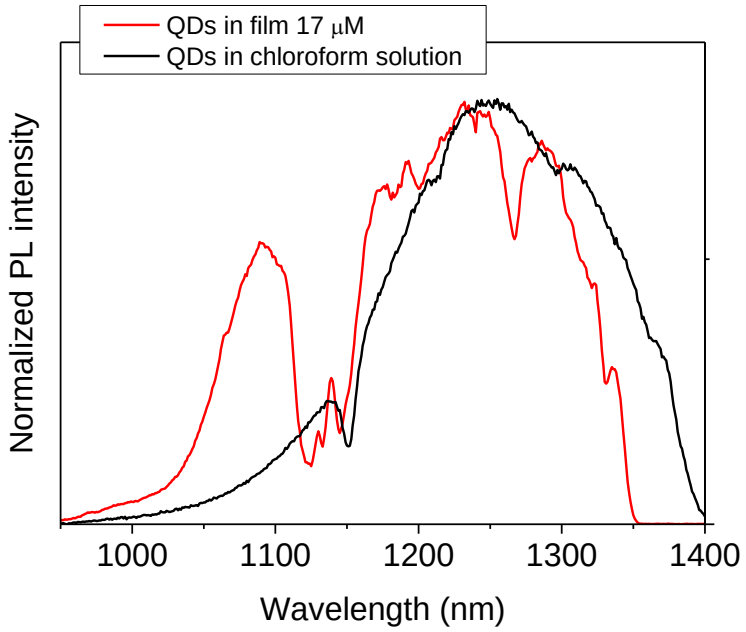

Fig. 4.1: Comparison of the steady-state photoluminescence spectra of PbS QDs dispersed in pure chloroform and in the spin-coated $Ge_{23}Sb_7S_{70}$ film matrix, taken from reference [53]

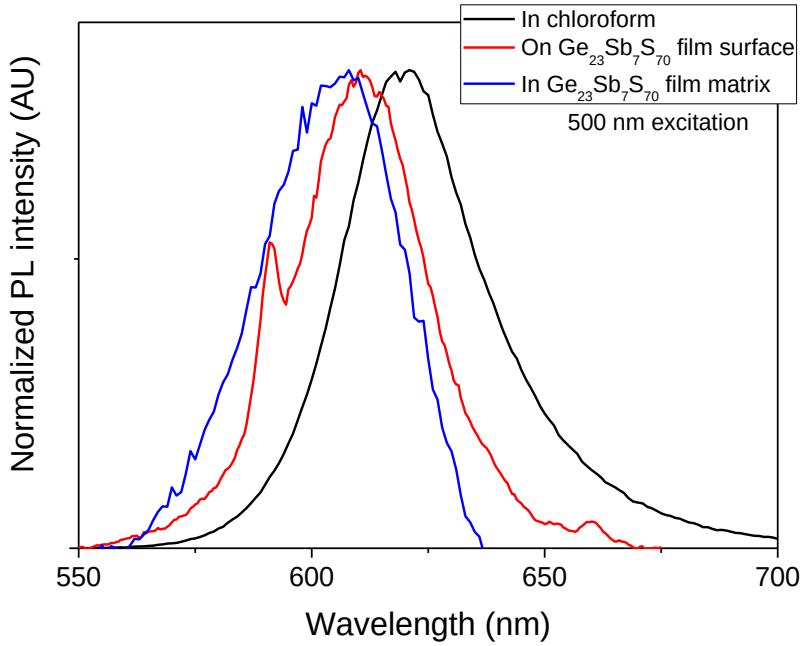

Fig. 4.2: Comparison of the steady-state photoluminescence spectra of CdSe/ZnS core-shell QDs dispersed in pure chloroform, on $Ge_{23}Sb_7S_{70}$ film surface, and in the spin-coated $Ge_{23}Sb_7S_{70}$ film matrix. Taken from reference [53].

One of the main goals was to understand how the emission efficiency trended throughout processing from QDs in pure chloroform to incorporation into the film matrix throughout a series of anneals. These anneals were optimized to remove the residual amine solvent from the film [43], as amines are known to quench luminescence due to their easily oxidized lone pair of electrons [103]. This is evidenced by the Stern-Volmer plot in Figure 4.3.

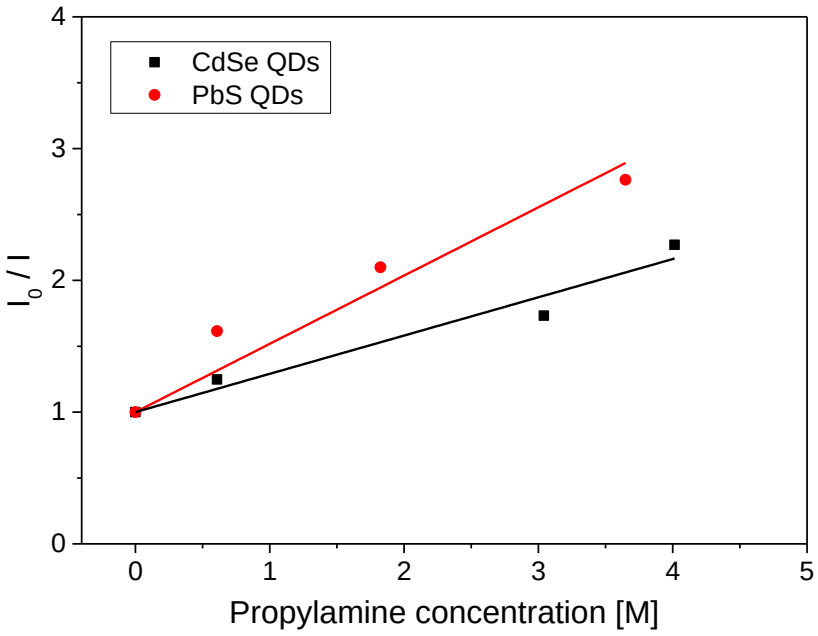

Fig. 4.3: Stern-Volmer plot of CdSe and PbS QDs dispersed in chloroform, and diluted with propylamine

The Stern-Volmer relationship for collisional quenching is given by Equation 4.1, where I_0 and I are the PL intensities of QDs (dispersed in pure chloroform) with propylamine

concentration of 0 and [Q], respectively, and k_{sv} is the Stern-Volmer constant equal to the product of k_q, the quenching rate constant, and τ_0, the unquenched lifetime.

$$\frac{I_0}{I} = 1 + k_{SV}[Q] = 1 + k_q\tau_0[Q] \qquad \text{(Eq. 4.1)}$$

For the CdSe QDs, k_{SV} was found to be 0.29, and for the PbS QDs, k_{SV} was found to be 0.52. In this plot, I_0 and I are normalized to the QD concentration. Therefore, the observed increase in I_0/I with the concentration of propylamine is evidence of quenching behavior. Due to this quenching, complete or near-complete removal of residual amine solvent from the film is very important. In order to quantify this, the integrated area beneath the steady-state emission spectra of the QD-doped films was plotted throughout the series of anneals, which is shown in Figure 4.4.

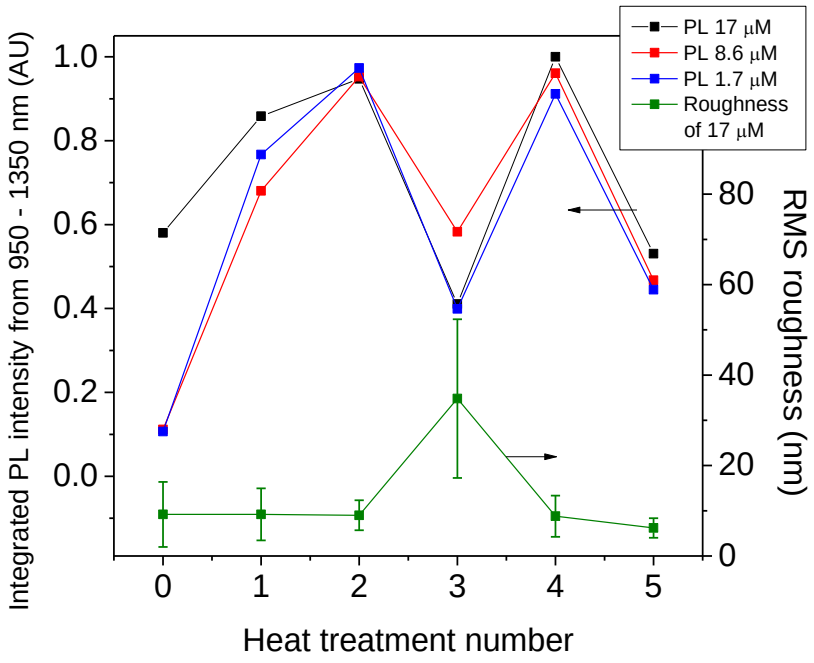

Fig. 4.4: Integrated steady-state photoluminescence intensity for varying concentration of PbS QDs in spin-coated $Ge_{23}Sb_7S_{70}$ films, and RMS surface

roughness of those films throughout a series of sequential heat treatments. Taken from reference [53]

It should be noted that steady-state luminescence measurements are not truly quantitative, because the intensity recorded by the detector can vary because of reasons such as variations in the orientation of the sample, and intensity of the excitation. For this reason, luminescence lifetime measurements were also taken, presented in Table 4.1 The steady-state data implies that emission intensity generally increases as the film is annealed. As expected, the intensity increases most rapidly for the first few heat treatments, as this is when solvent is most rapidly removed from the film. After that, solvent is removed progressively slower, so emission intensity should increase at a progressively slower rate and then level off. This is what is observed, with the exception of two anomalies, HT3 and HT5. It is seen that the reduction in emission intensity is correlated with an increase in surface roughness. Therefore, it is believed that the increased roughness led to more scattering of both the excitation light and the luminescent light, reducing the apparent intensity recorded by the detector. In order to verify this, luminescent lifetimes of the samples were also taken throughout the series of anneals, shown in Table 4.1. It should be noted that previous studies have observed that the lifetime of a luminescent, rare-earth doped nanocrystal varies depending on the refractive index of the surrounding medium [104,105]. Specifically in those studies, the lifetime decreases when the refractive index of the medium increases. Thus, environmental effects must be taken into consideration when analyzing the following lifetime data.

Table: 4.1: comparison of luminescent lifetimes for PbS QDs in pure chloroform, to PbS QDs in spin-coated $Ge_{23}Sb_7S_{70}$ film

	Lifetime (ns)	Solvent peak absorption size ($\%T*cm^{-1}$) error is +/- 10%
In pure chloroform	78	-
HT0	-	662
HT1	-	439
HT2	29	387
HT3	42	168
HT4	53	107
HT5	61	82
HT5 repeat	30	-

The increasing lifetime values correlate with the removal of solvent as characterized by the solvent peak absorption area determined from the transmission FTIR spectra of these films. Additionally, the lifetime increases progressively from HT2 to HT5, supporting the theory that the apparent reduction in intensity is due to the increased surface roughness, as opposed to a reduction in the efficiency of the QDs. This occurs despite the increasing refractive index of the matrix throughout heat treatment, which was measured in another study [106]. Additionally, upon repeating HT5, lifetime decreased significantly. This implies that the QDs were "overheated" and provides an explanation for the reduction in apparent emission intensity for HT5. Finally, the lifetime of the QDs in the film matrix never reaches that of the QDs in pure chloroform, meaning that the QDs in the film have a reduced efficiency. This is explained by small amounts of residual solvent still present in the film, as well as aggregation of the QDs during the film deposition process. There is also possibly an effect from the higher refractive index of the film matrix vs. that of pure chloroform (~1.97 for the film and ~1.44 for chloroform at 650 nm) [106,107], though

quantifying this effect would require further experimentation. However, Figure 4.4 shows the photoluminescence intensity for three concentrations of PbS QDs in the ChG film matrix spanning one order of magnitude concentration are very similar throughout the entire series of anneals. As a result, it is believed that aggregation of the QDs is playing a significant role in determining the efficiency of luminescence, and that dispersion gets worse as the film is doped with higher QD concentrations. This is partially supported by TEM of the 17 μm (highest concentration) QD doped film, shown in Figure 4.5.

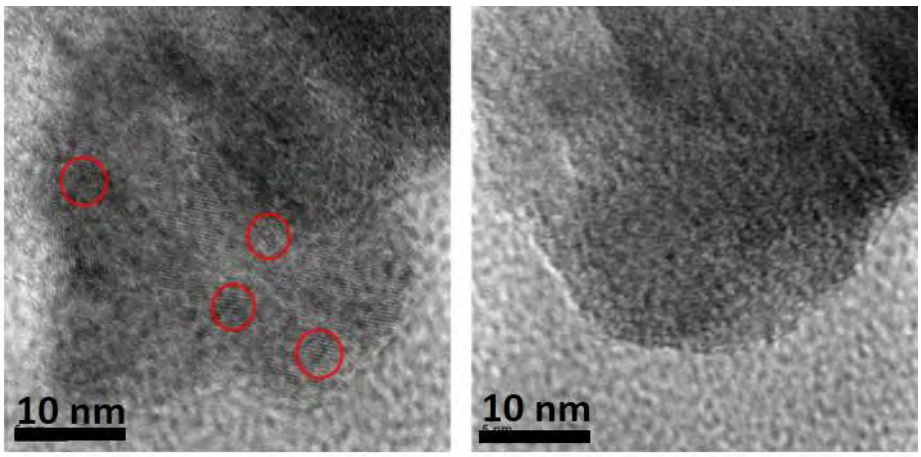

Fig. 4.5: Transmission electron microscopy of a PbS QD doped $Ge_{23}Sb_7S_{70}$ film. (a) is a region containing an aggregation of QDs, with four individual QDs circled in red as a guide to the eye and (b) is a region of the same film with no QDs present.

The QDs are identified by the visible order in the crystal lattice, compared to the amorphous matrix, and approximate size in the range of ~3-5 nm, which is expected based on the peak emission wavelength [53]. For this sample, pieces of the film were "chipped" off and placed on a TEM grid, and the lower concentration QD-doped samples were not analyzed with TEM, due to the difficulty of finding and identifying the QDs and general unreliability of the method. However, better experimental protocol for analyzing QD-doped ChG films

with TEM were established, which are shown later in this chapter. The conclusion from the initial doping experiments is that QDs can be used to realize luminescent behavior in solution-derived ChG films, but at a reduced efficiency. It is believed that aggregation is primarily responsible for this, and the focus of the experiments that followed was to improve the dispersion of the QDs in order to enhance the efficiency of the luminescence.

4.2. Electrospraying of QD-doped films

Two approaches toward improving nanoparticle dispersion were explored: the surface chemistry of the QDs (i.e. thermodynamic) and the processing method (studying the effect of drying kinetics). For improvements of the surface chemistry, we have collaborated with Dr. Manashi Nath's group at Missouri University of Science and Technology. This group has provided CdTe QDs capped with mercaptopropionic acid, which disperse in ethanolamine, the solvent used for the electrospray process.

The hypothesis behind the use of electrospray as a method of improving nanoparticle dispersion is that a single QD could be isolated inside of a droplet in order to prevent aggregation. As the droplets fall to the substrate, a certain degree of solvent evaporates from the drop, depending on the deposition parameters such as working distance between the nozzle and substrate and the flow rate, which affects the initial droplet size. This leads to an increase in droplet viscosity, providing a kinetic barrier to aggregation. The droplets are also charged, so they should not interact until they reach the substrate.

4.2.1. Initial droplet size during electrospray

In order to test this hypothesis, it is first necessary to understand the initial droplet size during electrospray. First, a literature model was used, shown in Equation 4.2, where d_0 is the initial droplet diameter, ρ is the liquid density, ε_0 is the vacuum permittivity, Q is the liquid flow rate, γ is the liquid-air interfacial tension, and k is the liquid electrical conductivity.

$$d_0 = \left(\frac{16\rho\varepsilon_0 Q^3}{\gamma k}\right)^{\frac{1}{6}} \qquad \text{(Eq. 4.2)}$$

Based on this equation, the expected initial droplet diameter at 10 µL/hr is 261 nm, using γ = 0.049 N/m (value of pure ETA) and a measured conductivity of the glass solution, k = $2x10^{-2}$ S/m.

In order to investigate droplet size experimentally, the glass solution was electrosprayed on a TEM grid for ~5 seconds at a working distance of 10 mm. It is proposed that atomic force microscopy (AFM) could also be used to analyze the surface profile of droplets and check the results of TEM, but this was technique was not available. Figure 4.6 shows a sample TEM image from such a sample.

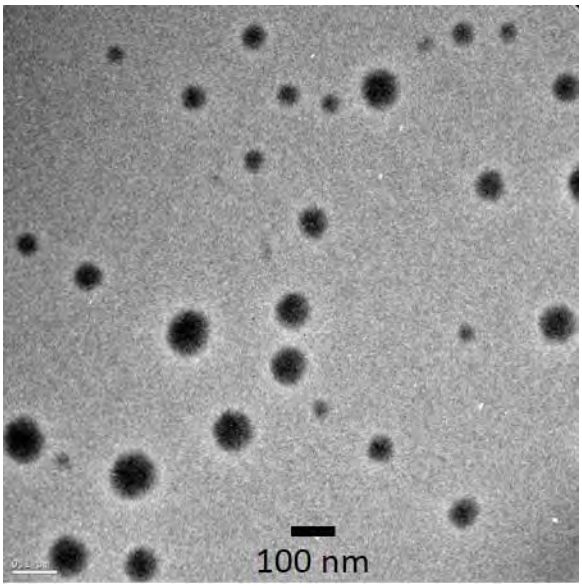

Fig. 4.6: TEM micrograph of short electrospray on a TEM grid. The dark regions are cured ChG and the light gray region is the amorphous carbon substrate.

As a first order approximation, the droplets were assumed to be hemispherical, and fully cured with the same density and composition as the corresponding bulk glass. This gives a volume of glass that can be correlated back to initial droplet size. Looking at over 60 drops across the grid, the following initial droplet size distribution was estimated and shown in Figure 4.7.

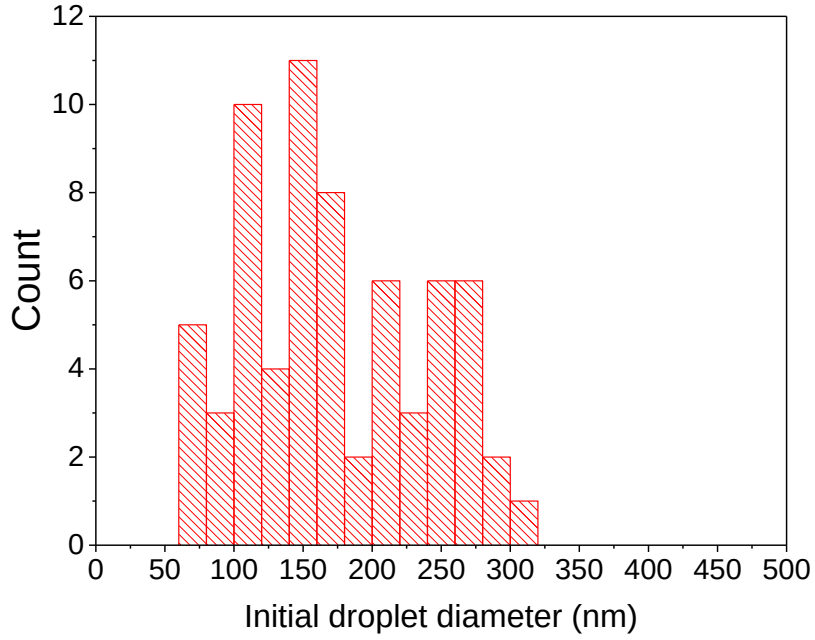

Fig. 4.7: Initial droplet size histogram of 0.05 g/mL $Ge_{23}Sb_7S_{70}$/ETA during electrospray determined from TEM micrographs, under the assumptions listed above.

The average initial droplet size in this estimation is 173 nm, lower than the prediction of 261 nm by Equation 3. There are several sources of error. First, the droplets undoubtedly have some solvent remaining, and are likely to be less dense as the bulk glass. It is also possible that there is some volatilization of material. Also, the profile of the droplets is actually believed to be parabolic, based on initial characterization with electron energy loss spectroscopy (EELS), shown in Figure 4.8.

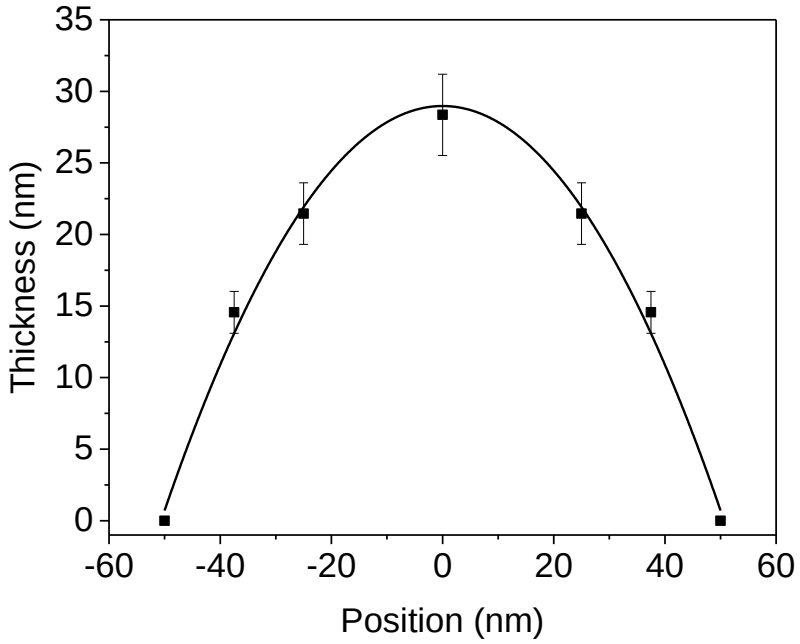

Fig. 4.8: EELS thickness profile of an electrosprayed droplet on a TEM grid

Figure 4.8 shows a parabolic surface profile, with center thickness of about 1.15 times the radius of the droplet. In order to obtain an accurate estimate of cured droplet volume, it will be necessary take EELS data on more droplets to further investigate the typical cured droplet shape, and to extract the relationship between droplet diameter (as seen in the TEM images) and droplet volume. This will allow a more accurate estimation of initial droplet size, combined with further investigation of how much material is lost during annealing.

4.2.2. Doping with CdTe QDs

These initial results were extended to QD-doped samples. First, pure CdTe with mercaptopropionic acid surface ligand provided by Dr. Nath's group, was dispersed in

ETA at a concentration of 0.1 mg/mL, and electrosprayed on a TEM grid, shown in Figure 4.9.

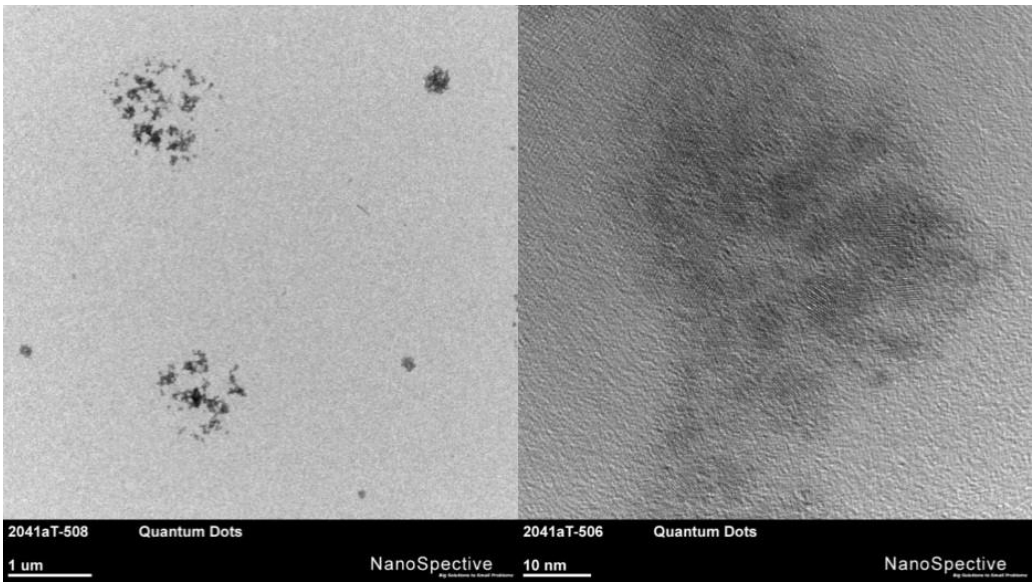

Fig. 4.9: TEM micrographs of pure CdTe QDs/ETA electrosprayed at 10 µL/hr

Clusters of QDs are seen where the droplets arrived at the substrate. From high magnification images, the QD diameter is estimated as 4.8 nm with a standard deviation of 1.2 nm.

TEM was also used to investigate electrosprayed QD-doped ChG solution, which is shown in Figure 4.10. As mentioned in Section 1.3, the QD concentration in this solution was 0.06 mg/mL, and the glass concentration was 0.045 g/mL. From the initial droplet size estimation using the hemispherical cured droplet assumption, it is expected that this solution would contain 0.4 QDs/droplet on average.

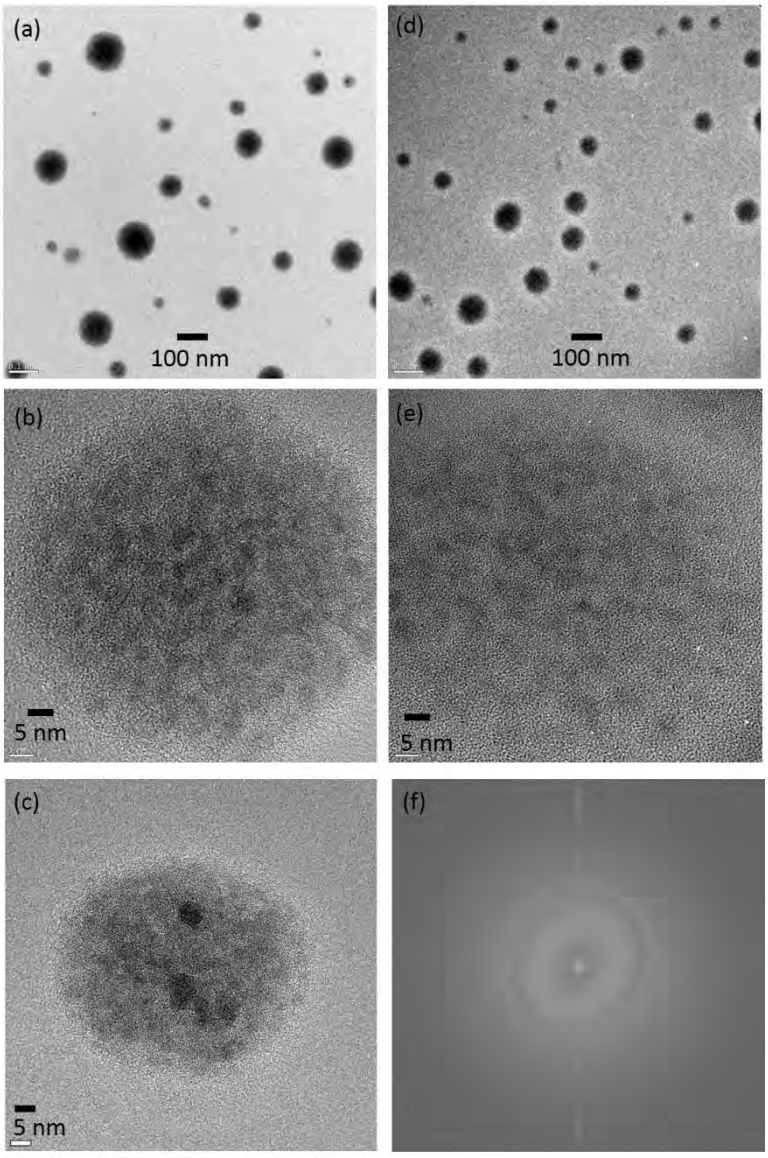

Fig. 4.10: TEM images of $Ge_{23}Sb_7S_{70}$ made by electrospray. A, B and C are CdTe QD-doped. D and E are undoped, and F is a fast Fourier transform (FFT) of image E.

From Figure 4.10, images A and D show a similar distribution of droplet sizes, with some regions of darkness and lightness in both doped and undoped samples. B and E are high magnification images, which show the regions of lightness and darkness in more detail. There are crystalline regions in both samples which are about 5 nm in dimension, which

was evident in the images from visible, ordered atomic planes, as well as polycrystalline diffraction rings in the Fast Fourier Transform (FFT) image. It is possible that the crystallinity is due to the volatilization of sulfur that is suspected during the annealing of these samples, leaving behind a composition that does not remain amorphous. Image C is a relatively small droplet from the doped sample, and in such droplets, there are very distinct dark regions that are believed to be the CdTe QDs. However, EDS data does not show evidence of CdTe in these samples, likely due to the very low volume percent of the QDs. There is more contrast between the QDs and glass matrix in the smaller droplets because they are thinner, but in general contrast is difficult due to the crystalline regions which are approximately the same size as the QDs.

In order to investigate the dispersion of QDs in the blanket film, which is more relevant to a device than the individual droplets, focused ion beam (FIB) milling was utilized to lift out a cross-sectional slice of a film. This sample was then analyzed with STEM, shown in Figure 4.11 below. STEM was used to allow more contrast between the features in the samples. Three layers of QD-doped $Ge_{23}Sb_7S_{70}$ were deposited, with sputtered Au-Pd layers between the ChG layers.

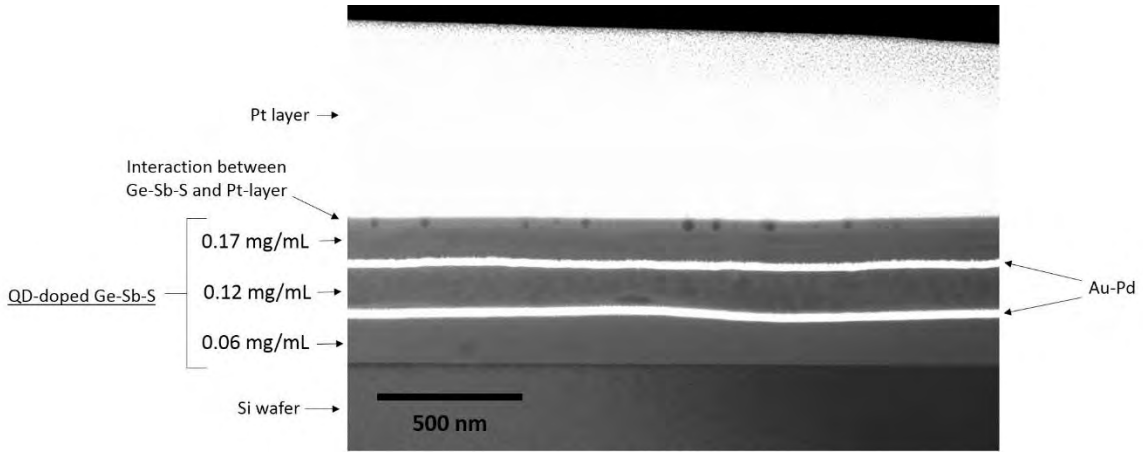

Fig. 4.11: STEM of three-layer, CdTe doped $Ge_{23}Sb_7S_{70}$ coatings made by electrospray

Note that the Pt layer is applied to the sample as protection during the FIB process, and interacts with the ChG film. In the future, an additional Au-Pd layer should be applied to the top film as well in order to prevent this interaction. Three concentrations of QDs were tested, 0.06 mg/mL, 0.12 mg/mL, and 0.17 mg/mL, which have expected average separation distances in the fully-cured $Ge_{23}Sb_7S_{70}$ film of 47, 37, and 33 nm, respectively. This calculation was based on the mass ratio of QDs to ChG, assuming that the film is fully cured with the same density of the bulk glass, and taking into account the approximate QD size of 5 nm diameter. Figure 4.12 below shows a higher magnification of the sample.

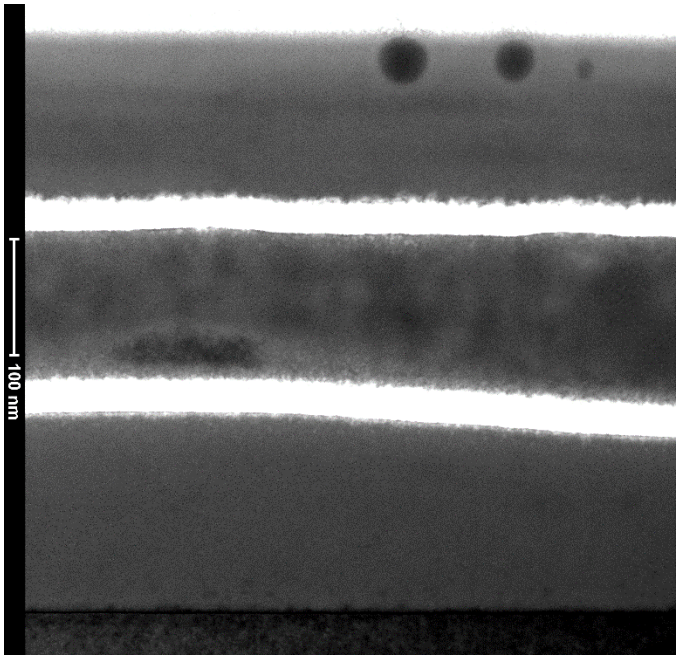

Fig. 4.12: STEM image of 5 nm CdTe QD-doped $Ge_{23}Sb_7S_{70}$ in the concentration of 0.06 mg/mL (bottom), 0.12 mg/mL (middle) and 0.17 mg/mL (top).

The dark circles in the top layer are pores which were induced by interaction between the Pt layer and the ChG, as these features are only seen near the top surface of the top film,

and EDX showed no difference in composition between the dark circles and the surrounding film. In the middle film, there are some darker and lighter regions. This could be a result from some spray instability causing localized variation in the density of the film.

A slice from a spin-coated film doped with CdTe QDs was also lifted-out for imaging with TEM. The concentration of QDs in this sample was 0.17 mg/mL, the same as the highest loaded electrosprayed film from Figure 4.13.

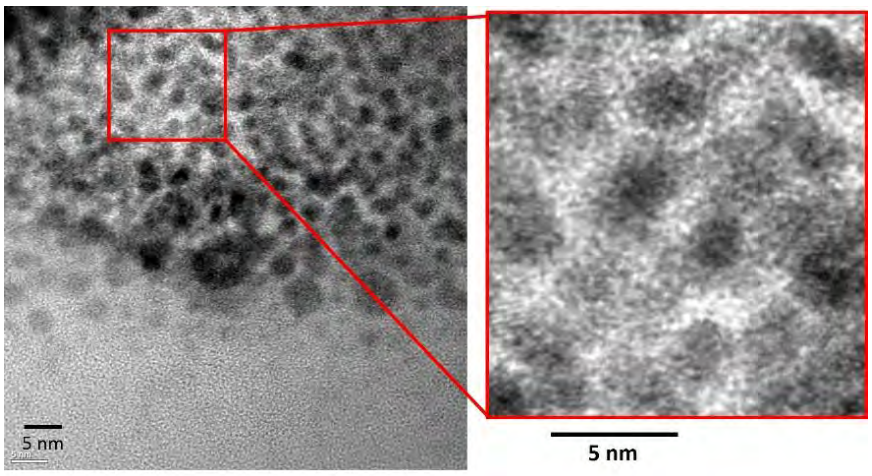

Fig. 4.13: TEM of cross-section of spin-coated film made from solution containing 0.05 g/mL $Ge_{23}Sb_7S_{70}$ and 0.17 mg/mL CdTe in ethanolamine

There appear to be regions of crystallinity in this sample, shown in the blown-up portion of the image. Although these regions of dark spots, which made up a large portion of the 50 nm thick film, appear to be large aggregates of QDs, EDS did detect the presence of CdTe in such a region. Most of the dark spots also appear to be 2-4 nm in size, which is less than the expected 4.8 nm diameter of the QDs. Therefore, absolute confirmation that the QDs are incorporated into the film could not be made.

In these samples, it is difficult to comment definitively on where the QDs are located, and their degree of dispersion. The thickness of the lifted-out slices is approximately 100 nm, which may simply be too thick to have good contrast between CdTe and $Ge_{23}Sb_7S_{70}$. Bulk CdTe has a density of 6.2 g/cm^3, while bulk $Ge_{23}Sb_7S_{70}$ has a density of 2.94 g/cm^3, so there may not be large differences in attenuation of electrons through a region where there is a single QD, and a region where there are no QDs. This would suggest insufficient contrast for visual identification of the QD either by its contrast or its crystallinity (diffraction) from the background glass matrix. As the QDs are only 5 nm in size, one can estimate that they only make up 5% of the thickness of the lifted-out slice; additionally, the image can be further convoluted by multiple QDs residing along the same path of the electron beam. In the case of the highest concentration of QDs in the electrosprayed film, the expected average separation distance between QDs is 47 nm, meaning that it is likely to have more than one QD on the same path in a 100 nm thick cross-section.

4.2.3. Experiments with commercial CdSe/ZnS core-shell QDs

In addition to the CdTe QDs provided by Dr. Nath's group, commercial CdSe/ZnS core-shell QDs capped with octadecylamine were tested, which were purchased from Ocean NanoTech. These QDs were found to disperse in ethanolamine at concentrations as high as 0.3 mg/mL. The absorption and PL spectra shown in Figure 4.14 below are from the manufacturer's product literature.

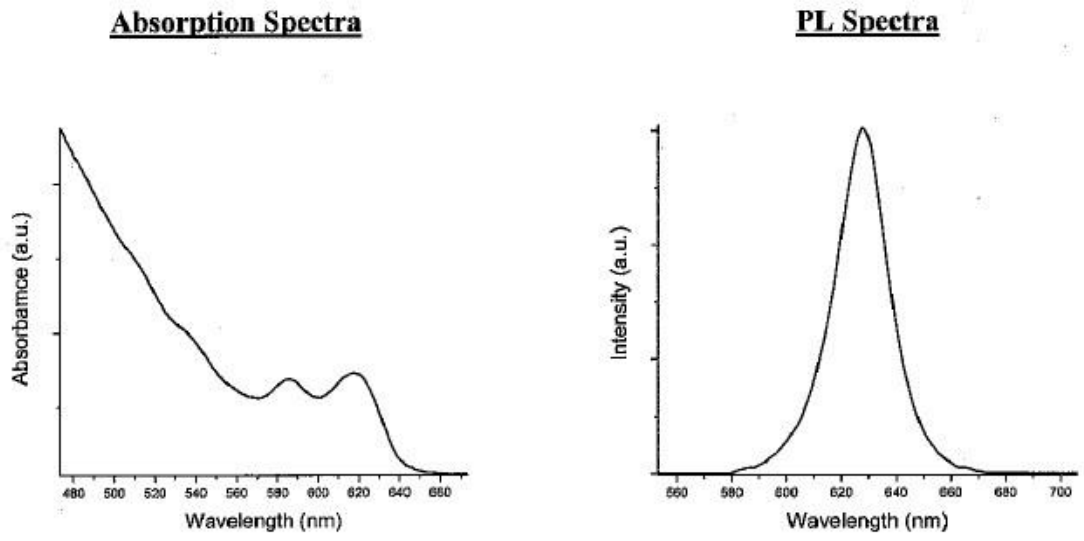

Fig. 4.14: Absorption and PL spectra of CdSe/ZnS core-shell QDs from Ocean Nanotech product literature

Based on the position of the expected emission, centered at 624 nm, the core CdSe is expected to have an average diameter of 5.85 nm, based on Equation 4.2 below, where λ is the peak emission wavelength [58]

$$D = (1.6122x10^{-9})\lambda^4 - (2.6575x10^{-6})\lambda^3 + (1.6242x10^{-3})\lambda^2 - (0.4277)\lambda + 41.57$$

(Eq. 4.3)

The total QD size, considering that the diameter is the sum of the core diameter plus shell thickness, was investigated by spraying pure QDs/ethanolamine on a TEM grid, with sample TEM micrographs shown in the following figure.

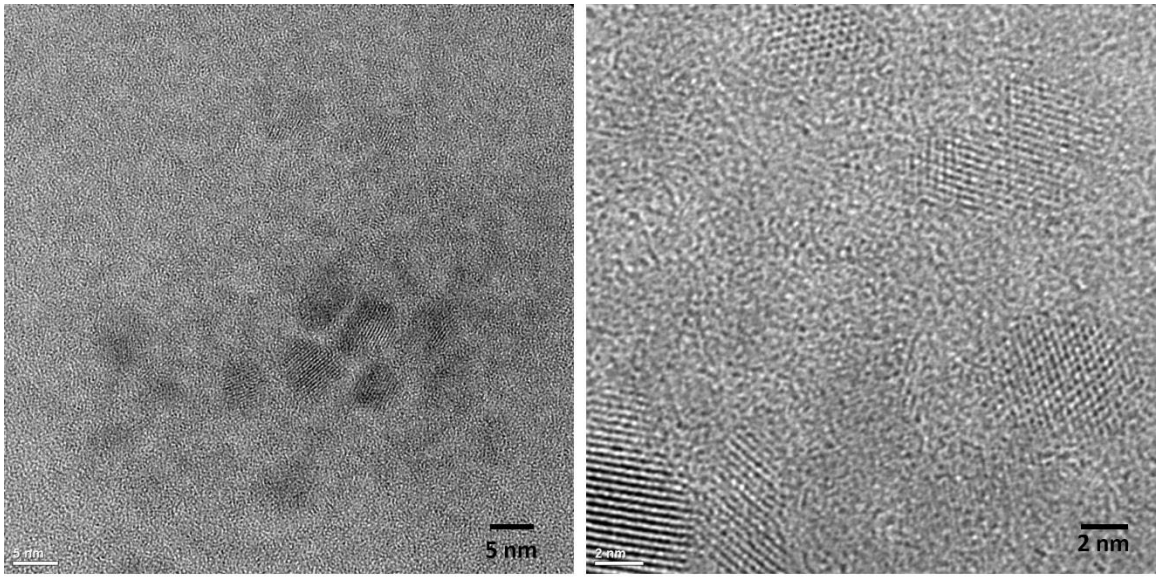

Fig. 4.15: TEM micrographs of CdSe/ZnS core-shell QDs electrosprayed on a TEM grid for ~1 s. The concentration of the QDs was 0.2 mg/mL, corresponding to a nominal 645 nm separation distance in the solution, assuming ideal dispersion.

Using the TEM micrographs, a total of eleven QDs were identified and measured in an effort to estimate the size of the QDs and calculate their dispersion. This resulted in an average QD diameter of 5.5 nm with a standard deviation of 0.95 nm. This total diameter (core + shell) is lower than the predicted core diameter of 5.85 nm from Equation 4.2. This is likely due to strain imposed on the core due to the shell, causing a red-shift of the band-gap [49]. It is also likely that the shell is very thin and does not add much to the total QD diameter, likely on the order of two monolayers, as this has been demonstrated to result in maximum quantum yield [49]. Based on the size of the QDs, the average separation distance between the QDs (used to estimate QD dispersion or distribution within the film) can be calculated from the loading level (mg/mL) of the QDs in the solution. These initial experiments were done using a 0.2 mg/mL dispersion of QDs in ethanolamine, which has a 645 nm separation distance between QDs. In this dispersion, $Ge_{23}Sb_7S_{70}$ was dissolved

to a concentration of 0.05 mg/mL. This solution was electrosprayed on a TEM grid by moving the spray at a velocity of 48 mm/min over the grid, with the intention of depositing a very thin film for analysis. This solution was also electrosprayed on Si substrates for luminescence studies. In these cured samples, the expected average separation distance is 70 nm, based on the ratio of QDs to glass.

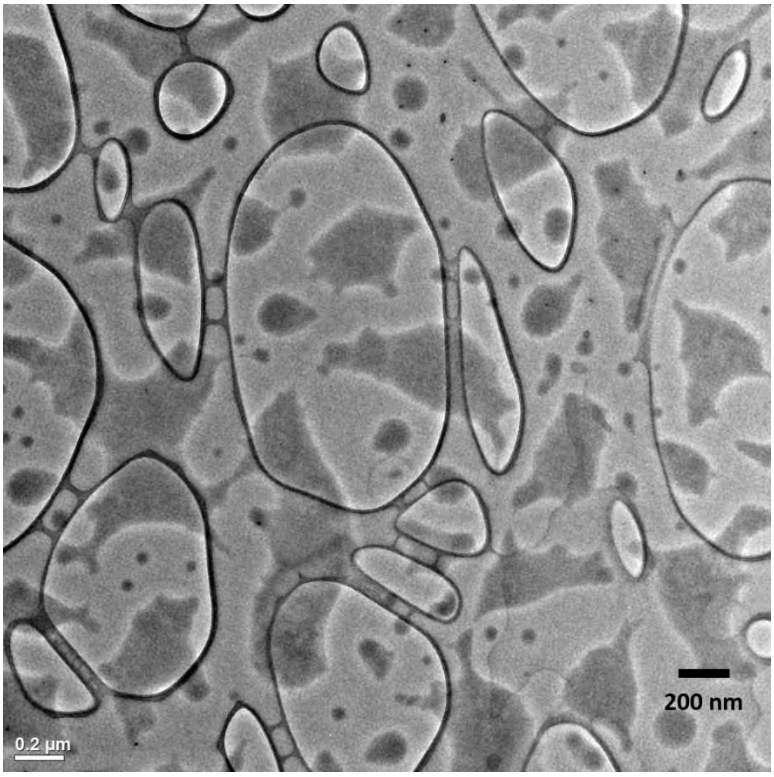

Fig. 4.16: TEM of CdSe QD-doped $Ge_{23}Sb_7S_{70}$ sprayed on grid with pass of 48 mm/min

This micrograph is an overview of the sample. The holey carbon webbing and ultra-thin carbon film appears light gray with very dark outlines of the holes in the carbon webbing. The ChG sample is a medium gray, and appears as irregularly shaped due to several

droplets coming together. Figure 4.17 below shows part of a QD-doped glass droplet under higher magnification, with a QD-containing area blown-up.

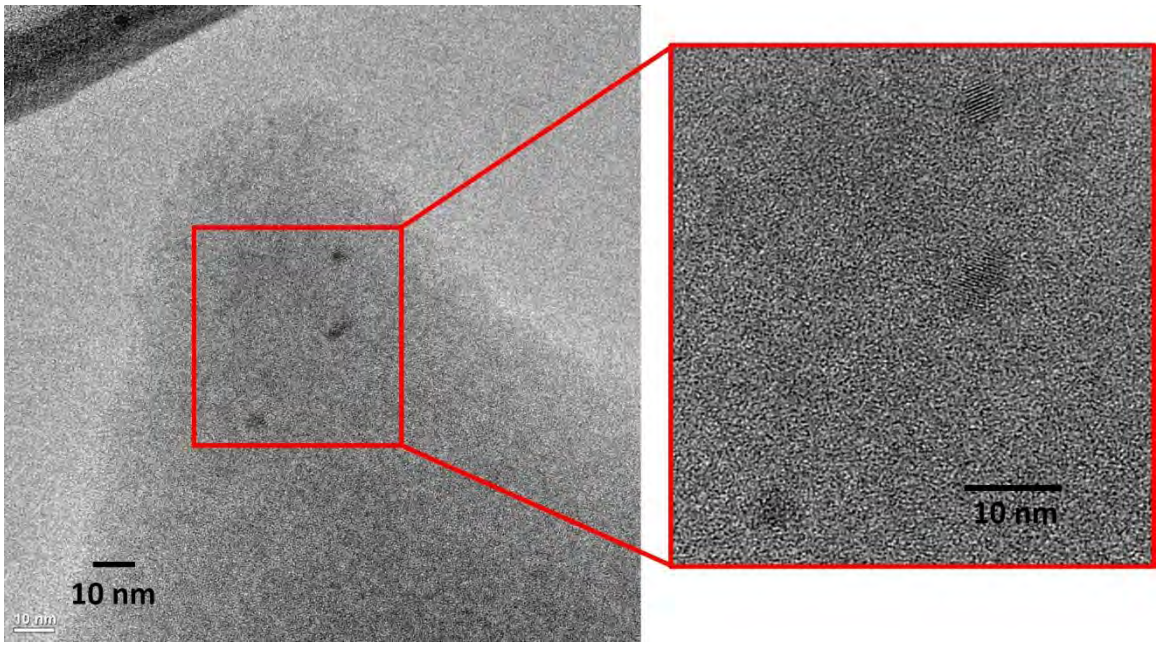

Fig. 4.17: CdSe QDs in electrosprayed droplets of $Ge_{23}Sb_7S_{70}$, concentration of 0.2 mg/mL, or 70 nm expected separation distance in the cured material

The appearance of dispersed QDs gives support to the idea that electrospray has potential as a method of enabling better dispersion of nanoparticles, especially given that these QDs are separated by as little as ~15 nm in this vicinity. However, the QDs in this sample do not appear as frequently as expected, based on the cured-film separation distance of 70 nm. One possibility is of course that the QDs are present, but there are still the issues with contrast discussed previously in this section. Another possibility is that the QDs do not make it into the film, but are instead expelled from the spray. This seems unlikely though because there was no difficulty finding the pure QDs sprayed on a TEM grid (Figure 4.15), and the concentration of the QDs was identical in both samples. Finally, it is perhaps

possible that the QDs dissolve in the glass matrix during annealing at high temperature. Future work will include investigation of these possibilities.

4.3. Luminescence studies of QD-doped films

Photoluminescence experiments were utilized to investigate the incorporation of both CdTe and CdSe QDs into $Ge_{23}Sb_7S_{70}$ films. The table below is an overview of the results obtained on the various systems utilized.

Table 4.2: Photoluminescence systems utilized to characterize QDs

System		Results	
Description	Excitation sources tested	CdTe QDs	CdSe QDs
Dr. Gaume's Ocean Optics QE Pro-FL at CREOL	532 nm laser pointer (~1.5 mW), 470 nm LED	No PL observed	PL observed (very weak from films)
Dr. Khajavikhan's homebuilt system at CREOL	532 nm laser (~500 mW)	No PL observed	PL observed (very weak from films)
Dr. McClenaghan's time-resolved system at Université Bordeaux	532 nm laser	No PL observed	Weak PL observed from films
Dr. McClenaghan's Jobin Yvon fluorometer at Université Bordeaux	Xenon lamp w/monochromator in 500-600 nm range	No PL observed	Not tested

For the CdTe QDs, various sample forms were tested, including the QD powder, 0.6 mg/mL QDs dispersed in ethanolamine, pure QDs drop-cast on a glass substrate, and spin-coated and electrosprayed films deposited from solutions having initial QD concentrations ranging from 0.06 to 0.17 mg/mL. Despite testing on the various systems listed, no PL

response was recorded. It is believed that this is due to insufficient passivation of the QDs. The degree of passivation dictates the number of defects on the QD surface that can lead to non-radiative de-excitation of the excited electron. As such, core-shell QDs tend to exhibit much higher quantum yields than QDs passivated with an organic ligand. In this case, the QDs are passivated with only an organic ligand, giving an inherently reduced quantum yield, and perhaps making them more susceptible to environmental effects like quenching due to the presence of amine solvent, either when dispersed in ethanolamine, or residual solvent in the deposited film. In the case of the core-shell CdSe/ZnS QDs tested in parallel, strong PL was observed from the QDs dispersed in ethanolamine-based solutions, shown in the following paragraph.

Figure 4.18 shows UV-vis-NIR absorption spectra of the QDs dispersed in ethanolamine, and in the $Ge_{23}Sb_7S_{70}$ solution.

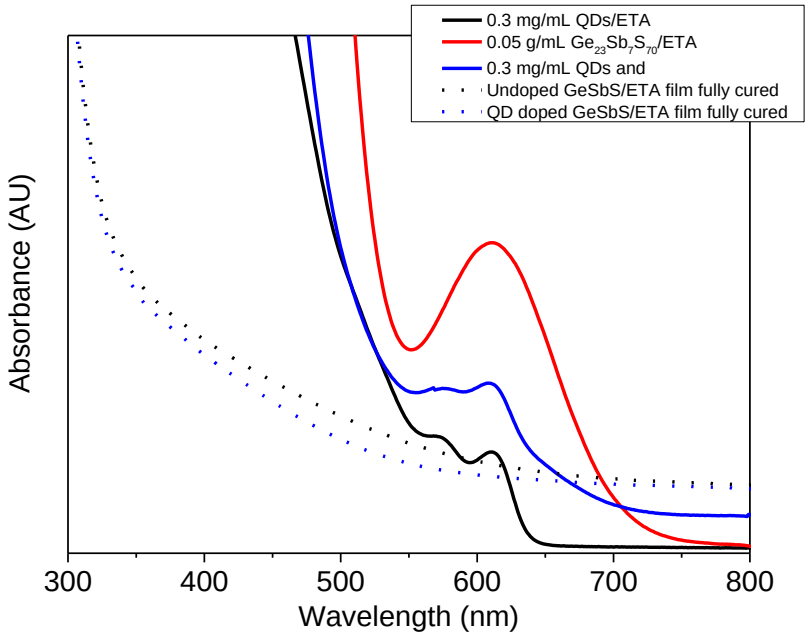

Fig. 4.18: UV-vis-NIR absorption spectra of QDs in solution and in spin-coated films

The absorption spectrum of the CdSe QDs dispersed in pure ethanolamine is very similar to that in Figure 4.14, from the manufacturer. This indicates that the QDs are likely to be well-dispersed. The shape of the spectrum is maintained for the QDs in the $Ge_{23}Sb_7S_{70}$/ethanolamine solution. This is again evidence that the dispersion of the QDs is not affected by the presence of the dissolved glass at a concentration of 0.05 g/mL. However, it is noted that the absorbance of the glass solution doped with QDs is less than the absorbance of the pure glass solution. It is believed that this is a result of oxygen exposure to the ChG solution, which has been observed to make the solutions change from a dark green to a light green color.

Figure 4.19 shows PL spectra of CdSe QDs in various forms obtained using the Ocean Optics QE Pro-FL instrument.

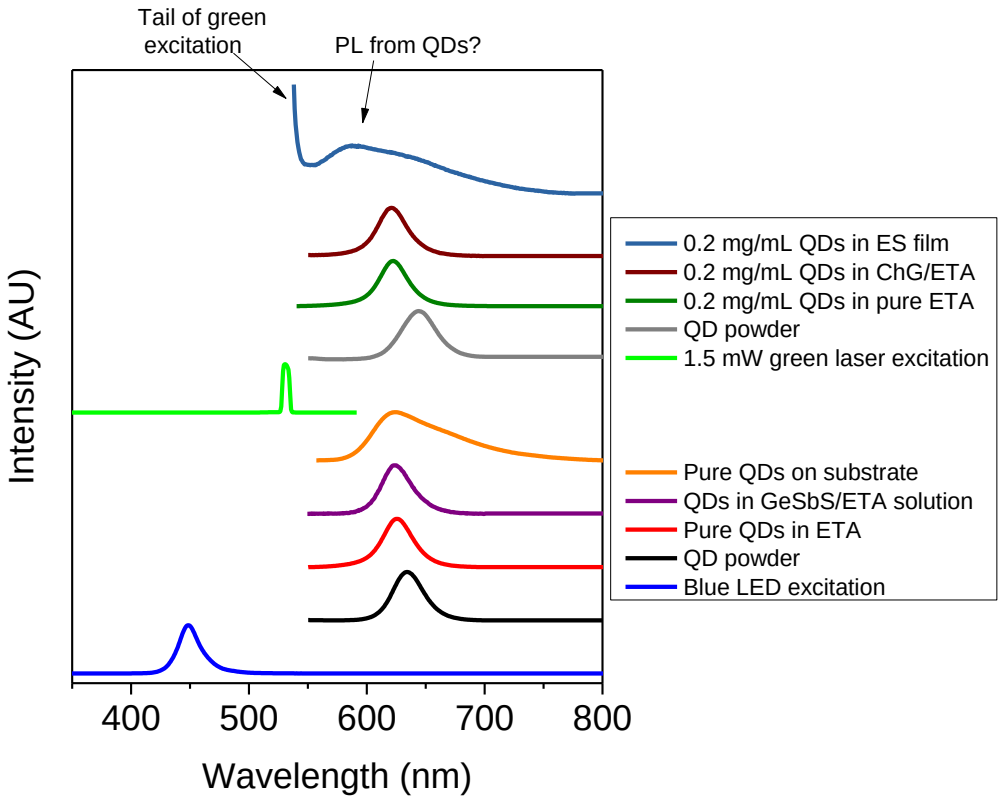

Fig. 4.19: Normalized PL spectra of CdSe QDs in various environments tested with Ocean Optics QE Pro-FL instrument using two different excitation sources

The PL spectra of these samples is very similar to the data provided by the manufacturer. In these experiments, the signal from the solutions was very strong, such that orange luminescence could be easily seen visibly when either excitation source was directed at the samples. However, in the case of the QDs in the electrosprayed film, the signal was very weak. This apparent response from the electrosprayed film looks very similar to the response of the pure QDs dropcast on a substrate. The observed blue-shift is also consistent with the previous results discussed in Section 4.1. As such, this is believed to be emission from the QDs in the film. For reference, the recorded tail of the green laser excitation at 541 nm is the same intensity as the maximum of the response from the QDs. Of course, the

recorded intensity is only indicative of how much light reaches the detector, which depends on many factors, such as the optics and geometry of the system. In the case of the QE Pro-FL system, there was a simple collimating lens to collect the light from the sample and couple it into an optical fiber which lead to the detector. This system was very useful to obtain preliminary data.

In efforts to verify the data recorded on the QE Pro-FL system, measurements were also done on a home-built system belonging to Dr. Mercedeh Khajavikhan at CREOL. This system has a few chief advantages, namely the ability to use more intense excitation, focusing optics for the luminescence, and the use of a beam splitter to filter out the excitation source. This optical component reflects wavelengths shorter than 567 nm (such as the 532 nm excitation), and transmits the PL above 567 nm. Figure 4.20 below shows the spectra recorded from this system.

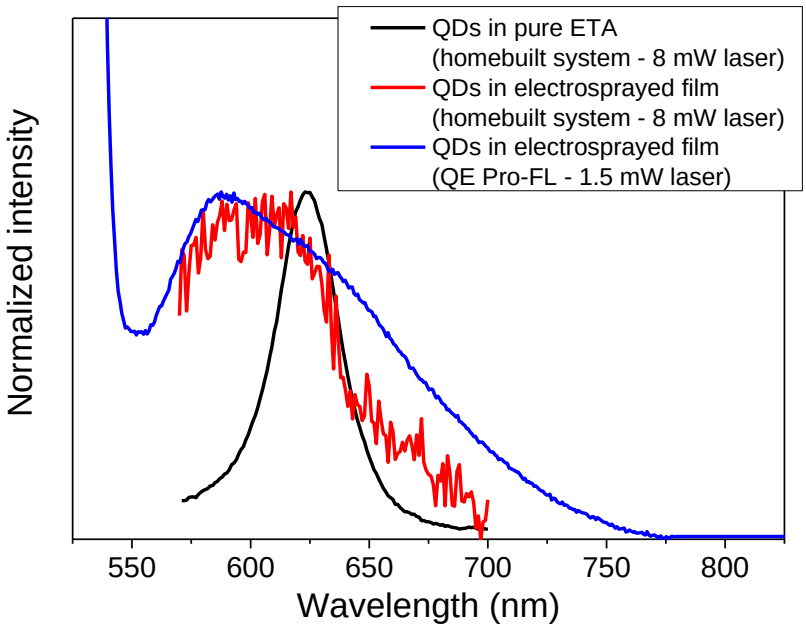

Fig. 4.20: PL spectra recorded of CdSe QDs in pure ethanolamine and in a $Ge_{23}Sb_7S_{70}$ electrosprayed film.

In Figure 4.20, the PL spectra are shown from the homebuilt system at CREOL, along with an overlay of the emission recorded from the same QD-doped electrosprayed on the QE Pro-FL. It is clear that there are some differences in the shape of the spectra, primarily that the measurement on the QE Pro-FL is centered at a shorter wavelength. This may be due partially to the tail of the excitation source adding some contribution to the intensity recorded by the QE Pro-FL. Additionally, the QE Pro-FL system shows more emission at longer wavelengths (650 to 775 nm). One difficulty with the homebuilt system is that the sample is far away from the detector (~2 m), and passes through several optical components, such as a lenses to focus the emission and a beam splitter to cut the excitation from the recorded spectrum. So, despite the high excitation power, there is also more loss of the emission on the way to the detector due to reflection losses from the multiple optical components. This is in comparison to the collimating lens and optical fiber of the QE Pro-FL system that could be placed very close to the sample. Sample alignment was also difficult on the homebuilt system in order to maximize the signal, and the result could not be repeated to obtain additional spectra for averaging and improving the signal-to-noise ratio. Based on these photoluminescence studies, strong emission from QDs dispersed in ChG/amine solution is demonstrated, but there was much difficulty recording emission from the films. The biggest contribution is likely the small interaction volume of the thin films with the excitation source.

These samples were shipped to Dr. Nathan McClenaghan in Bordeaux to further confirm the steady-state emission spectra (shown in Figure 4.21) as well as to take luminescence lifetimes (shown in Figure 4.21 and Table 4.3). Samples were prepared using both electrospraying and drop-casting, in order to test the effect of different drying kinetics on the luminescent behavior of the QDs. Two working distance were also tested in order to investigate the effect of the amount of drying prior to arrival at the substrate.

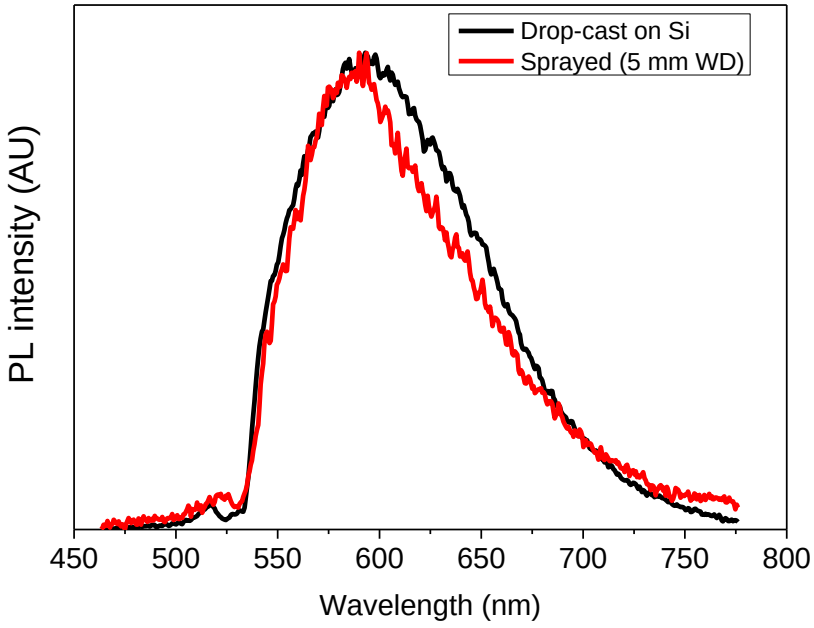

Fig. 4.21: Steady-state photoluminescence spectra with 532 nm excitation of drop-cast and electrosprayed ChG films made from solutions containing 0.2 mg/mL CdSe/ZnS QDs and 0.05 g/mL $Ge_{23}Sb_7S_{70}$.

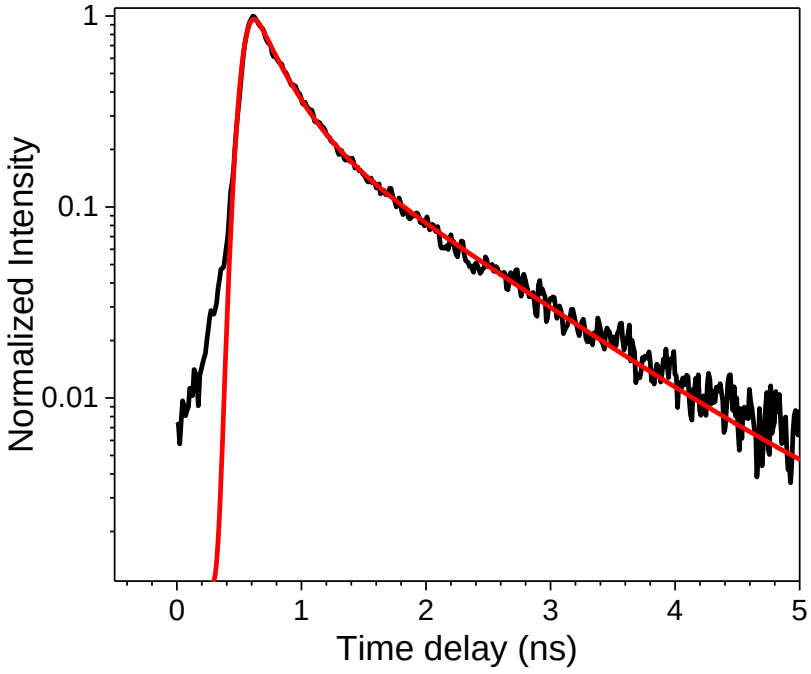

Fig. 4.22: Sample decay of QD-doped electrosprayed film (black) with two exponential fit (red)

Table 4.3: Photoluminescence decay (532 nm excitation) and fitting parameters of QD-doped sample. It is believed that there is a significant difference between the dropcast and electrosprayed samples, but not between the two electrosprayed samples due to error in the measurement

	Dropcast	Electrosprayed (10 mm WD)	Electrosprayed (5 mm WD)
τ_1	0.3	0.2	0.2
Weight 1	30%	40%	40%
τ_2	1.5	0.9	1
Weight 2	70%	60%	60%
Average lifetime (ns)	**1.14**	**0.62**	**0.68**

The steady-state spectra are centered at ~600 nm, consistent with the measurements from the other two systems. The lifetime data implies that the efficiency of the luminescence is higher in the dropcast film than the electrosprayed film. This contradicts the hypothesis that electrospray allows a more viable on-chip light source than other methods due to the quicker drying kinetics. However, it is not known what is the effect of the electric field on the QDs. It is perhaps possible that electrospray could lead to better dispersion of nanostructures due to quicker drying kinetics, and that the high electric field causes a reduction in the efficiency of the emission by producing defects in the QDs.

Based on the generally weak luminescence, and scarce observation of QDs in the electrosprayed ChG material, it is possible that the QDs rarely make it into the film. For example, they could be collecting at the tip of the nozzle. Thus, it is proposed to utilize a wire inserted through the nozzle, with some distance extending past the end of the nozzle, in order to minimize the collection of QDs at the nozzle tip. Comparison of TEM and PL of samples made with this method would indicate whether or not this enables higher QD loading in the deposited material.

Data summary:

In Chapter 4, it is demonstrated that luminescence from QDs in solution-derived ChG films is possible. However, there are some general issues with efficiency of the luminescence. This is evidenced by the reduced luminescence lifetime of the QDs when in the spin-coated film, as compared to the QDs in the pure chloroform solvent. Aggregation of QDs was observed in this sample under TEM. Thus, two methods of improving

dispersion were studied: optimizing the surface chemistry of the QDs, and exploring the use of electrospray as an alternative deposition process. Two organic capping agents were found to allow the dispersion of QDs in a $Ge_{23}Sb_7S_{70}$/ethanolamine solution, including mercaptopropionic acid, and octadecylamine. Both QDs were incorporated into spin-coated and electrosprayed films, where indication was found that electrospray may be more suitable for nanoparticle incorporation. QD incorporation into electrosprayed films was based on an initial droplet size analysis from TEM combined with EELS, and found to be around 174 nm. With this small droplet size, there is potential to incorporate a high concentration of dispersed QDs. The luminescence data demonstrates the ability to fabricate a luminescent, QD-doped ChG film. Contrary to the expected result, the electrosprayed films exhibit less-efficient luminescence than the slow-drying dropcast film.

V. CONCLUSIONS

Upon completion of this author's MS degree, the original, primary goal of this dissertation was defined, as to how nanoparticle dispersion could be improved in solution-derived chalcogenide glass (ChG) films. It was believed that the aggregation mechanism limiting good dispersion in the spin-coating processes occurred primarily due to the thermodynamic driving force of aggregation and the kinetics of solvent evaporation. Strategies to examine the role of these two processes in the creation of optical quality infrared transparent glass films formed the basis of this PhD dissertation.

A key component needed to improve dispersion and study these effects was QDs with surface chemistry optimized for solutions of chalcogenide glass dissolved in amine solvents was established. Two different surface chemistries were found to allow sufficiently high dispersion, mercaptopropionic acid and octadecylamine. In addition, electrospray was investigated due to suspected advantages with regards to QD dispersion. In parallel to the dispersion studies, the other unique advantages of electrospray were explored, namely the possibility of GRIN coatings. Based on these ideas, the goals of this dissertation was further refined to:

- Explore the fabrication of gradient refractive index (GRIN) coatings through the flexibility of the electrospray process
- Understand how the degree of QD dispersion varies with film deposition method (spin-coating vs. electrospray) and with the processing parameters used in each method

- Characterize the resulting luminescent properties of QD-doped ChG films

The first step was to develop blanket ChG film deposition by electrospray. In these experiments, it was found that low vapor pressure, higher viscosity solutions, namely $Ge_{23}Sb_7S_{70}$ and As_2S_3 dissolved in ethanolamine, result in a more stable spray. As this solvent has not been studied in much detail previously for ChG film deposition, optimization of solvent removal was necessary. A method of obtaining uniform thickness films over large areas was also demonstrated by utilizing a serpentine path of the spray over the substrate. These results are significant because they represent a simple approach to optical quality, uniform thickness ChG films using a solution-based approach compatible with roll-to-roll processing.

Effective GRIN films were also demonstrated by depositing non-uniform thickness layers of $Ge_{23}Sb_7S_{70}$. These samples were demonstrated to have a gradient in composition and uniform thickness over a range of about 3 mm. Based on the expected volume of each layer, and the measured refractive index of the individual films, a linear change in refractive index from 2.15 to 2.4 was predicted over the 3 mm range. The interface between the two layers was found to be very smooth. Through compositional mapping, a gradual change in the composition from $Ge_{23}Sb_7S_{70}$ at the bottom, to As_2S_3 at the top, was observed. This is likely due to redissolution of the first layer by the wet deposition of droplets from the second layer. Because this film lacks a sharp interface, Fresnel loss is not expected, it is conceivable to use such a film in a device as either a GRIN coating to tune the resonant wavelength of an array of resonators, or even to fabricate an array of resonators with

different refractive indices from the GRIN film itself. Finally, it may be possible to generate an anti-reflective layer based on this multilayer approach, due to the gradual change in composition from the bottom to the top of the film. Based on these results, the first goal of this dissertation was accomplished.

The next two goals were to compare the dispersion of QDs in solution-derived ChG films, and the resulting photoluminescence behavior. The first step in this process was to understand the initial droplet size during electrospray. This was done for one solution at one flow rate (0.05 g/mL $Ge_{23}Sb_7S_{70}$/ethanolamine at 10 μL/hr). A method of analyzing the cured volume of sprayed droplets on a TEM grid was developed, by spraying for a short duration and then imaging the diameter of the droplets, as well as estimating their thickness using EELS. This approach can be utilized to optimize ChG droplet size for any application. It was difficult to image and characterize the dispersion of QDs in a ChG film matrix, which is suspected to be due mainly to the small size of the QDs, and lack of contrast between the two phases. However, individual QDs were found with a short distance between them in an electrosprayed ChG sample, demonstrating that this approach does have some potential for nanoparticle dispersion. Therefore, the second goal of this dissertation was partially successful. The third goal was also partially successful, as luminescence was observed from the QD doped solutions and films made by spin-coating and electrospray. Thus far, the preliminary luminescence lifetime data suggests that electrospray results in a less-efficient light source, though it is unknown if this is an effect of QD dispersion or something else, such as the high applied electric field causing a reduction in emission efficiency.

The findings of this thesis have contributed to the know-how required to continue the evolution of novel materials for infrared optical applications. Specifically, these findings will enable further work to exploit the use of infrared glass films in a wide range of microphotonic applications where small scale (2- or 3-D printing) or larger scale (roll-to-roll) fabrication strategies are required. This work has shown that electrospray (ES) is a robust processing route amenable to fabrication of active or passive glass films with tailorable properties and refractive index profiles. An explanation of the ES process parameters and their correlation to resulting film quality has been made which will extend the use of compositionally tailorable properties of glass films in planar photonic systems.

VI. FUTURE WORK

Future work is suggested in all areas in this dissertation. One remaining issue is stability of the spray, which seems to be caused by wetting of the solution up the nozzle and leads to isolated roughness of the films. It is proposed that a nozzle coated with a chemically resistant, hydrophobic layer, such as polytetrafluorethylene, would minimize wetting of the nozzle, perhaps even allowing solvents such as propylamine and ethylenediamine to be used. These solvents have been studied in more detail, and it is possible that they can be removed to a further degree from the film during annealing due to their lower boiling point. In addition, a multiplexed nozzle array could be used to increase throughput and make the process more suitable for scale-up. This has been demonstrated with other solutions. A linear array could be tested first, with spacing of a few mm between each nozzle. The angle between the linear array and the direction of the spray nozzle could be varied in order to possibly find a spacing that would result in direct deposition of uniform thickness films without a serpentine path.

In the case of GRIN films, it would be very interesting to attempt simultaneous spray of two compositions in order to fabricate a true GRIN coating. This could be done by spraying both solutions with a positive voltage, or spraying one solution with a positive voltage, and the other with a negative voltage. Using one positive and one negative voltage would be particularly interesting because the droplets of each solution would be oppositely charged, and they would therefore be attracted together due to electrostatic attraction. Both situations would require the purchase of some additional equipment, primarily another DC power supply and syringe pump.

For QD-doped films, it is suggested to do a more comprehensive study of the luminescent lifetimes of various concentrations of QDs in electrosprayed and spin-coated films to investigate the observation of shorter lifetimes for the electrosprayed films than dropcast films. This also should help to extract conclusions about the microscopic dispersion of the QDs from their macroscopic properties. In addition, experiments are suggested to deconvolve the effects of dispersion and matrix (surrounding refractive index) on the lifetime of the QDs. However, the first step is to be able to characterize the dispersion of the QDs, which is difficult due to minimal contrast difficult between the QDs and the surrounding matrix. Therefore, it is proposed to study the incorporation of metallic nanoparticles, such as Au, with something like octadecylamine or mercaptopropionic acid surface chemistry, allowing them to disperse in an amine solvent. Using a metal such as Au, with a density of 19.3 g/cm^3, would allow better contrast between the nanoparticles and the surrounding matrix. It would also be beneficial to use larger nanoparticles than the ~5 nm QDs in this dissertation. Finally, the issue of the very low quantity of QDs in the deposited electrosprayed films is suggested to be addressed by utilizing a wire extending through the nozzle center, as discussed in Chapter 4.

REFERENCES

1. V. Singh, T. L. Pao, N. Patel, H. Lin, L. Li, Y. Zou, F. Deng, C. Ni, J. Hu, J. Giammarco, A. P. Soliani, B. Zdyrko, I. Luzinov, S. Novak, J. Novak, P. Wachtel, S. Danto, J. D. Musgraves, K. Richardson, L. C. Kimerling and A. M. Agarwal, 'Mid-infrared materials and devices on a Si platform for optical sensing,' *Science and Technology of Advanced Materials*, 15 [1] 014603 (15 pp.) (2014).

2. J. D. Kenyon, 'Forbidden science: from ancient technologies to free energy,' *Bear and Company* (2010).

3. D. C. Lingberg, 'Theories of vision from Al-Kindi to Kepler,' *University of Chicago Press* 12 (1976).

4. T. P. Pearsall, 'Photonics essentials,' *McGraw-Hill* (2010).

5. http://manufacturing.gov/ip-imi.html, 2015 [September 14] 1.

6. T. L. Pao, V. Singh, L. Kimerling and A. Murthy Agarwal, 'Planar silicon nitride mid-infrared devices,' *Appl. Phys. Lett.*, 102 [25] 251121 (5 pp.) (2013).

7. J. Hu, V. Tarasov, N. Carlie, L. Petit, A. Agarwal, K. Richardson and L. Kimerling, 'Exploration of waveguide fabrication from thermally evaporated Ge-Sb-S glass films,' *Optical Materials*, 30 [10] 1560-1566 (2008).

8. J. D. Musgraves, N. Carlie, J. Hu, L. Petit, A. Agarwal, L. C. Kimerling and K. A. Richardson, 'Comparison of the optical, thermal and structural properties of Ge-Sb-S thin films deposited using thermal evaporation and pulsed laser deposition techniques,' *Acta Materialia*, 59 [12] 5032-5039 (2011).

9. H. Lin, L. Li, Y. Zou, S. Danto, J. D. Musgraves, K. Richardson, S. Kozacik, M. Murakowski, D. Prather, P. T. Lin, V. Singh, A. Agarwal, L. C. Kimerling and J. Hu, 'Demonstration of high-Q mid-infrared chalcogenide glass-on-silicon resonators,' *Opt. Lett.*, 38 [9] 1470-2 (2013).

10. N. Carlie, J. D. Musgraves, B. Zdyrko, I. Luzinov, J. Hu, V. Singh, A. Agarwal, L. C. Kimerling, A. Canciamilla, F. Morichetti, A. Melloni and K. Richardson, 'Integrated chalcogenide waveguide resonators for mid-IR sensing: Leveraging material properties to meet fabrication challenges,' *Optics Express*, 18 [25] 26728-26743 (2010).

11. J. Janata, 'Principles of chemical sensors,' *Springer* (2009).

12. C. McDonagh, C. S. Burke and B. D. MacCraith, 'Optical chemical sensors,' *Chem. Rev.*, 108 [2] 400-422 (2008).

13. E. J. Park, K. R. Reid, W. Tang, R. T. Kennedy and R. Kopelman, 'Ratiometric fiber optic sensors for the detection of inter- and intra-cellular dissolved oxygen,' *Journal of Materials Chemistry*, 15 [27-28] 2913-2919 (2005).

14. L. C. Kimerling, 'Silicon microphotonics,' *Appl. Surf. Sci.*, 159–160 [0] 8-13 (2000).

15. H. Wong, V. Filip, C. K. Wong and P. S. Chung, 'Silicon integrated photonics begins to revolutionize,' *Microelectronics Reliability*, 47 [1] 1-10 (2007).

16. J. D. B. Bradley, E. S. Hosseini, Purnawirman, Z. Su, T. N. Adam, G. Leake, D. Coolbaugh and M. R. Watts, 'Monolithic erbium- and ytterbium-doped microring lasers on silicon chips,' *Optics Express*, 22 [10] 12226-12237 (2014).

17. C. Tsay, F. Toor, C. F. Gmachl and C. B. Arnold, 'Chalcogenide glass waveguides integrated with quantum cascade lasers for on-chip mid-IR photonic circuits,' *Opt. Lett.*, 35 [20] 3324-3326 (2010).

18. E. H. Cho, B. Kim, S. Jun, J. Lee, D. H. Park, K. Lee, J. Kim, J. Kim and J. Joo, 'Remote biosensing with polychromatic optical waveguide using blue light-emitting organic nanowires hybridized with quantum dots,' *Advanced Functional Materials*, 24 [24] 3684-3691 (2014).

19. M. Muneeb, X. Chen, P. Verheyen, G. Lepage, S. Pathak, E. Ryckeboer, A. Malik, B. Kuyken, M. Nedeljkovic, J. Van Campenhout, G. Z. Mashanovich and G. Roelkens, 'Demonstration of Silicon-on-insulator mid-infrared spectrometers operating at 3.8m,' *Optics Express*, 21 [10] 11659-11669 (2013).

20. C. Reimer, M. Nedeljkovic, D. J. M. Stothard, M. O. S. Esnault, C. Reardon, L. O'Faolain, M. Dunn, G. Z. Mashanovich and T. F. Krauss, 'Mid-infrared photonic crystal waveguides in silicon,' *Optics Express*, 20 [28] 29361-29368 (2012).

21. A. Rickman, 'The commercialization of silicon photonics,' *Nature Photonics*, 8 [8] 579-582 (2014).

22. Z. Cheng, X. Chen, C. Y. Wong, K. Xu, C. K. Y. Fung, Y. M. Chen and H. K. Tsang, 'Focusing subwavelength grating coupler for mid-infrared suspended membrane waveguide,' *Opt. Lett.*, 37 [7] 1217-1219 (2012).

23. R. Shankar, I. Bulu and M. Loncar, 'Integrated high-quality factor silicon-on-sapphire ring resonators for the mid-infrared,' *Appl. Phys. Lett.*, 102 [5] 051108 (3 pp.) (2013).

24. T. Baehr-Jones, A. Spott, R. Ilic, A. Spott, B. Penkov, W. Asher and M. Hochberg, 'Silicon-on-sapphire integrated waveguides for the mid-infrared,' *Optics Express*, 18 [12] 12127-35 (2010).

25. G. Z. Mashanovich, M. M. Milosevic, M. Nedeljkovic, N. Owens, B. Xiong, J. T. Ee and Y. Hu, 'Low loss silicon waveguides for the mid-infrared,' *Optics Express*, 19 [8] 7112-19 (2011).

26. X. Wang, S. Kim, s. l. Ro[German, M. Jetter, P. Michler and B. Mizaikoff, 'Ultra-sensitive mid-infrared evanescent field sensors combining thin-film strip waveguides with quantum cascade lasers,' *Analyst*, 137 [10] 2322-2327 (2012).

27. C. Charlton, M. Giovannini, J. Faist and B. Mizaikoff, 'Fabrication and characterization of molecular beam epitaxy grown thin-film GaAs waveguides for mid-infrared evanescent field chemical sensing,' *Anal. Chem.*, 78 [12] 4224-4227 (2006).

28. T. Lewi and A. Katzir, 'Silver halide single-mode strip waveguides for the mid-infrared,' *Opt. Lett.*, 37 [13] 2733-2735 (2012).

29. S. Khan, J. Chiles, J. Ma and S. Fathpour, 'Silicon-on-nitride waveguides for mid- and near-infrared integrated photonics,' *Appl. Phys. Lett.*, 102 [12] (2013).

30. J. E. Shelby, 'Introduction ot glass science and technology'. The Royal Society of Chemistry, Cambridge, UK, 2005.

31. B. J. Eggleton, B. Luther-Davies and K. Richardson, 'Chalcogenide photonics,' *Nature Photonics*, 5 [3] 141-8 (2011).

32. J. S. Sanghera, L. B. Shaw, L. E. Busse, V. Q. Nguyen, P. C. Pureza, B. C. Cole, B. B. Harbison, I. D. Aggarwal, R. Mossadegh, F. Kung, D. Talley, D. Roselle and R. Miklos, 'Development and infrared applications of chalcogenide glass optical fibers,' *Fiber and Integrated Optics*, 19 [3] 251-274 (2000).

33. G. Tao, S. Shabahang, H. Ren, F. Khalilzadeh-Rezaie, R. E. Peale, Z. Yang, X. Wang and A. F. Abouraddy, 'Robust multimaterial tellurium-based chalcogenide glass fibers for mid-wave and long-wave infrared transmission,' *Opt. Lett.*, 39 [13] 4009-4012 (2014).

34. S. Danto, M. Dubernet, B. Giroire, J. D. Musgraves, P. Wachtel, T. Hawkins, J. Ballato and K. Richardson, 'Correlation between native As2Se3 preform purity and glass optical fiber mechanical strength,' *Mater. Res. Bull.*, 49 [1] 250-258 (2014).

35. J. S. Sanghera, I. D. Aggarwal, L. E. Busse, P. C. Pureza, V. Q. Nguyen, F. H. Kung, L. B. Shaw and F. Chenard, 'Chalcogenide optical fibers target mid-IR applications,' *Laser Focus World*, 41 [4] 83-87 (2005).

36. R. Stegeman, G. Stegeman, P. Delfyett J., L. Petit, N. Carlie, K. Richardson and M. Couzi, 'Raman gain measurements and photo-induced transmission effects of germanium- and arsenic-based chalcogenide glasses,' *Optics Express*, 14 [24] (2006).

37. J. S. Sanghera, L. B. Shaw, P. Pureza, V. Q. Nguyen, D. Gibson, L. Busse, I. D. Aggarwal, C. M. Florea and F. H. Kung, 'Nonlinear Properties of Chalcogenide Glass Fibers,' *International Journal of Applied Glass Science*, 1 [3] 296-308 (2010).

38. L. Sojka, Z. Tang, D. Furniss, H. Sakr, A. Oladeji, E. Beres-Pawlik, H. Dantanarayana, E. Faber, A. B. Seddon, T. M. Benson and S. Sujecki, 'Broadband, mid-infrared emission from Pr3+ doped GeAsGaSe chalcogenide fiber, optically clad,' *Optical Materials*, 36 [6] 1076-1082 (2014).

39. Y. Zheng, Y. Zhou, X. Yu, Y. Qi, S. Peng, L. Wu and F. Yang, 'Performance of Er3+-doped chalcogenide glass MOF amplifier applied for 1.53 m band,' *Optoelectronics Letters*, 10 [3] 184-187 (2014).

40. X. Niu, P. Zhang, Y. Zhou, W. Zhang, X. Wang, X. Shen, C. Lin, Y. Xu, Y. Wu and S. Dai, 'Modeling and simulation of mid-IR amplifying characteristics of Tm3+-doped chalcogenide Photonic Crystal Fibers,' *Infrared Phys. Technol.*, 63 178-83 (2014).

41. P. Ma, D. Choi, Y. Yu, X. Gai, Z. Yang, S. Debbarma, S. Madden and B. Luther-Davies, 'Low-loss chalcogenide waveguides for chemical sensing in the mid-infrared,' *Optics Express*, 21 [24] 29927-29937 (2013).

42. Y. Zou, L. Moreel, H. Lin, J. Zhou, L. Li, S. Danto, J. D. Musgraves, E. Koontz, K. Richardson, K. D. Dobson, R. Birkmire and J. Hu, 'Solution Processing and Resist-Free Nanoimprint Fabrication of Thin Film Chalcogenide Glass Devices: Inorganic-Organic Hybrid Photonic Integration,' *Advanced Optical Materials*, 2 [8] 759-64 (2014).

43. J. Novak, S. Novak, M. Dussauze, E. Fargin, F. Adamietz, J. D. Musgraves and K. Richardson, 'Evolution of the structure and properties of solution-based Ge23Sb7S70 thin films during heat treatment,' *Mater. Res. Bull.*, 48 [3] 1250-5 (2013).

44. Y. Zou, H. Lin, O. Ogbuu, L. Li, S. Danto, S. Novak, J. Novak, J. D. Musgraves, K. Richardson and J. Hu, 'Effect of annealing conditions on the physio-chemical properties of spin-coated As2Se3 chalcogenide glass films,' *Optical Materials Express*, 2 [12] 1723-1732 (2012).

45. C. Tsay, Y. Zha and C. B. Arnold, 'Solution-processed chalcogenide glass for integrated single-mode mid-infrared waveguides,' *Optics Express*, 18 [25] 26744-53 (2010).

46. L. Petit, N. Carlie, F. Adamietz, M. Couzi, V. Rodriguez and K. C. Richardson, 'Correlation between physical, optical and structural properties of sulfide glasses in the system Ge-Sb-S,' *Mater. Chem. Phys.*, 97 [1] 64-70 (2006).

47. J. Chiles, M. Malinowski, A. Rao, S. Novak, K. Richardson and S. Fathpour, 'Low-loss, submicron chalcogenide integrated photonics with chlorine plasma etching,' *Appl. Phys. Lett.*, 106 [11] (2015).

48. N. Carlie, N. C. Anheier J., H. A. Qiao, B. Bernacki, M. C. Phillips, L. Petit, J. D. Musgraves and K. Richardson, 'Measurement of the refractive index dispersion of As2Se3 bulk glass and thin films prior to and after laser irradiation and annealing using prism coupling in the near- and mid-infrared spectral range,' *Rev. Sci. Instrum.*, 82 [5] 053103 (7 pp.) (2011).

49. D. Bera, L. Qian, T. Tseng and P. H. Holloway, 'Quantum dots and their multimodal applications: A review,' *Materials*, 3 [4] 2260-2345 (2010).

50. S. Horikoshi and N. Serpone, 'Microwaves in nanoparticle synthesis: fundamentals and applications'. Wiley 2013.

51. M. Daniel and D. Astruc, 'Gold Nanoparticles: Assembly, Supramolecular Chemistry, Quantum-Size-Related Properties, and Applications Toward Biology, Catalysis, and Nanotechnology,' *Chem. Rev.*, 104 [1] 293-346 (2004).

52. T. Trindade, O. O'Brien and N. L. Pickett, 'Nanocrystalline semiconductors: synthesis, properties, and perspectives,' *Chemistry of Materials*, 13 [11] 3843-58 (2001).

53. S. Novak, 'Nanoparticles in solution-derived chalcogenide glass films,' *MS Thesis, Clemson University* (2012).

54. A. I. Ekimov, A. L. Efros and A. A. Onushchenko, 'Quantum size effect in semiconductor microcrystals,' *Solid State Commun.*, 56 [11] 921-4 (1985).

55. C. Woodford, 'What are quantum dots?' *www. explainthatstuff. com*, 2015 [1/7] 1 (2014).

56. R. Rossetti, S. Nakahara and L. E. Brus, 'Quantum size effects in the redox potentials, resonance Raman spectra, and electronic spectra of CdS crystallites in aqueous solution,' *J. Chem. Phys.*, 79 [2] 1086-8 (1983).

57. R. Rossetti, J. L. Ellison, J. M. Gibson and L. E. Brus, 'Size effects in the excited electronic states of small colloidal CdS crystallites,' *J. Chem. Phys.*, 80 [9] 4464-9 (1984).

58. W. W. Yu, L. Qu, W. Guo and X. Peng, 'Experimental determination of the extinction coefficient of CdTe, CdSe, and CdS nanocrystals,' *Chemistry of Materials*, 15 [14] 2854-2860 (2003).

59. I. Moreels, K. Lambert, D. Smeets, D. De Muynck, T. Nollet, J. C. Martins, F. Vanhaecke, A. Vantomme, C. Delerue, G. Allan and Z. Hens, 'Size-dependent optical properties of colloidal PbS quantum dots,' *ACS Nano*, 3 [10] 3023-3030 (2009).

60. J. M. Harbold and F. W. Wise, 'Photoluminescence spectroscopy of PbSe nanocrystals,' *Physical Review B (Condensed Matter and Materials Physics)*, 76 [12] 1-6 (2007).

61. J. E. Murphy, M. C. Beard, A. G. Norman, S. P. Ahrenkiel, J. C. Johnson, P. Yu, O. I. Micic, R. J. Ellingson and A. J. Nozik, 'PbTe colloidal nanocrystals: Synthesis, characterization, and multiple exciton generation,' *J. Am. Chem. Soc.*, 128 [10] 3241-3247 (2006).

62. J. M. Pietryga, R. D. Schaller, D. Werder, M. H. Stewart, V. I. Klimov and J. A. Hollingsworth, 'Pushing the band gap envelope: Mid-infrared emitting colloidal PbSe quantum dots,' *J. Am. Chem. Soc.*, 126 [38] 11752-11753 (2004).

63. P. A. Loiko, G. E. Rachkovskaya, G. B. Zacharevich, V. S. Gurin, M. S. Gaponenko and K. V. Yumashev, 'Optical properties of novel PbS and PbSe quantum-dot-doped alumino-alkali-silicate glasses,' *J. Non Cryst. Solids*, 358 [15] 1840-1845 (2012).

64. R. S. Silva, O. Baffa, F. Chen, S. A. Lourenco and N. O. Dantas, 'Luminescence in semimagnetic Pb1-xMnxSe quantum dots grown in a glass host: Radiative and nonradiative emission processes,' *Chemical Physics Letters*, 567 23-6 (2013).

65. S. El-Rabaie, T. A. Taha and A. A. Higazy, 'Characterization and growth of lead telluride quantum dots doped novel fluorogermanate glass matrix,' *Materials Science in Semiconductor Processing*, 30 631-635 (2015).

66. S. El-Rabaie, T. A. Taha and A. A. Higazy, 'PbTe quantum dots formation in a novel germanate glass,' *J. Alloys Compounds*, 594 102-106 (2014).

67. F. Pang, X. Sun, H. Guo, J. Yan, J. Wang, X. Zeng, Z. Chen and T. Wang, 'A PbS quantum dots fiber amplifier excited by evanescent wave,' *Optics Express*, 18 [13] 14024-30 (2010).

68. C. Liu, Y. K. Kwon and J. Heo, 'Absorption and photoluminescence of PbS QDs in glasses,' *J. Non Cryst. Solids*, 355 [37-42] 1880-1883 (2009).

69. A. M. Malyarevich, K. V. Yumashev and A. A. Lipovskii, 'Semiconductor-doped glass saturable absorbers for near-infrared solid-state lasers,' *J. Appl. Phys.*, 103 [8] 081301-1 (2008).

70. K. Wundke, S. Pötting, J. Auxier, A. Schülzgen, N. Peyghambarian and N. F. Borrelli, 'PbS quantum-dot-doped glasses for ultrashort-pulse generation,' *Appl. Phys. Lett.*, 76 [1] 10-12 (2000).

71. P. Bajaj, E. Woodruff and J. T. Moore, 'Synthesis of PbSe/SiO2 and PbTe/SiO2 nanocomposites using the sol-gel process,' *Mater. Chem. Phys.*, 123 [2-3] 581-584 (2010).

72. A. Sashchiuk, E. Lifshitz, R. Reisfeld, T. Saraidarov, M. Zelner and A. Willenz, 'Optical and conductivity properties of PbS nanocrystals in amorphous zirconia sol-gel films,' *J. Sol Gel Sci. Technol.*, 24 [1] 31-38 (2002).

73. A. Martucci, P. Innocenzi, J. Fick and J. D. Mackenzie, 'Zirconia-ormosil films doped with PbS quantum dots,' *J. Non Cryst. Solids*, 244 [1] 55-62 (1999).

74. N. N. Parvathy, A. V. Rao and G. M. Pajonk, 'Effects of temperature and sol-gel parameters on PbS crystallite sizes and their spectral and physical properties in a porous silica matrix,' *J. Non Cryst. Solids*, 241 [2-3] 79-90 (1998).

75. M. V. Kovalenko, R. D. Schaller, D. Jarzab, M. A. Loi and D. V. Talapin, 'Inorganically functionalized PbS-CdS colloidal nanocrystals: Integration into amorphous chalcogenide glass and luminescent properties,' *J. Am. Chem. Soc.*, 134 [5] 2457-2460 (2012).

76. S. Novak, L. Scarpantonio, J. Novak, M. Dai Pre, A. Martucci, J. D. Musgraves, N. D. McClenaghan and K. Richardson, 'Incorporation of luminescent CdSe/ZnS core-shell quantum dots and PbS quantum dots into solution-derived chalcogenide glass films,' *Optical Materials Express*, 3 [6] 729-738 (2013).

77. C. Lu, J. M. P. Almeida, N. Yao and C. Arnold, 'Fabrication of uniformly dispersed nanoparticle-doped chalcogenide glass,' *Appl. Phys. Lett.*, 105 [26] (2015).

78. E. A. Fagen and H. Fritzsche, 'Electrical conductivity of amorphous chalcogenide alloy films,' *J. Non Cryst. Solids*, 2 170-9 (1970).

79. M. Yamashita, H. Yamanaka and H. Wakabayashi, 'Thin-film preparation of the Li2S□GeS2□Ga2S3 glass system by sputtering,' *Solid State Ionics*, 89 [3–4] 299-304 (1996).

80. G. C. Chern and I. Lauks, 'Spin-coated amorphous chalcogenide films,' *J. Appl. Phys.*, 53 [10] 6979-82 (1982).

81. J. Xu and R. M. Almeida, 'Preparation and characterization of germanium sulfide based sol-gel planar waveguides,' *J. Sol Gel Sci. Technol.*, 19 [1-3] 243-248 (2000).

82. Y. Zha, M. Waldmann and C. B. Arnold, 'A review on solution processing of chalcogenide glasses for optical components,' *Optical Materials Express*, 3 [9] 1259-1272 (2013).

83. M. Waldmann, J. D. Musgraves, K. Richardson and C. B. Arnold, 'Structural properties of solution processed Ge23Sb 7S70 glass materials,' *Journal of Materials Chemistry*, 22 [34] 17848-17852 (2012).

84. S. Song, N. Carlie, J. Boudies, L. Petit, K. Richardson and C. B. Arnold, 'Spin-coating of Ge23Sb7S70 chalcogenide glass thin films,' *J. Non Cryst. Solids*, 355 [45-47] 2272-8 (2009).

85. J. Zeleny, 'Instability of electrified liquid surfaces,' *Physical Review*, 10 1-6 (1917).

86. M. Cloupeau and B. Prunet-Foch, 'Electrohydrodynamic spraying functioning modes: A critical review,' *J. Aerosol Sci.*, 25 [6] 1021-1036 (1994).

87. G. Taylor, 'Disintegration of water drops in an electric field,' *Proc. Royal Soc. London*, 280 383 (1964).

88. W. Deng, J. F. Klemic, X. Li, M. A. Reed and A. Gomez, 'Increase of electrospray throughput using multiplexed microfabricated sources for the scalable generation of monodisperse droplets,' *J. Aerosol Sci.*, 37 [6] 696-714 (2006).

89. A. Jaworek, 'Electrospray droplet sources for thin film deposition,' *J. Mater. Sci.*, 42 [1] 266-97 (2007).

90. J. Fenn, 'Electrospray wings for nanoscale elephants,', 1 1 (2006).

91. D. J. Carswell and J. Milsted, 'New method for preparation of thin films of radioactive material,' *Journal of Nuclear Energy*, 4 [1] 51-54 (1957).

92. X. Zhao, X. Wang, S. L. Lim, D. Qi, R. Wang, Z. Gao, B. Mi, Z. Chen, W. Huang and W. Deng, 'Enhancement of the performance of organic solar cells by electrospray deposition with optimal solvent system,' *Solar Energy Mater. Solar Cells*, 121 119-125 (2014).

93. T. Zhu, C. Li, W. Yang, X. Zhao, X. Wang, C. Tang, B. Mi, Z. Gao, W. Huang and W. Deng, 'Electrospray dense suspensions of TiO2 nanoparticles for dye sensitized solar cells,' *Aerosol Science and Technology*, 47 [12] 1302-1309 (2013).

94. J. S. Sanghera and I. D. Aggarwal, 'Active and passive chalcogenide glass optical fibers for IR applications: a review,' *J. Non Cryst. Solids*, 256–257 [0] 6-16 (1999).

95. T. Cardinal, K. A. Richardson, H. Shim, A. Schulte, R. Beatty, K. Le Foulgoc, C. Meneghini, J. F. Viens and A. Villeneuve, 'Non-linear optical properties of chalcogenide glasses in the system As-S-Se,' *J. Non Cryst. Solids*, 256 353-360 (1999).

96. '"Interferenzmikroskop Aufbau sw" by Polytec GmbH - Own work. Licensed under CC BY-SA 3.0 via Commons - https://commons.wikimedia.org/wiki/File:Interferenzmikroskop_Aufbau_sw.jpg#/media/File:Interferenzmikroskop_Aufbau_sw.jpg, 2015 [10/5].

97. Y. Zha and C. B. Arnold, 'Solution-processing of thick chalcogenidechalcogenide and metal-chalcogenide structures by spin-coating and multilayer lamination,' *Optical Materials Express*, 3 [2] 309-317 (2013).

98. J. Hu, Ning-Ning Feng, N. Carlie, L. Petit, A. Agarwal, K. Richardson and L. Kimerling, 'Optical loss reduction in high-index-contrast chalcogenide glass waveguides via thermal reflow,' *Optics Express*, 18 [2] 1469-78 (2010).

99. M. L. Trunov, P. M. Nagy, V. Takats, P. M. Lytvyn, S. Kokenyesi and E. Kalman, 'Surface morphology of as-deposited and illuminated As-Se chalcogenide thin films,' *J. Non Cryst. Solids*, 355 [37-42] 1993-1997 (2009).

100. S. Song, J. Dua and C. B. Arnold, 'Influence of annealing conditions on the optical and structural properties of spin-coated As2S3 chalcogenide glass thin films,' *Optics Express*, 18 [6] 5472-5480 (2010).

101. A. J. D'Alfonso, B. Freitag, D. Klenov and L. J. Allen, 'Atomic-resolution chemical mapping using energy-dispersive x-ray spectroscopy,' *Physical Review B (Condensed Matter and Materials Physics)*, 81 [10] 100101 (4 pp.) (2010).

102. L. J. Allen, A. J. D'Alfonso, B. Freitag and D. O. Klenov, 'Chemical mapping at atomic resolution using energy-dispersive X-ray spectroscopy,' *MRS Bull*, 37 [1] 47-52 (2012).

103. P. Thanasekaran, R. Liao, B. Manimaran, Y. Liu, P. Chou, S. Rajagopal and K. Lu, 'Photoluminescence electron-transfer quenching of rhenium(I) rectangles with amines,' *Journal of Physical Chemistry A*, 110 [37] 10683-10689 (2006).

104. R. E. Muenchausen, L. G. Jacobsohn, B. L. Bennett, E. A. McKigney, J. F. Smith and D. W. Cooke, 'A novel method for extracting oscillator strength of select rare-earth ion optical transitions in nanostructured dielectric materials,' *Solid State Commun.*, 139 [10] 497-500 (2006).

105. D. W. Cooke, J. -. Lee, B. L. Bennett, J. R. Groves, L. G. Jacobsohn, E. A. McKigney, R. E. Muenchausen, M. Nastasi, K. E. Sickafus, M. Tang, J. A. Valdez, J. -.

Kim and K. S. Hong, 'Luminescent properties and reduced dimensional behavior of hydrothermally prepared Y2SiO5:Ce nanophosphors,' *Appl. Phys. Lett.*, 88 [10] 103108-1 (2006).

106. J. Wilkinson, 'Characterization and optimization of solution-derived chalcogenide glass thin films,' *MS Thesis, Clemson University* (2012).

107. S. Kedenburg, M. Vieweg, T. Gissibl and H. Giessen, 'Linear refractive index and absorption measurements of nonlinear optical liquids in the visible and near-infrared spectral region,' *Optical Materials Express*, 2 [11] 1588-1611 (2012).

APPENDIX A: EXAMPLE G-CODES TO CONTROL CNC MOVEMENT

Description: Serpentine path with y_{offset} = 0.5 mm, v_x = 20 mm/min, distance in x-direction of 30 mm, for a total distance in the y-direction of 5 mm.

```
G21 G90 G64 G40
G0 X0 Y0 Z0
G1 X-30 F20
G1 Y0.5
G1 X0
G1 Y1
G1 X-30
G1 Y1.5
G1 X0
G1 Y2
G1 X-30
G1 Y2.5
G1 X0
G1 Y3
G1 X-30
G1 Y3.5
G1 X0
G1 Y4
G1 X-30
G1 Y4.5
G1 X0
G1 Y5
M2
```